Ph.D. DISSERTATION

Seismic source analysis with multi-faceted approaches

다각적 접근법에 기반한 지진원 특성 분석

BY

Jeong-Ung Woo

FEBRUARY 2020

School of Earth and Environmental Sciences
College of Natural Sciences
Seoul National University

Seismic source analysis with multi-faceted approaches

다각적 접근법에 기반한 지진원 특성 분석

Junkee Rhie

A dissertation submitted in partial fulfillment of the requirements for the degree of Doctor of Philosophy

NOVEMBER 2019

Seoul National Unversity

School of Earth and Environmental Sciences

Jeong-Ung Woo

Confirming the Ph.D. Dissertation written by Jeong-Ung Woo

DECEMBER 2019

Chair	YoungHee Kim	(Seal)
Vice Chair	Junkee Rhie	(Seal)
Examiner	Kang-Kun Lee	(Seal)
Examiner	Tae-Seob Kang	(Seal)
Examiner	Seongryong Kim	(Seal)

Abstract

Intraplate earthquakes or IEs occur when tectonic stress is transmitted to critically stressed fault systems from plate boundary regions. Compared to the plate boundary, the observed seismicity in the intraplate region is relatively low and the locations of detected earthquakes are not confined in a specific region. Identifying fault structures beneath surfaces requires tremendous work of geophysical exploration, and it is more difficult to identify how stresses transmitted to remote areas over hundreds of kilometers interact with fault structures inside the plate. The Korean peninsula is a representative example of intraplate region, which is located 800 km away from the Ryukyu and Nankai trenches, and moderate earthquakes of which people can feel were rarely observed ever. Among the local earthquakes detected from the official seismic instrumental recordings by Korean Meteorological Administration, only ten earthquakes has local magnitudes (M_{L}) equal to or greater than 5 since 1978. Therefore, two recent 2016 M_{L} 5.8 Gyeongju earthquake and 2017 M_{L} 5.4 Pohang earthquakes provide unprecedented opportunities to observe seismic behaviors in Korean peninsula. The purpose of my study is to identify the various seismic source properties of the moderate earthquakes in the Korean Peninsula and to provide case studies what kinds of structure and stress state can cause earthquakes in intraplate region.

From the results of earthquake source parameter on the 2016 M_{L} 5.8 Gyeongju earthquake and its consecutive earthquake sequences, I observed that the mainshock occurred beneath the Yangsan fault with surface expressions, but considering that no clear surface deformations were found and the fault plane delineated by the spatial distribution of aftershocks has a strike deviated from the Yangsan fault, unrevealed fault structure developed beneath the Yangsan fault has been favorably reactivated to the current stress field. The reverse faults and strike-slip faults observed from focal mechanism analysis are matched with the principal stress applied to the Korean peninsula

that is mainly aligned to the east-west direction. The distribution of the aftershocks has confirmed that the Gyeongju earthquake did not occur on a single fault, but on at least three segmented fault zones. In particular, the static stress changes generated by the M_{L} 5.1 earthquake that occurred $\sim$ 50 minutes earlier than the main earthquake increased the Coulomb stress at the position of the following M_{L} 5.8 earthquake, which can be interpreted as an sequentially triggered earthquake. I observed the perturbations of stress field at the Gyeongju aftershock area. Especially, the phenomenon that the strike-slip fault is dominant in the area deeper than 15km can be interpreted to be related to the dense earthquake clusters moving along the strike directions at this depth.

Since the 2017 M_{L} 5.4 Pohang earthquake occurred near the Pohang geothermal power plant, the spatial and temporal distribution of the Pohang mainshock and the earthquakes during the five hydraulic stimulation periods at the injection site were closed examined with the period of fluid injection into binary geothermal wells. As a result, the Pohang earthquake and its immediate foreshocks occurred on the same fault plane for the earthquake during the hydraulic stimulations into a specific well and the earthquakes observed for the earthquakes in stimulation periods were migrated to the location of mainshock as well as its foreshocks. The observed fault plane corresponds to fault system identified from the aftershock distribution and also is matched with the observation that the crossing point with geothermal well coincides with the breakage inferred from an image logging device.

A detailed location analysis on the Pohang aftershocks suggest that at least four fault segments were reactivated and the largest aftershock of M_{L} 4.6 is considered to be ruptured on the conjugate fault to the mainshock rupture area. The fault plane involved in the Pohang mainshock was divided into three segments, and the hypocenter of the mainshock is situated on the intersection line between two interconnecting fault segments. I inverted the slip distribution of the mainshock rupture by assuming com-

plex fault geometry and the results indicate that two parts of slip patches were ruptured with temporal gap of 2s at SW and NE part respectively, during the whole slip history of 5 s. The time interval between two patches may indicate that the fault segment at NE part spatially disconnected from the other fault segments were triggered by dynamic stress changes generated by the first rupture at the SW part.

Characteristics of the moderate earthquakes in the Gyeongsang basin investigated by multi-faceted approaches for the two recent earthquakes can be summarized as the following five points: (1) the reactivation of complex fault system, not limited to a single fault, (2) the dominance of strike-slip and reverse faults, which can favorably occur in a response to the current stress field applied in Korea peninsula, (3) the possible causality between surface fault traces that can be regarded as to be generated with the basin formation process and the delineated fault plane from observed seismicity, (4) the increase of seismic $\boldsymbol{b}$-values during a certain period of aftershock sequences, (5) the earthquakes whose magnitudes are greater than 4 were located either at the edge of the fault or the interconnecting point between two fault segments. These characteristics can be applied to investigate the location of earthquakes found in ancient literatures and candidates of future earthquakes on the Korean Peninsula, and it can be applied for the understanding of the general characteristics of globally observed IEs.

keywords: earthquake location, focal mechanism analysis, finite fault inversion, induced and triggered seismicity, aftershock monitoring system

student number: 2015-20467

Contents

List of Tables

List of Figures

Chapter 1

Introduction

Intraplate earthquakes occur in tectonic plates with low strain rates, away from plate boundaries (Johnston, 1989). Although they host only 5% of the world's seismic moment release, some of these events are potentially responsible for a disproportionate amount of casualty (Gangopadhyay and Talwani, 2003; Talwani, 2014) in some of the more densely populated areas, such as 1886 Charleston earthquake (Durá-Gómez and Talwani, 2009), 1976 Tangshan earthquake (Chen, 1988), and 2001 Bhuj earthquake (Rastogi et al., 2001). In spite of the importance in terms of seismic hazard analysis, the physical properties of intraplate earthquakes are not well understood. It is widely accepted that intraplate earthquakes are caused by the tectonic forces transmitted from plate boundaries and located in preexisting zones of weakness such as failed rifts (Sykes, 1978; Talwani and Rajendran, 1991; Zoback, 1992; Bodin and Horton, 2004; Tavakoli et al., 2010). However, the clear causality between the preexisting weak zones and the location of the intraplate earthquakes has not been verified, in that there are a few reported cases where intraplate earthquakes occurred regardless of old geological surface faults (Ferreira et al., 1998; Assumpçao et al., 2004). Furthermore, it is difficult to identify the correlation because it is rare for a fault rupture to extend to the surface (Adams et al., 1991). Although our understanding of the characteristics of intraplate earthquakes has advanced slowly due to their rarity, the increasing number of installations of seismographs in intraplate regions and the diverse approaches appropriate for array networks have expanded our knowledge about these earthquakes (Talwani, 2014; Bianchi et al., 2018; Matos et al., 2018; Ross et al., 2018; Soto-Cordero et al., 2018).

The southern part of the Korean Peninsula lies within the eastern margin of the Eurasian Plate and the nearest tectonic boundary from the peninsula is $\sim$ 800 km to the southeast at the Ryukyu and Nankai Trough (So et al., 2016), and thus it is classified as a intraplate region where the frequency of earthquakes is relatively low compared to that on plate boundaries. Based on an earthquake catalogue by the Korea Meteorological Administration (KMA), only 10 earthquakes with $M_{\mathrm{L}} \geq 5$ were in-

strumentally recorded in and around the Korean peninsula since 1978. Among them, five earthquakes occurred for the last five years. The number of seismic observatory operated by KMA has increased in recent years and temporary seismic networks were installed for monitoring aftershocks of the two largest earthquakes, the 2016 Gyeongju earthquake and the 2017 Pohang earthquake (Kim et al., 2016a,b; Hong et al., 2017; Kim et al., 2018b; Woo et al., 2019a,b). Such a plenty of seismic observations at regional and local distances can provide a valuable opportunities to analyze multi-scaled source properties of the moderate earthquakes.

The largest amongst them, a M_{L} 5.8 earthquake in Gyeongju, on 12 September 2016, produced strong coseismic ground shaking, which was sufficient to be felt throughout South Korea (Hong et al., 2017). Including the M_{L} 5.1 event, followed 50 minutes later by the occurrence of the M_{L} 5.8 event, and the largest aftershock with M_{L} 4.5 recorded after a week, hundreds of events were reported near the epicenter of the M_{L} 5.8 earthquake (Kim et al., 2016b). The epicenters of the three events are located in the Gyeongsang Basin where several systematic fault sets, such as the Yangsan Fault System and the Gaum Fault System, are developed (Chang, 1977; Hwang et al., 2008) and microseismic activities occur along the surface geological lineaments or faults (Huang et al., 2017). A deep seated fault system identified from the hypocentral distributions of 2016 Gyeongju aftershocks has been suggested to result in the sequences (Hong et al., 2017; Kim et al., 2017b; Lee et al., 2018; Son et al., 2018). More specifically, recovered fault plane for the main shock is striking to the NNE-SSW direction and steeply dipping to the SE direction with a right-lateral strike-slip motion based on the regional moment tensor inversion and the hypocentral distribution (Hong et al., 2017; Kim et al., 2018b; Son et al., 2018). Since the Yangsan Fault is located close to the epicenters and the total amount of dextral displacement on the fault is nearly 30 km (Kyung, 2003), the possible correlation between the Yangsan Fault System and the Gyeongju earthquake sequences have been addressed (Kim et al., 2017c, 2018b; Uchide and Song, 2018). However, it is difficult to prove the direct causal-

ity between the deep seated fault plane and the surface faults because the focal depth exceeds 10 km and no surface deformation due to E2 has been reported (Park et al., 2018).

Next year, the second largest event of M_{L} 5.5 among instrumentally recorded events in and around Southern Korean peninsula occurred in Pohang on 15 November 2017 (Kim et al., 2018c; Grigoli et al., 2018). The event has been suspected as to have an anthropogenic origin related to the fluid stimulation due to its proximity to the Enhanced geothermal system (EGS). The surface deformation observed from D-InSAR analyses represents large amount of slip patches at northeast parts of the mainshock hypocenter. The aftershock distribution suggests that the mainshock occurred on a fault plane striking striking to a NNE direction with NW dip angle, which can be considered as a reactivation process of the complex fault system developed throughout the Pohang basin such as NE striking Heunghae fault and Gokgang fault. The inverted moment tensor solutions for the three largest earthquakes have a very high percentage of non-double-couple components (Grigoli et al., 2018), which can result from intervention of multi-fault system in their rupture processes. In this study, I investigated the detailed source parameters related to the 2016 M_{L} 5.8 Gyeongju earthquake sequences, the 2017 M_{L} 5.5 Pohang earthquake sequences using seismograms obtained from not only permanent stations but also temporary seismic recording stations when it is available. The basic goals of the study is (1) to create more complete catalogs for earthquake sequences, (2) to provide comprehensive source properties: spatio-temporal distribution, faulting mechanisms, regional stresses, and stress drop in each sequences, and (3) to understand interactions among regional faults, occurrence of earthquakes, and possible fluid migrations. In chapter 2, and 3, I provided case study for the 2016 M_{L} 5.8 Gyeongju earthquake sequences. In chapter 4, 5, and 6, I analyzed detailed source parameters related to the 2017 M_{L} 5.5 Pohang earthquake sequences including the period of hydraulic stimulations. For two inland earthquakes, a team for monitoring aftershock sequences has installed and operated temporary seis-

mic networks until now. The multifaceted approaches of the source parameter analysis described above will contribute to a better understanding of the reactivation process of interacting complex faults in the Gyeongsang Basin, induced and triggered seismicity related to the hydraulic injection at the Pohang EGS site, and the generalized characteristics of intraplate earthquakes that occur in complex fault systems.

Chapter 2

The 2016 Gyeongju earthquake sequence revisited: aftershock interactions within a complex fault system

2.1 Introduction

Intraplate earthquakes pose certain seismic hazards and risks as natural disasters, although they are responsible for only 5% of the world's seismic moment release (Chen, 1988; Johnston, 1989; Rastogi et al., 2001; Wang, 2007; Durá-Gómez and Talwani, 2009). Despite their importance in hazard analysis, their general characteristics are not well understood (Gangopadhyay and Talwani, 2003; Talwani, 2014). It is widely accepted that intraplate earthquakes are caused by the tectonic forces transmitted from plate boundaries and are located in pre-existing zones of weakness, such as failed rifts (Sykes, 1978; Talwani and Rajendran, 1991; Zoback, 1992; Bodin and Horton, 2004; Tavakoli et al., 2010). However, this hypothesis has not been clearly verified because some studies have reported that intraplate earthquakes occur regardless of faults with surface expressions (Ferreira et al., 1998; Assumpçao et al., 2004). Furthermore, the rarity of the surface extension of fault ruptures makes it hard to observe the causality (Adams et al., 1991). Our understanding of intraplate earthquakes has advanced as many seismographs are installed in intraplate regions and diverse approaches for array networks are developed (Talwani, 2014; Bianchi et al., 2018; Matos et al., 2018; Ross et al., 2018; Soto-Cordero et al., 2018).

The Korean peninsula is an intraplate region located $\sim$ 800 km away from the Ryukyu and Nankai trough. According to an event catalogue published by the Korea Meteorological Administration (KMA), only 10 earthquakes with $M_{\mathrm{L}} \geq 5$ have been instrumentally recorded since 1978 (So et al., 2016). The largest among them, a M_{L} 5.8 earthquake in Gyeongju, South Korea on 12 September 2016, produced strong coseismic ground shaking, which was sufficient to be felt throughout South Korea (Hong et al., 2017). The event happened in the Gyeongsang Basin, where there are several systematic fault sets with surface expression, such as the Yangsan and Gaum Fault Systems (Figs. 2.1 and 2.2a) (Chang, 1977; Han et al., 2017; Hwang et al., 2008). The 2016 Gyeongju earthquake sequence started from a M_{L} 5.1 event that ruptured 50 minutes before the M_{L} 5.8 event, and thousands of earthquakes, including a M_{L}

4.5 aftershock on September 19, occurred in the sequence (Kim et al., 2016b). Hereafter, for convenience, we refer to the three events of M_{L} 5.1, M_{L} 5.8, and M_{L} 4.5 as E1, E2 (the main shock), and E3, respectively. From the distribution of the hypocenters and inverted moment tensors of the three events, it has been demonstrated that these earthquakes occurred on a deep-seated fault system at a depth range of 10–18 km (Kim et al., 2016a; Hong et al., 2017; Kim et al., 2017b, 2018b; Lee et al., 2018; Son et al., 2018). In particular, Son et al. (2018) delineated two distinct parallel dextral faults striking to the NNE–SSW direction from relocated aftershocks, and Uchide and Song (2018) observed that the inverted finite fault slips of E1 and E2 propagated towards SSW and NNE directions, respectively. A possible correlation between the Yangsan Fault and the Gyeongju earthquakes has been raised because the epicenters are located close to the fault, with 30 km of dextral displacement (Kyung, 2003; Kim et al., 2017b,c; Lee et al., 2018). However, it is difficult to prove whether the deep-seated fault system extends to the surface because the focal depths exceed 10 km, and no surface deformation due to E2 has been reported (Park et al., 2018).

In this study, we investigated the source parameters of the Gyeongju earthquakes using a larger data set obtained from both permanent and temporary seismic networks. Our basic goal is to create a more complete catalogue of earthquakes in the vicinity of the mainshock from 2014 to 2016. We located earthquakes detected by an automatic algorithm and resolved the detailed fault segments based on the Double-Difference method. The relative magnitudes of events were estimated from the amplitude ratios with reference events. Long period waveforms and the first motions of P-wave polarities were used for moment tensor inversion and focal mechanism determination, respectively. Based on our catalogue, we conducted further analysis, including the consideration of statistical parameters, tectonic stress fields, and the role of stress transfer induced by E1 and E2. These multifaceted approaches will contribute to a better understanding of both the reactivation process of interacting complex faults in the aftershock region and the generalised characteristics of intraplate earthquakes within

complex fault systems.

2.2 Data acquisition

The data used for the detection of events and the determination of their hypocenters, magnitudes, and focal mechanisms are divided into two parts: the continuous waveforms recorded at permanent seismic stations and those from temporary seismic stations installed for monitoring aftershocks and analysing detailed source parameters (Fig. 2.1). Three years of waveform data from January 2014 to December 2016 were gathered from six broadband and two short-period seismometers within 50 km of the E2 epicenter. For moment tensor determination of the ten selected events, waveforms recorded at three broadband stations with epicentral distances greater than 50 km were also collected, and data from five broadband stations (inset of Fig. 2.1) were used in the end. The temporary network of 27 broadband instruments began operation within two hours of E1, and we assembled the waveform data through the end of 2016 (Fig. 2.1). For the epicenter of E2, the data coverage of the eight permanent stations yields an azimuthal gap of 80° and a minimum epicentral distance of 5 km. However, by adding data from the temporary instruments, the two parameters could be reduced to a gap of 32° and a minimum epicentral distance of 0.9 km. Therefore, it is expected that not only can additional events with small magnitudes be detected but also that the source parameters of the earthquakes can be analysed at high-resolution scales using both the permanent and temporary stations (see details about the temporary seismic network in Kim et al. (2016a)).

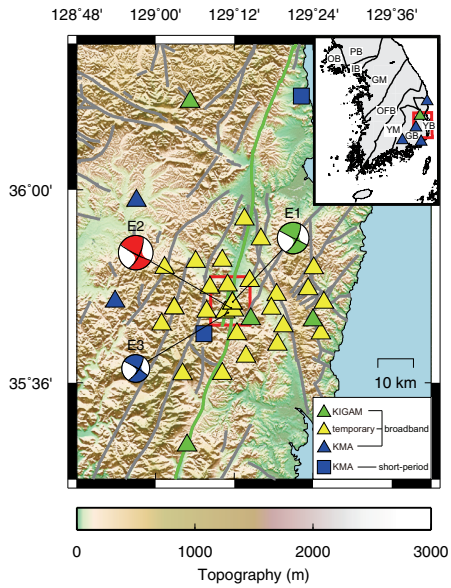

Figure 2.1: The distribution of the stations used for the detection of events and determination of their locations, magnitudes, and focal mechanisms. The three major events (E1, E2, and E3) are shown with their moment tensors obtained from the low-frequency waveform inversion method. The two faults with surface expressions near the main shock are denoted as green lines. Other faults and lineaments with surface expression are shown as dark grey lines. Six broadband sensors operated by the Korean Meteorological Administration (KMA) and Korea Institute of Geoscience and Mineral Resources (KIGAM) are illustrated as green and blue triangles, and the 27 temporary broadband sensors are represented by yellow triangles. Two short-period sensors from the KMA are denoted as blue squares. The red box corresponds to the regions in Fig. 2.2b and Fig. 2.3a. Major geological units are separated with black lines in the inset: PB (Pyungnam Basin), OB (Ongjin Basin), IB (Imjingang Belt), GM (Gyeonggi Massif), OFB (Okcheon Fold Belt), YM (Youngnam Massif), GB (Gyeongsang Basin), and YB (Yeonil Basin). The box with red lines in the inset indicates the region of the main figure. The five broadband seismometers shown in the inset are used to determine the moment tensor solutions of the ten selected events.

2.3 Hypocenter determination

2.3.1 Method of analysis

To analyse not only the aftershocks within a few kilometres of the E2 epicenter but also the seismicity changes before and after E1, we applied an automatic earthquake detection method to continuous waveform data and determined their absolute locations using the single difference method (HYPOELLIPSE, Lahr (1999)). In order to resolve the spatial pattern of the aftershocks, the earthquakes near E2 were relocated using the Double-Difference algorithm (HypoDD, Waldhauser and Ellsworth (2000)). P- and S-wave phase arrival times were automatically measured from the recursive short-term average to long-term average ratio (STA/LTA) method (Withers et al., 1998; Grigoli et al., 2014; Woo et al., 2017). Then, incorrectly measured phase arrival times were manually inspected to discriminate overlapping events and remove false detections. A regional one-dimensional velocity model for the Gyeongsang Basin (e.g. Kim et al. (2011)) was applied throughout the hypocenter determination.

In the process of relocation, the travel time differences calculated from 545,024 chosen arrival time pairs as well as those measured from 3,840,597 waveform cross-correlation pairs were applied. We tested whether the data obtained from the chosen arrival times distort the relocation results and confirmed insignificant changes in the results. For the waveform cross-correlation between the two events, time windows centerd at the measured arrival times were interpolated at a sampling rate of 1,000 Hz, and the maximum cross-correlation coefficient (maxCC) of 3-s time windows were measured by allowing up to ±1.5 s time shifts (e.g. Hauksson and Shearer (2005)). All the seismograms were bandpass-filtered from 1 to 10 Hz before the cross-correlation, and the travel time differences between the two waveforms were used only if the maxCC was above 0.85. To allow the bootstrapping to test the relocation uncertainties, the events were relocated by resampling the differential travel times for each event pair. The mean of the standard deviations of the 20 trials corresponds to 37 m horizontally

and 54 m vertically, respectively.

2.3.2 Absolute location

During the study period, 2,931 earthquake candidates were automatically detected, and 2,848 earthquakes within 80 km of the epicenter of E2 were selected through the manual inspection of waveforms (Fig. 2.2). Only 148 events (5.2%) occurred before the onset of E1. These events were mainly observed in offshore regions or along several local fault structures (Fig. 2.2a). However, only two events were located within 10 km of the epicenter of E2 during this period, and the background seismicity near the aftershock region is therefore considered insignificant. After the onset of E1, the number of earthquakes located outside the 10 km radius from the E2 epicenter was 146 (5.1%), and their locations were similar to those that occurred before E1. However, some regions experienced spatial changes in seismic activities following the occurrence of E1. For example, the earthquakes at the location where the Ulsan and Dongrae Faults intersect shifted 5 km to the south (see the blue circled area in Fig. 2.2a). The earthquakes near the Miryang Fault migrated to the north by a few kilometres (see the magenta circled area in Fig. 2.2a). These observations suggest that the seismicity changed due to the Gyeongju earthquakes, although it is hard to verify for how long these changes are maintained.

Starting from E1, 2,552 events (89.6%) occurred within 10 km from the epicenter of E2, and the distribution of the hypocenters showed a trend along the NNE–SSW direction (Fig. 2.2b). Although their epicenters are mainly located between the two surface fault traces of the Yangsan and Deokcheon Faults striking to the NNE–SSW or N–S direction (Kim et al., 2017c), the spatial distribution of the earthquakes does not exactly coincide with the surface geological features (Fig. 2.2b).

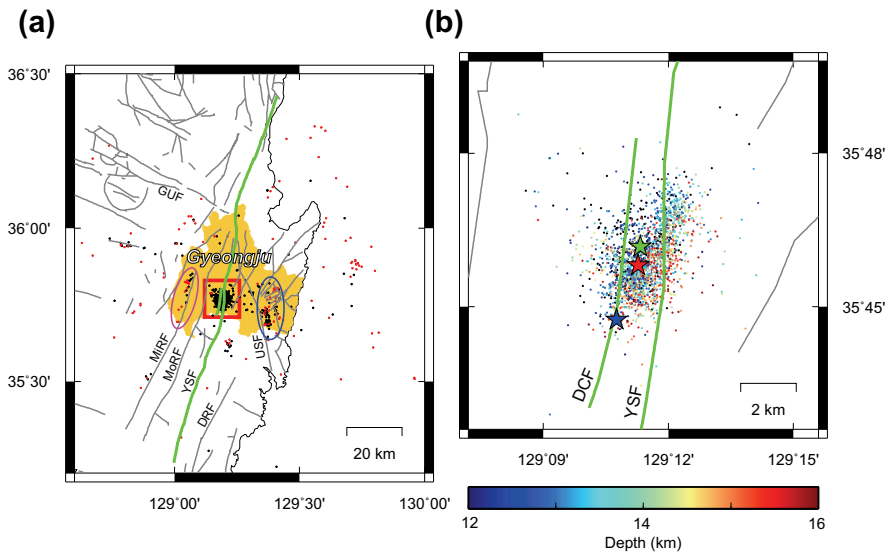

Figure 2.2: (a) Distribution of the hypocenters calculated from the visually inspected P-phase and S-phase arrival times and (b) a zoomed-in view of the region of interest. The seismicity values before and after the onset of E1 are shown with red and black dots, respectively. The names of major surface ruptures are presented with abbreviations: GUF (Gaum Fault), MiRF (Miryang Fault), MoRF (Moryang Fault), YSF (Yangsan Fault), DRF (Dongrae Fault), USF (Ulsan Fault), and DCF (Deokcheon Fault). The blue circled area and magenta circled area have experienced temporal changes in seismicity (see details in Section 2.3.2). The red box in (a) corresponds to the zoomed-in region of (b). The green, red, and blue stars in (b) are the locations of E1, E2, and E3, respectively. The other symbols match those in Fig. 2.1.

2.3.3 Double-Difference relocation

Including the three largest events, 2,493 events were relocated within 10 km from the epicenter of E2 (Fig. 2.3a). This number is $\sim$ 5 times greater than that of the relocated events of previous studies, which only used data from permanent station networks for a similar period (Son et al., 2018). This result illustrates the importance of aftershock monitoring networks for observations of micro-seismic events (Kim et al., 2016a, 2018b). In the map view, aftershocks are primarily aligned along N26°E, extending 5 km in the fault-parallel direction and 2 km in the fault-normal direction. The focal depths of the earthquakes range from 12 km to 16 km (Figs. 2.3c and 2.3d). Comparing the spatial pattern of the relocated hypocenters with that obtained from the single difference method, we can clearly observe the distinctive fault geometries that cannot be resolved in the initial distribution. In particular, it seems that the largest events (E1 and E2) occur independently on two distinct sub-parallel faults with an offset of 600–700 m, while E3 occurred on a conjugate fault plane with an ESE–WNW strike (Fig. 2.3a). For convenience, hereafter, we refer to the three fault planes overlapping with the locations of E1, E2, and E3 as F1, F2, and F3, respectively. The sizes and shapes of each fault plane are estimated from the hypocenter distributions.

The F1 plane strikes at N26°E and deepens towards the southeast direction with a dip angle of 65° in the depth range of 13.0–16.0 km; it is 3.0 km long and 3.1 km wide, comprising a square-like fault plane (Fig. 2.3c). Located to the east of F1, F2 has the same strike as F1, but the dip angle of the fault plane varies with the depth range and can be separated as: (1) F2a with a dip of 55° and a depth range of 11.5–13.5 km and (2) F2b with a dip of 69° and a depth range of 12.5–16.0 km (Figs. 2.3c-d). E2 is located on F2b, whose dip angle is matched with that of one nodal plane of the E2 calculated moment tensor solution. The widths of F2a and F2b correspond to 2.4 km and 3.7 km, respectively, while the lengths of F2a and F2b are the same at 5.5 km. The strike of F3 is set to N116°E, since the earthquakes near E3 are aligned perpendicularly to the strikes of F1 and F2. However, the number of earthquakes distributed over the

streak is not enough to infer the dip angle. Therefore, we modelled F3 as a vertical fault plane based on the moment tensor inversion of E3 (Fig. 2.3a). Using the spatial distribution of the aftershocks for an hour from the onset of E3, the length and width of F3 were set to 1.0 km and 0.7 km, respectively. The parameters of each fault plane are summarised in Table 2.1, and the schematic diagram is illustrated in Fig. 2.4.

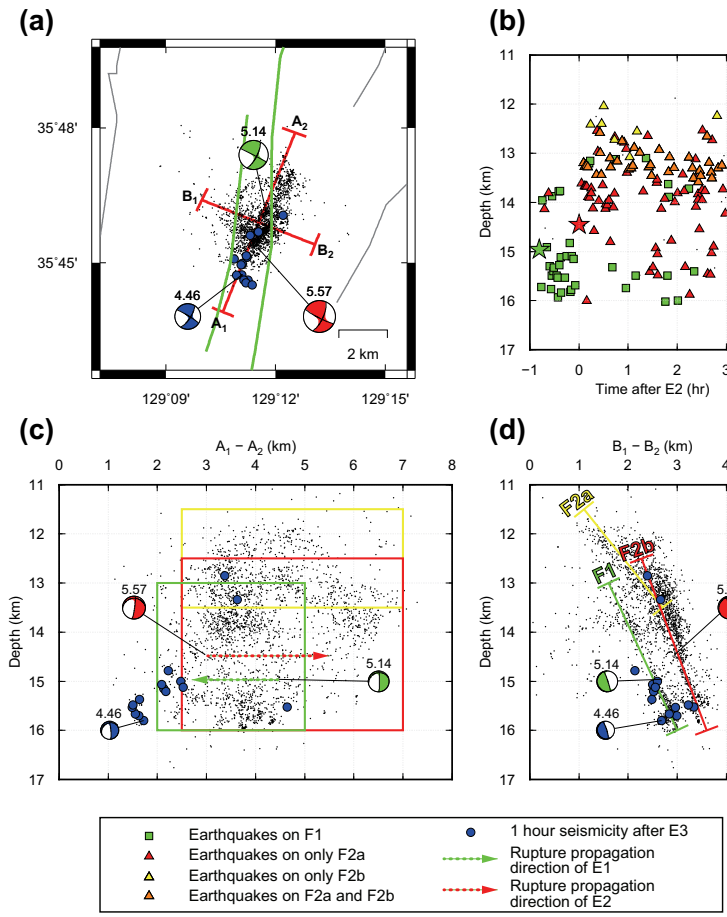

Figure 2.3: Distribution of the 2,510 relocated hypocenters in the aftershock region. (a) Distribution of the epicenters of the Gyeongju earthquakes. (b) Five-hour seismicity at the early stage of aftershocks as a function of focal depth. Four different symbols are used for the events in four selected periods. (c-d) The depth distributions along A1–A2 (oriented N26ºE) and B1–B2 (oriented N116ºE). The three moment tensor solutions of E1, E2, and E3 are distinguished as three different colours of compressional quadrants: green (E1), red (E2), and blue (E3). The blue dots in (a), (c), and (d) represent one hour of seismic activities following E3, and the estimated rupture propagation directions of E1 and E2 by Uchide and Song (2018) are denoted as green and red arrows, respectively. Fault geometries of F1, F2a, and F2b are illustrated as green, yellow, and red lines, respectively. The other symbols match those in Fig. 2.1.

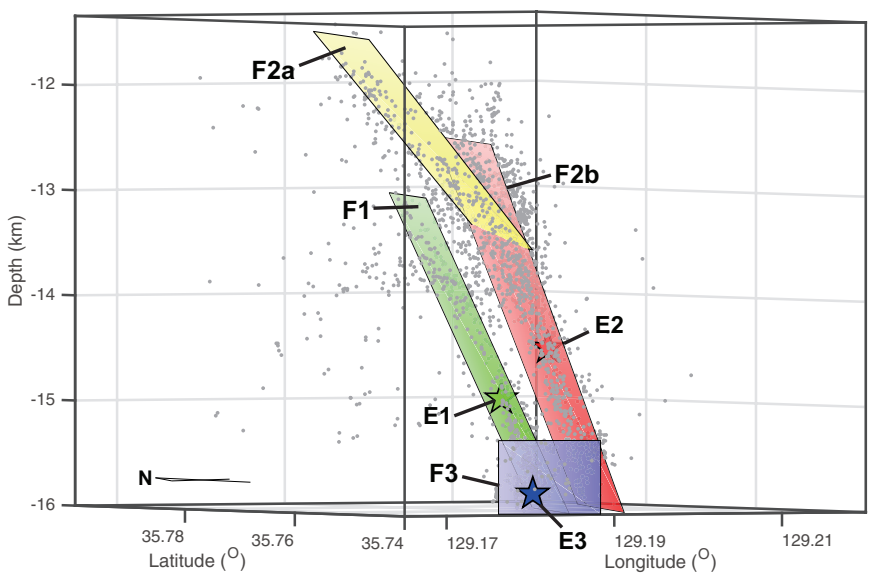

Figure 2.4: A three-dimensional schematic diagram to illustrate the spatial distribution of the aftershocks and the geometry of the four faults (F1, F2a, F2b, and F3). Detailed information for each fault is summarised in Table 2.1.

E1 and E2 are located at the north-eastern part of F1 and south-western part of F2 compared with the spatial distribution of the aftershocks (Figs. 2.3c–d). The asymmetric aftershock distributions with respect to hypocenters may suggest that E1 and E2 ruptured towards the southwest and northeast, respectively (Mendoza and Hartzell, 1988). This is consistent with the rupture directivity inferred from the finite fault slip models of E1 and E2 (Uchide and Song, 2018).

2.4 Aftershock statistics

2.4.1 Magnitude estimation

Choosing from among the various methods to estimate earthquake magnitude, we used the scaling relationship between magnitude differences and amplitude ratios. If two events have similar ray paths, focal mechanisms, and source time histories, the magnitude difference (dM) between them can be expressed as:

$$dM = clog_{10}\alpha \tag{2.1}$$

where α is the amplitude ratio of one event to the other event, and c is a linear scaling parameter between the amplitude ratio and the magnitude difference (Shelly et al., 2016). In this study, the linear relationship and scaling parameter (c) of Eq. (1) were investigated using aftershocks in the KMA catalogue, and the magnitudes of the aftershocks detected were relatively determined from linear scaling with the KMA catalogue events.

For the cross-correlation measurements applied in the relocation procedure, the amplitude ratios between two waveforms aligned by their phase arrival times were measured as the slope of the principal component obtained from the principal component analysis (PCA) for the data vectors (e.g. the amplitude relation between two aligned waveforms on a specific channel; see details in Fig. 2.2 of Shelly et al. (2016)). The PCA sequentially finds principal components, which show the relationships among

variables (Jolliffe, 2011). Compared to measuring peak amplitude ratios, this method is known to give reliable amplitude ratios because it applies full waveforms, unlike other methods that use only the differences in peak amplitude values (Shelly et al., 2016). Figure 2.5 illustrates that the logarithms of the amplitude ratios are approximately linearly proportional to the magnitude differences for the 165 events in the KMA catalogue that are also listed in our event catalogue. The c values estimated from the least squares method and PCA are not significantly different (0.62 and 0.69, respectively). Of the two methods, the c value is taken from the PCA, since it is a more appropriate approach for extracting patterns among variables without assigning dependent and independent variables (Jolliffe, 2011).

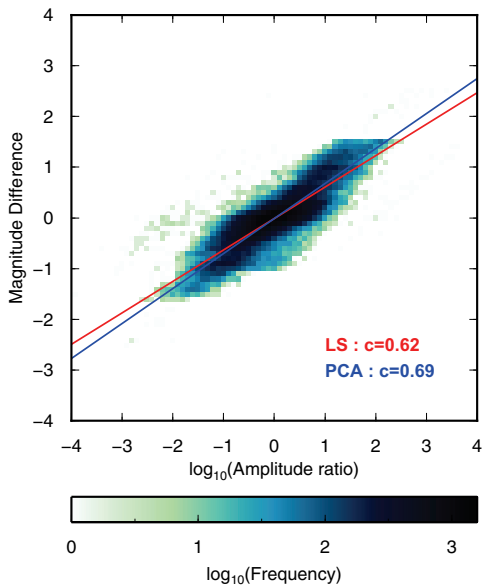

Figure 2.5: Determination of the scaling parameter c in Eq. (1) by using KMA catalogue events. For an event pair, the logarithm of the amplitude ratio measured from waveform data and the magnitude differences between the two events correspond to the abscissa and ordinate of the graph. Two methods were tested for the estimation of the c value: the least squares method (red line; $c = 0.62$) and the principal component analysis method (blue line; $c = 0.69$).

For the whole set of aftershocks, we calculated the amplitude ratios between the target events and KMA catalogue events in the same manner for the estimation of the c value. Each measured amplitude ratio for a target event is translated to a relative magnitude by using Eq. (1) and a c value of 0.69. To increase the reliability of the results, the magnitudes of the target events were estimated by averaging the magnitudes obtained from more than 10 measured amplitude ratios. Here, we define the estimated magnitudes as $\boldsymbol{M_{rel}}$ since Eq. (1) can be valid for a limited range of magnitudes. From the procedure, the magnitudes of 2,560 earthquakes were relatively estimated.

2.4.2 Spatial and temporal characteristics of aftershock activity

As characteristics for aftershock occurrences, the frequency–size distribution and the aftershock decay rate have been applied in many cases (Wiemer and Katsumata, 1999; Aktar et al., 2004; Zhao and Wu, 2008; Enescu et al., 2011; De Gori et al., 2014; Abdelfattah et al., 2017; Ansari, 2017). The former characteristic can be expressed in the following way:

$$log_{10}N = \boldsymbol{a} - \boldsymbol{bM} \tag{2.2}$$

where N is the cumulative number of earthquakes with magnitudes equal to or greater than $\boldsymbol{M}$. The $\boldsymbol{a}$–value and $\boldsymbol{b}$–value, which are generally treated as constants, reflect the characteristics of earthquakes in a particular region and period. However, they can change with time or location. In particular, the $\boldsymbol{b}$–value can be affected by various physical properties such as asperities, effective stress, material heterogeneity, crack density, thermal gradient, and tectonic regimes (Wiemer and Katsumata, 1999; Westerhaus et al., 2002; Schorlemmer et al., 2005; Goebel et al., 2017; Raub et al., 2017; Tormann et al., 2014). The frequency of aftershocks generally decreases in inverse proportion to time, and the tendency can be expressed using Omori's formula:

$$R(t) = \boldsymbol{K}(t + \boldsymbol{c})^{-\boldsymbol{p}} \tag{2.3}$$

where K, c, and p are constants to be determined. In particular, the p–value that represents a measure of the decay rate of the seismic activities is known to vary from 0.6 to 1.8 (Wiemer and Katsumata, 1999), and many factors influence the variation in p-value, including structural heterogeneity, stress, and temperature in the crust (Utsu et al., 1995). In this study, we reasoned that the minimum magnitude of completeness (M_C) that satisfies Eq. (2) changes over time due to the expansion of the temporary observation network, affecting the estimation of b–values and p–values. Therefore, we first analysed the temporal variations in b for every set of 500 events in chronological order by allowing duplication of 400 events, considering the time-variant M_C (Figs. 2.6a–b). We then estimated b–values and p–values for all aftershocks and for two event subsets on F1 and F2 for the maximum value of M_C (Figs. 2.6c–d). The b–value for each event set is evaluated from the maximum likelihood method by Aki (1965) with a magnitude bin size (ΔM) of 0.1, and the uncertainty of each estimated b–value is calculated by using the Shi and Bolt (1982) equation. The M_C is calculated from a modified goodness-of-fit method from Wiemer and Wyss (2000). After the calculation of the goodness-of-fit value for every M_C with a 0.1 interval, we find the minimum M_C (M_{Cmin}) for which the goodness-of-fit value is greater than 0.9 and take the M_C that yields the maximum goodness-of-fit value in the range of [M_{Cmin}, $M_{Cmin} + 2\Delta M$]. The three constants and their standard deviations in Eq. (3) for each event set with magnitudes greater than M_C are estimated from the maximum likelihood procedure of Ogata (1983).

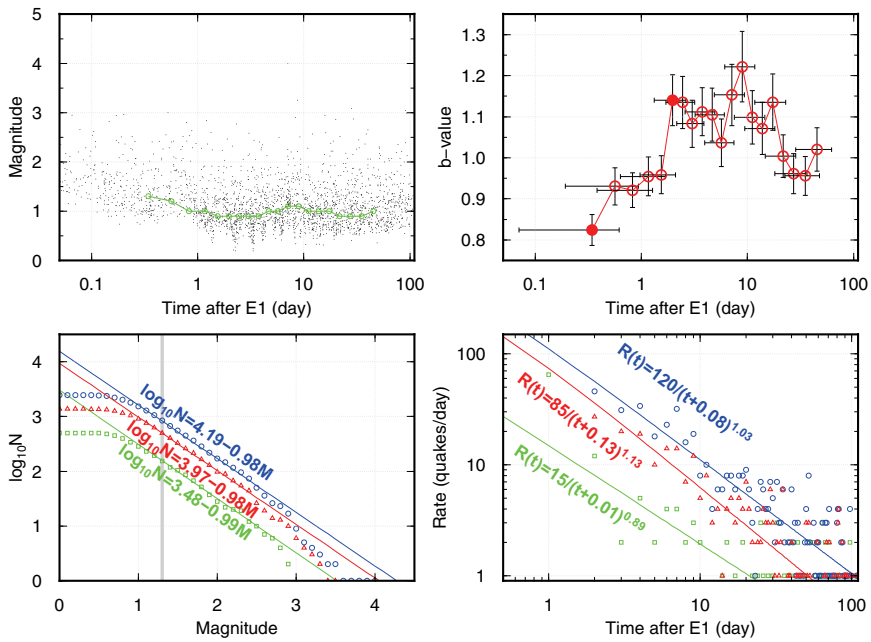

Figure 2.6: (a) Event magnitudes as a function of time. The temporal variation in M_C is represented as a green line. (b) The ***b***-value variation is a function of time. The horizontal and vertical error bars indicate one standard deviation of event origin times and ***b***-values, respectively. The ***b***-value difference between two event sets denoted as solid red dots was tested by Utsu's test (see Section 2.4.2). (c) The frequency–magnitude distribution of the three event clusters: all events (blue dots), F1 (green dots), and F2 (red dots). A grey line represents the M_C used for estimation of ***b***-values. (d) The occurrence rate of the three event clusters: all events (blue dots), F1 (green dots), and F2 (red dots). The three lines with different colours in (c) and (d) represent the obtained G-R law and modified Omori's Law, respectively.

The results of the time-variant M_C and b–values are presented in Figs. 2.6a–b. For the first three days, M_C decreases from 1.3 to 1 and remains at $\sim$ 1 for the subsequent period (Fig. 2.6a). The b–value, on the other hand, is 0.82 ± 0.04 at the initial stage and increases to 1.14 ± 0.06 during the three days after the onset of E1 (Fig. 2.6b). The b–values of the total data set and the events on F1 and F2 are approximately the same at 0.98 ± 0.03, 0.99 ± 0.07, and 0.98 ± 0.04, respectively, but the p–values of the three event sets are 1.03 ± 0.08, 0.89 ± 0.03, and 1.13 ± 0.08, respectively, which are slightly different from one another (Figs. 2.6c–d). For each event set, the M_C for calculating the b–values and p–values is fixed to 1.3, which is the maximum value over time. The initial three days of decreasing M_C correspond exactly to the period in which the temporary observation network was being expanded. The decrease in M_C during the early earthquake sequences may come from the high level of background noise. However, we ensured that the temporal change in M_C does not appear in the results from the 959 earthquakes detected by using only the eight permanent stations. The b–value temporarily increased from 0.82 to 1.14 during the initial three-day period in which the seismic observation network was being expanded. We tested and confirmed that the increasing trend still appears even if M_C is fixed to the highest value (i.e. 1.3) and confirmed that the choice between various M_C and fixed M_C does not affect the increase in b–value. The two event segments marked as solid red dots are offset by three days, and their b–value difference is estimated as 0.32 (Fig. 2.6b). To determine whether or not the difference between the two b–values is statistically significant, we applied Utsu (1992) test, and the probability that there would be no difference in the b–value between the two sets of populations is estimated as 9×10^{-5}, confirming that the difference in the b–values of the two sets of data would be statistically significant. The tendency for b–values to increase after the onset of an earthquake has been observed in other cases: the 2004 M_S 6.0 Parkfield earthquake (Shcherbakov et al., 2006) and the 13 September 1999 M_W 5.8 event between the Izmit epicenter and Lake Sapanca (Raub et al., 2017). Raub et al. (2017) estimated that the increase

in b–values is related not only to the release of stress but also to the unclamping of faults. Hosono and Yoshida (2002) reported that the expected number of relatively large earthquakes is lacking in later earthquake sequences compared with that calculated from the modified Omori formula for an early time period, and this effect may result in the relatively small b–values at the initial stages. The estimated b–values for all data sets, E1, and E2 are all close to 1 and consistent with the estimation of 1.04 for the KMA catalogue events (Hong et al., 2017). This b–value of 1 also corresponds to the commonly observed value in other earthquake sequences (Wu et al., 2015; Ansari, 2017). The p–value of 1.03 for the entire data set is considerably lower than the 1.53 value of Hong et al. (2017), who also used the KMA catalogue events. The disparity can be attributed to the use of different fitting ranges in Omori's Law or the additional consideration of M_C for determination of the p-values.

2.5 Moment tensor solutions and focal mechanisms

2.5.1 Method of analysis

In this study, the deviatoric moment tensor solutions were determined using the ISOLA software of Sokos and Zahradnik (2008) for 10 selected earthquakes with $M_L \geq 3$. After several trials were attempted for the appropriate stations and filtering ranges, the moment tensor solutions of the 10 selected earthquakes were determined using the waveforms recorded at four or five stations, and two different frequency ranges of 0.05–0.1 Hz were used for the three largest events, while 0.08–0.16 Hz were used for the rest. The optimal focal depths were determined from moment tensor inversion by testing different depth ranges with a 1-km bin. The same regional one-dimensional velocity model used in the location procedure (e.g. Kim et al. (2011) was used to construct Green's functions as well. For 519 aftershocks with more than 20 P-wave arrival times, the P-wave polarities at each station were manually measured, and we applied the FOCMEC software of Snoke (2003) to calculate their focal mech-

anisms. The focal mechanism analysis was performed only if an earthquake had at least 10 polarity measurements. We sorted out the candidate focal mechanisms with minimum measurement errors for each event and excluded events from the analysis if candidate solutions contained polarity errors larger than three. Among the possible solutions for each event, we selected one optimal solution, of which the sum of the distances from its P, T, and B axes to all other solutions on the focal sphere is minimised. All solutions, including the selected optimal solution, are visually inspected to confirm similarity in the mechanisms. We obtained 263 reliable focal mechanisms in this procedure.

2.5.2 Results

The detailed moment tensor inversion results of the 10 selected events are given in Fig. 2.7 and Table 2.2. Although some earthquakes have a considerable amount of compensated linear vector dipole components ($\sim$ 20%), double-couple components are generally dominant. All inverted moment tensor solutions are classified as strike-slip events, of which one nodal plane is parallel to F1 and F2, which is consistent with previous research studies (Kim et al., 2018b; Son et al., 2018). Assuming that the fault rupture of each earthquake propagates on F1 or F2, the true fault plane has an NNE–SSW strike direction with right-lateral movement.

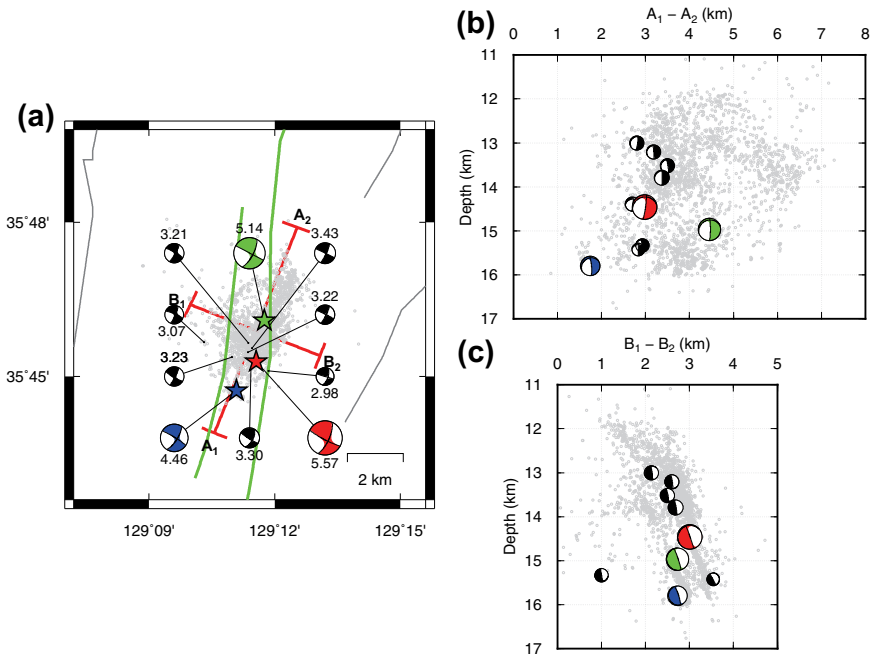

Figure 2.7: The spatial distribution of the 10 selected events with their deviatoric moment tensors. Each number above the moment tensor in (a) represents the moment magnitude of the event. The compressive quadrants of the three largest events in (b) and (c) are coloured in green (E1), red (E2), and blue (E3). All the relocated hypocenters are denoted as grey dots on the map in (a) and cross-sections in (b) and (c). The other symbols match those in Fig. 2.1.

We classified the 263 focal mechanisms estimated by the P-wave first motions according to the ternary diagram of Frohlich (1992). The number of earthquakes that correspond to strike-slip events and thrust events were 174 (66%) and 54 (21%), respectively. The remaining events were classified as odd faulting types, while no normal faulting events were observed. From the spatial distribution of the strike-slip events and thrust events, which account for 87% of the calculated focal mechanisms, we can observe that both types of focal mechanisms occur on both F1 and F2 (Fig. 2.8). The trend and plunge of the P-axis of the strike-slip events are 75° ± 11° and 10° ± 7°, respectively, and those of the thrust events are 77° ± 20° and 14° ± 10°, respectively, indicating that the trend of the maximum principal stress axis is homogeneous at 70–80°. However, despite the coexistence of the two faulting types on both F1 and F2, the detailed spatial distributions of the strike-slip and thrust events are quite different from each other, implying that the other principal stresses are locally heterogeneous. Reliability of the determined faulting types is verified by visually comparing the observed and expected P-wave amplitudes. For example, P-wave amplitudes recorded near the epicenters of strike-slip events should be weak, but they should be positive and large for thrust events. In order to cross-check the reliability of the inverted fault parameters calculated by the methods implemented in the FOCMEC and ISOLA software, the focal mechanisms of the four earthquakes inverted from both methods were compared, and no significant differences were observed.

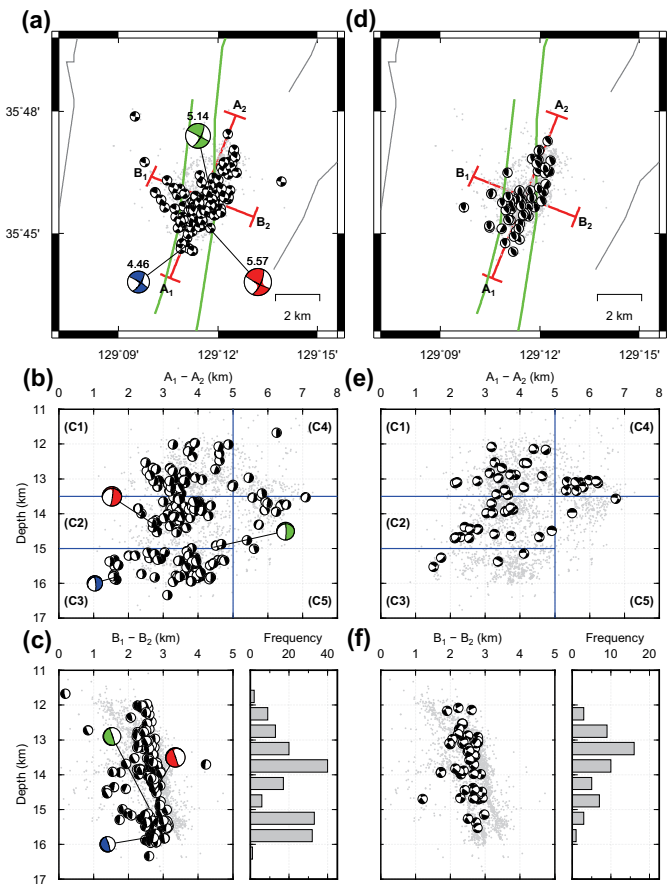

Figure 2.8: The hypocenter distribution of the 174 strike-slip events (a-c) and 54 thrust events (d-f) classified by Frohlich (1992) and the histograms for the number of strike-slip and thrust events as a function of focal depth (right panels of c and f). The moment tensor solutions of E1, E2, and E3 are illustrated in (a-c) with green, red, and blue compressional quadrants. The sub-regions of C1–C5 in (b) and (e) divided by blue lines represent the domains for the stress inversion (Fig. 2.9). The other symbols match those in Fig. 2.1.

2.6 Stress inversion

As mentioned in the previous section, the inverted focal mechanisms of the 263 events are mainly divided into strike-slip and thrust events under the homogeneous P-axis, and their spatial distributions are different from each other. One key observation is that thrust earthquakes rarely occur at depths deeper than $\sim$ 15 km, whereas strike-slip earthquakes occur at greater depths (e.g. the sub-region of C3 in Figs. 2.8b, c, e, and f). Another important observation is that thrust events are predominantly scattered in areas with depths shallower than 13.5 km and horizontal distances greater than 5 km on the A1–A2 profile (e.g. the sub-regions of C4 in Figs. 2.8b and e). The spatial heterogeneity of the fault types is indicative of the spatial heterogeneities observed in the tectonic stress field. To examine the heterogeneity in the stress field of the aftershock region, the study area is divided into five sub-regions in which the spatial distribution of the strike-slip and thrust events varies, and the stress inversion was performed for each sub-region (Fig. 2.9). The inversion was applied via the MSATSI software, which was redesigned from the conventional SATSI algorithm for use in the MATLAB environment (Hardebeck and Michael, 2006; Martínez-Garzón et al., 2014). No regularization for the spatial difference of the stress field is applied, and one fault plane from two conjugated planes is randoM_{L}y selected by considering the fault plane ambiguity. Detailed inversion parameters, such as the number of fault planes used and the direction of each principal axis, are presented in Fig. 2.9. Trends and plunges of the maximum stress components (σ_1) in all sub-regions are estimated as $\sim$ 260° N and $\sim$ 10°, respectively, which suggests that the maximum horizontal stress (σ_{Hmax}) is homogeneous in the study area. However, the intermediate stress field (σ_2) and the minimum stress field (σ_3) are not uniform in the five sub-regions. In the depth range less than 13.5 km, σ_2 in C1 and C4 corresponds to the minimum horizontal stress (σ_{hmin}) and the lithostatic stress (σ_v), respectively. At intermediate depths (13.5–15 km), the amplitudes of σ_2 and σ_3 are so close to each other that they cannot be well constrained (Fig. 2.9). For C3 at depths < 15 km, all the principal stress orientations

are well constrained due to the dominance of strike-slip events. The R values, defined as $(\sigma_1 - \sigma_2)/(\sigma_1 - \sigma_3)$, are equal to or greater than 0.75 throughout all sub-regions, suggesting that the aftershock region is in the transpressional regime (Bohnhoff et al., 2006).

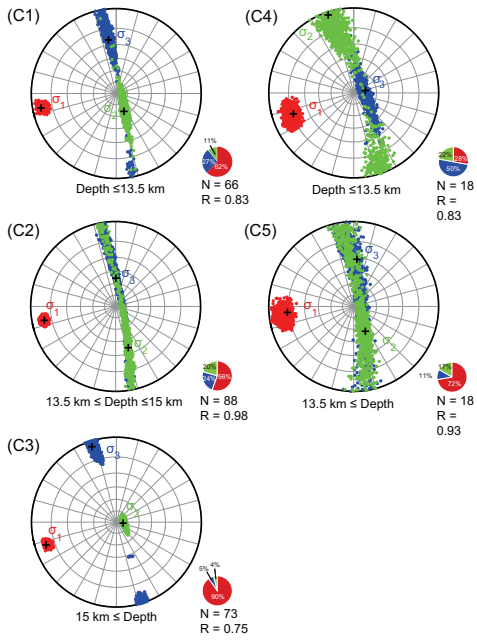

Figure 2.9: Stress inversion results for the events in the five different blocks (C1–C5). Firstly, the study area is divided into the left section (C1, C2, and C3) and the right section (C4 and C5) at the 5-km point on the A1–A2 profile. Then, each section is split into two or three subsections with different depth ranges. For each subplot, the depth ranges, relative stress magnitude (R), and number of focal mechanisms used (N) are shown below the inversion results. Each subplot is illustrated with a pie-chart representing the relative portions of strike-slip events (red), thrust events (blue), and other types of events (green). The three principal stress components ($\sigma_1 > \sigma_2 > \sigma_3$) are represented with 1,000 bootstrapping results. The maximum principal stress (σ_1) is well resolved with low uncertainty for all the subsections. Except for C3, the other principal stress components are not constrained due to the mixed population of strike-slip events and thrust events.

In C3, where σ_2 and σ_3 are clearly distinguished as the vertical stress and minimum horizontal stresses, the principal stresses normalised by vertical stress can be derived from the Coulomb Friction Law and the R value, with the assumption that excessive differential stresses would be released by slip along optimally oriented fault planes (Jaeger et al., 2009; Soh et al., 2018). Based on the frictional coefficient (μ) of 0.85 and the hydrostatic pore pressure, the relative minimum horizontal stresses (σ_{hmin}/σ_v) and the relative maximum horizontal stresses (σ_{Hmax}/σ_v) correspond to 0.70 and 1.94, respectively, which are consistent with the results of Soh et al. (2018). If μ varies from 0.6 to 1 following Byerlee's Law (Byerlee, 1978), σ_{hmin}/σ_v and σ_{Hmax}/σ_v have a range of 0.66–0.79 and 1.67–2.07, respectively. If we assume a unit weight of granitic rocks for the continental crusts (26.5 kNm^{-3}, Soh et al. (2018)), the values of σ_{Hmax}, σ_v, and σ_{hmin} at a depth of $\sim$ 16 km are estimated as 823, 424, and 297 MPa, respectively.

2.7 Stress transfer analysis

The 50-minute gap between the origin times of the E1 and E2 events and the 600–700 m offset of the two faults (F1 and F2) may indicate the static stress interaction in a multi-fault system. In other words, the perturbed stress field caused by the seismic activity on F1 may have affected the spatial and temporal distribution of earthquakes on F2, and vice versa. One of the favourable approaches with regard to the triggering of earthquake aftershocks is the Coulomb hypothesis, which explains the increased (or decreased) seismicity with regional static stress changes. For a specific receiver fault, the relationships among the Coulomb stress change ($\Delta\sigma_f$), shear stress change ($\Delta\tau$), normal stress change ($\Delta\sigma$), and pore pressure change (ΔP) on this fault are given as:

$$\Delta\sigma_f = \Delta\tau + \mu(\Delta\sigma + \Delta P) \tag{2.4}$$

where μ is the coefficient of internal friction, and unclamping is defined as positive for the normal stress (Lay and Wallace, 1995). If we use the apparent frictional coefficient $\mu\prime$ instead of μ, which involves both the effects of pore pressure changes and normal stress changes, then Eq. (5) can be rewritten as (Reasenberg and Simpson, 1992; King et al., 1994):

$$\Delta\sigma_f = \Delta\tau + \mu\prime\Delta\sigma \tag{2.5}$$

We applied two approaches for the Coulomb stress calculations via the Coulomb 3.3 software (Lin and Stein, 2004; Toda et al., 2005). Firstly, the Coulomb stress changes imparted by both E1 and E2 were analysed for optimally oriented strike-slip faults to resolve the temporal variation of the off-fault seismicity. The epicenters of detected events determined by the single difference method in Fig. 2.2 were compared with the Coulomb stress changes on the optimally oriented receiver fault for the maximum stress field in the N75°E direction, with a strength of 65 bars (Hong et al., 2017). We then calculated the Coulomb stress changes on F1, F2, and F3 from the E1 and (or) E2 slip models to check whether the static stress change of each fault plane correlates with off-fault seismicity. Following the scheme of Hong et al. (2017), the apparent frictional coefficient $\mu\prime$, Young's modulus, and Poisson's ratio were set to 0.4, 80 GPa, and 0.25, respectively. The finite rupture models of E1 and E2 from Uchide and Song (2018) were used to configure the slip amounts on the faults. Figure 2.10 illustrates the Coulomb stress changes on optimally oriented faults at a depth of 14 km generated by both E1 and E2 with the epicenters of all located earthquakes. In the region far from F1 and F2 (i.e. the area outside of the black box in Fig. 2.10), the seismicity increases within the area of positive Coulomb stress changes and decreases within the negative lobes. More specifically, the effects of the Coulomb stress changes were inversely proportional to the epicentral distances up to $\sim$ 50 km (see the upper right panel of Fig. 2.10).

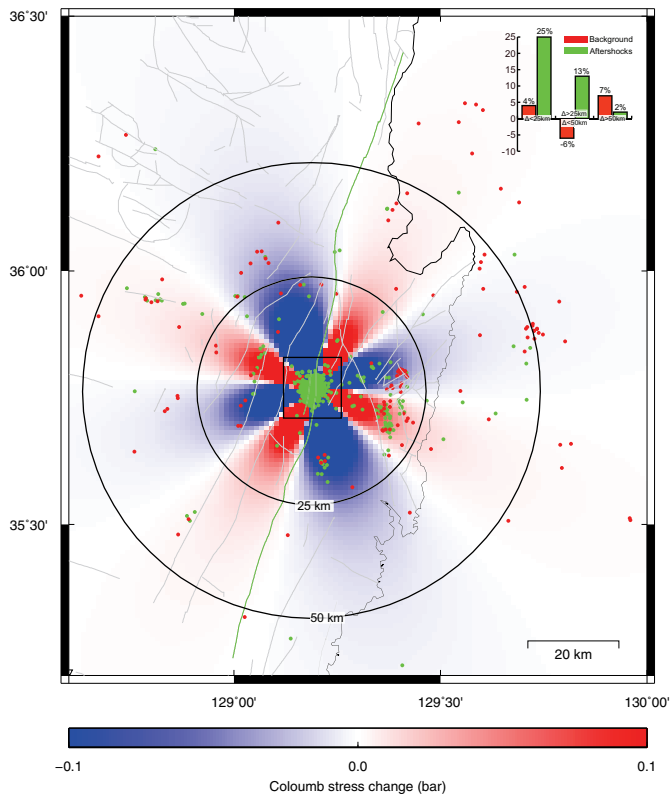

Figure 2.10: Coulomb stress changes on optimally oriented receiver faults at a depth of 14 km. Each sub-fault element is assumed to have an area of 1 $\times$ 1 km^2. The seismicity values before and after the onset of E1 illustrated in Fig. 2.3a are shown with red and green dots, respectively. The off-fault seismic activities are regarded as the earthquakes that occur outside the black box. For each epicentral distance bin, the percentage difference between the off-fault earthquake densities of the areas with increased Coulomb stress changes and those with decreased Coulomb stress changes is illustrated in the inset histogram. The other symbols match those in Fig. 2.1.

The calculated Coulomb stress change on F2b for the fault model of E1 gives a negative value at the loci of E2. However, an elliptical patch with positive Coulomb stress changes was observed near E2, not more than 500 m away (Fig. 2.11a). If the uncertainties of the finite slip model and relocated hypocenter are taken into account, the Coulomb stress changes by E1 may have advanced the occurrence of E2, although dynamic stress changes, fault geometries, and the regional stress state can affect the result (Gomberg et al., 2003). The fault model of E2 yields positive Coulomb stress changes on an inverted T-shaped area (Fig. 2.11b). The seismic activity on F1 for 5 hours after E2 overlaps with the area, implying that the Coulomb stress change caused by the occurrence of E2 may also have affected the seismicity on F1. Slips from both finite fault models of E1 and E2 result in positive Coulomb stress changes on the sinistral slip of F3 ($\sim$ 7 bar), which may indicate that the Coulomb stress changes imparted by the two largest events trigger the sinistral slip of E3 on a conjugate fault striking to the ESE–WNW direction.

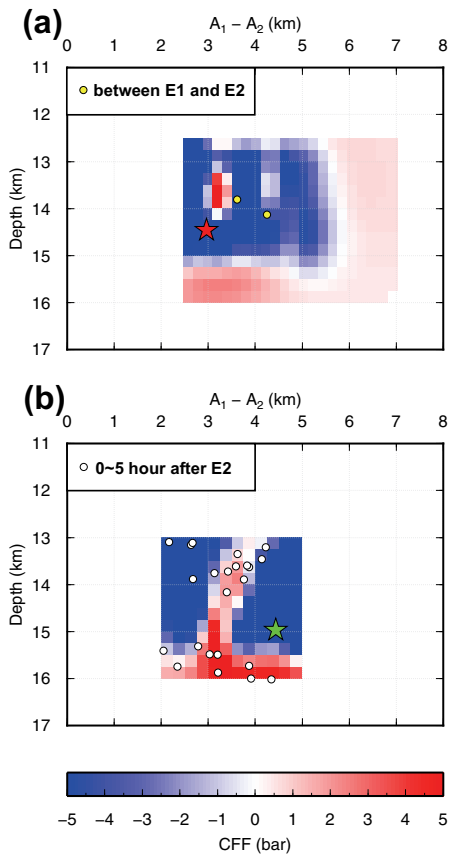

Figure 2.11: Coulomb stress changes imparted by the finite slip models of Uchide and Song (2018) on the sub-fault elements of other faults. (a) Coulomb stress changes on F2b caused by the finite slip model for E1. The seismic activities on F2 between the onsets of E1 and E2 are denoted as yellow dots. (b) Coulomb stress changes on F1 caused by the finite slip model for E2. Five hours of seismicity following E2 are shown as white dots. The green and red stars correspond to the locations of E1 and E2, respectively.

2.8 discussion

2.8.1 Fault system complexity

The detailed spatial distribution of the Gyeongju earthquakes represents the occurrence of E1 and E2 on two parallel fault planes of F1 and F2, with an offset of 600–700 m. Complex fault systems with two or more parallel faults can also be found in other regions (Durá-Gómez and Talwani, 2009; Rabak et al., 2010; Yano and Matsubara, 2017). Yano and Matsubara (2017) reported that part of the 2016 Kumamoto earthquake sequence was aligned on two vertical fault planes in the north-eastern area of Mt. Aso with two moderate-sized aftershocks ($M \geq 5$) located on either side of the fault plane. This is consistent with our results that major events in a sequence separately occurred on visually identified faults. The third largest event (E3), located at the south-western tip of the aftershock region, and a streak of earthquakes following E3 are aligned on F3, which is perpendicular to F1 and F2 (Fig. 2.3a). Conjugate fault systems can be found in many previous studies (2012 Sumatra earthquake, Meng et al. (2012); 2000 Wharton Basin earthquake, Robinson et al. (2001); 2000 Western Tottori earthquake, Fukuyama et al. (2003). In particular, the 2000 Western Tottori earthquake has characteristics similar to the Gyeongju earthquake in that relatively small conjugate faults ruptured at the tip of the main faults. The dip of F2 estimated from relocated earthquakes varies at a depth of $\sim$ 13.5 km (Fig. 2.3d). Therefore, we suggest that the fault plane is bent or that two distinct faults having different dips are crossing at the region. To check that an inaccurate velocity model affects the fault structure, various velocity models were tested, and significant changes were not observed.

2.8.2 Interactions between complex faults

The first couple of hours of spatio-temporal variations in seismicity on F1 and F2 are very characteristic. In the period between E1 and E2, most earthquakes are confined on F1 at a depth range of 15–16 km. Seismic activities on F1 abruptly diminished after

the occurrence of E2 for at least four hours (Fig. 2.3b). Instead, most of the earthquakes following E2 are located at depths shallower than 14 km. This is in contrast to the deep seismic activity on F1 before E2. The decreased seismicity on F1 starting from the occurrence of E2 cannot be fully explained by static stress changes because the Coulomb stress changes on F1 imparted by the finite slip model of E2 are positive in some areas (Fig. 2.11b). Therefore, other factors such as irregular fault geometry, heterogeneous elastic modulus, and complex stress states are required to explain it.

2.8.3 A possible microscale heterogeneity in the complex fault system

The b-values for F1 and F2 are almost unity, but the p-value for F1 is estimated to be significantly less than that of F2. The difference in p-values may result from the decreased seismicity of F1 after the occurrence of E2. To check the effect of initial earthquake sequences, the p-value for F1 was re-estimated after removing the earthquakes before E2. We confirmed that it remains at 0.96 ± 0.04, which is still less than those for all data sets and events on F2. Therefore, it is reasonable that the decay rate of the seismicity on F1 is generally slower than that on F2. Still, many factors can be attributed to the spatial changes in the p-values: stress, fault heterogeneity, and crustal heat flow (Wiemer and Katsumata, 1999; Enescu et al., 2011), requiring further analysis on this parameter in order to pinpoint the exact cause. The maximum M_{Rel} of the reverse fault earthquakes determined by focal mechanism inversion corresponds to 2.46. None of the fault types calculated from the moment tensor inversion has a thrust regime. Indeed, from the hypocenter distribution, no characteristic structure is identified along the NNE–SSW direction, the strike direction of the reverse faults. Therefore, the reverse fault events occur on smaller fault planes than those of the strike-slip events, and microcracks that cannot be identified by the hypocenter distribution may develop throughout the study area, generating the thrust events that occur in response to the heterogeneous stress field at each location.

2.8.4 Model Implication

Background seismicity around the study area is concentrated along mapped faults, which indicates that earthquakes occurred on pre-existing faults where local stress had accumulated, rather than at newly formed faults (Fig. 2.2a; Lee and Jin (1991); Han et al. (2017); Kim et al. (2017b)). The Gyeongju earthquakes ruptured beneath the Yangsan fault with a rupture length of 170–200 km and a horizontal offset of $\sim$ 30 km (Fig. 2.2a, Kyung (2003); Kim et al. (2017b)), but the general trend identified from the aftershocks is rotated clockwise by 15° from two mapped faults near the epicenters. Kim et al. (2018b) interpreted the angular difference as Riedel shears in a strike-slip duplex. However, we additionally identified F3 and thrust faults striking in different directions from the general trends. Therefore, a more complicated structure than the simple Riedel shears is needed to explain minor faults. The hypothesis proposed by Uchide and Song (2018) suggested that the fault rupture models for E1 and E2 occurred in a fault jog of extensional oversteps and the pull-apart stress between them would produce normal faults in the aftershock area. However, we did not observe normal faulting events; we suspect that the faulting types of the Gyeongju aftershocks are more likely to be affected by local stress fields and pre-existing faults, rather than by the directivity of rupture propagations.

2.9 conclusions

In this study, the source parameters of the Gyeongju earthquakes from three years of seismicity data near the aftershock zone were analysed using data from a temporary seismic network as well as two permanent seismic networks. For the three largest earthquakes with $M_{\mathrm{L}} > 4$, distinct fault planes at a depth of 12–16 km were identified. The two largest events (E1 and E2) occurred on two sub-parallel faults (F1 and F2) striking in the NNE–SSW direction, whereas the third largest event (E3) occurred on a vertical fault plane (F3) perpendicular to F1 and F2. The focal mechanisms estimated

from the first motions of the P-waves are composed of strike-slip events, thrust events, and intermediate types of events, which are not matched with an extensional fault jog and require modifications in the duplex strike-slip model. The strike-slip events are in accordance with the inverted moment tensors of the 10 selected events. The difference in the spatial distribution between the strike-slip events and thrust events indicates the heterogeneity between the minimum horizontal stress and lithostatic stress. In particular, reverse fault events are hardly observed deeper than 15 km, implying that the minimum horizontal stress is no longer greater than the overburden pressure below a depth of 15 km.

Table 2.1: Geometric parameters of the three major fault planes.

Fault ID	Width (km)	Length (km)	Min depth (km)	Max depth (km)	Area (km^2)	Strike/Dip (º)	Number of earthquakes
F1	3.1	3.0	13.0	16.0	9.3	26 / 65	507
F2a	2.4	5.5	11.5	13.5	13.2	26 / 55	541
F2b	3.7	5.5	12.5	16.0	20.4	26 / 69	1173
F3	0.7	1.0	15.3	16.0	0.7	116 / NA	34

Table 2.2: Source parameters of the ten earthquakes used in the moment tensor analysis.

Event ID	Event origin time (UTC; yy/mm/dd,hh:mm:ss.ss)	Latitude (ºN)	Longitude (ºE)	Depth (DD;MTI, km)[a]	Magnitude (M_W)	Strike(º)[b]	Dip (º)[b]	Rake (º)[b]	Double-couple component (%)	Maximum correlation
155 (E1)	16/09/12, 10:44:33.04	35.768	129.196	15.0; 14	5.14	27 / 297	71 / 89	-179 / -18	82	0.98
191 (E2)	16/09/12, 11:32:54.55	35.755	129.193	14.5; 12	5.57	24 / 117	70 / 82	171 / 19	75	0.98
331	16/09/12, 14:18:28.55	35.761	129.172	15.3; 14	3.07	24 / 292	80 / 80	-170 / -9	78	0.62
354	16/09/12, 14:52:31.06	35.761	129.190	13.5; 11	3.21	30 / 298	79 / 81	-171 / -10	79	0.75
561	16/09/12, 23:24:48.34	35.756	129.183	13.0; 11	3.23	28 / 119	80 / 82	171 / 9	87	0.73
1631 (E3)	16/09/19, 11:33:58.81	35.745	129.185	15.8; 14	4.46	32 / 301; 30 / 120	72 / 85; 70 / 90	-174 / -17; 180 / 20	82	0.98
1761	16/09/21, 2:53:55.13	35.759	129.191	13.8; 12	3.43	25 / 295; 30 / 120	79 / 89; 85 / 81	-179 / -10; 171 / 5	97	0.91
2167	16/10/02, 11:53:07.96	35.752	129.198	15.4; 15	2.98	17 / 107; 10 / 110	62 / 89; 53 / 77	179 / 27; 164 / 38	91	0.62
2314	16/10/10, 13:59:10.61	35.753	129.191	14.4; 15	3.30	27 / 121; 36 / 133	62 / 83 ; 64 / 75	172 / 27; 164 / 27	97	0.79
2884	16/12/12, 08:53:18.14	35.758	129.189	13.2; 11	3.22	26 / 295	81/ 84	-174 / -8	95	0.77

[a]The depth of each event is calculated from both the Double-Difference (DD) relocation and the moment tensor inversion (MTI).

[b]If we obtain the focal mechanism of an event using the first P-wave motions, we ordinarily describe the fault parameters obtained from the waveform inversion and first P-wave motions.

Chapter 3

Migrating earthquake clusters observed in 2016 Gyeongju earthquake sequence

Copyright – The materials in this chapter will be submitted to a journal as “Migrating earthquake clusters observed in 2016 Gyeongju earthquake sequence ” (draft title) by Woo *et al.*. I briefly described preliminary results on this topic.

3.1 Brief summary

In this chapter, I provided a summary of the procedures and results on the detailed source analysis of subset of Gyeongju earthquake sequences. The subset consists of $\sim$ 30 earthquakes that migrated to the SW direction at the edge of the aftershock area. From the principal component analysis, I obtained an optimal fault plane for the sequences and relocated the earthquake with cross-correlation measurements. The earthquake magnitudes were relatively measured from the amplitude-magnitude scaling relationship. Since they are located very similar area within 70 m, their source mechanisms can be analyzed by de-convolving empirical Green's functions (eGfs) of smaller earthquakes from relatively largest earthquakes. Since their magnitudes are less than M_{L} 2.4, it is required to obtain seismic data with high sampling rate and the seismograms gathered from temporary seismic stations installed by a team of Seoul National University, Pukyong National University, and Pusan National University can be usefully applied to this analysis. I applied finite fault inversions following the method suggested by Dreger et al. (2007) and obtained slip images for two large earthquakes with $M_{\mathrm{L}} \geq 2.0$. The peak slip were observed as $\sim$ 4 cm and the obtained stress drop ranges up to 50 MPa, which is considered to be very high compared with two largest earthquakes in the Gyeongju aftershock sequences (Uchide and Song, 2018). The high stress drop suggests that the rupture may not be coincided with each other in the cluster. Therefore, the earthquake in the clusters can be considered to be ruptured at difference asperities. More detailed discussions are required to the interpretations of the temporal migrations.

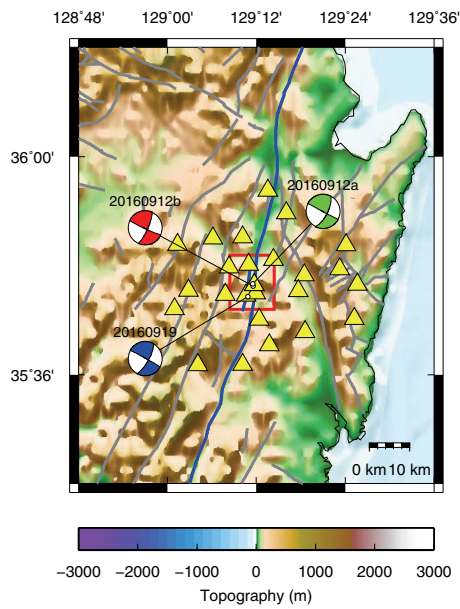

Figure 3.1: The distribution of temporary seismic stations used in the study. The focal mechanisms of three largest earthquakes are illustrated. Major geological lineaments and faults are denoted as gray lines. The Yangsan fault, which crosses throughout the Gyeongsang basin is highlighted as a blue line.

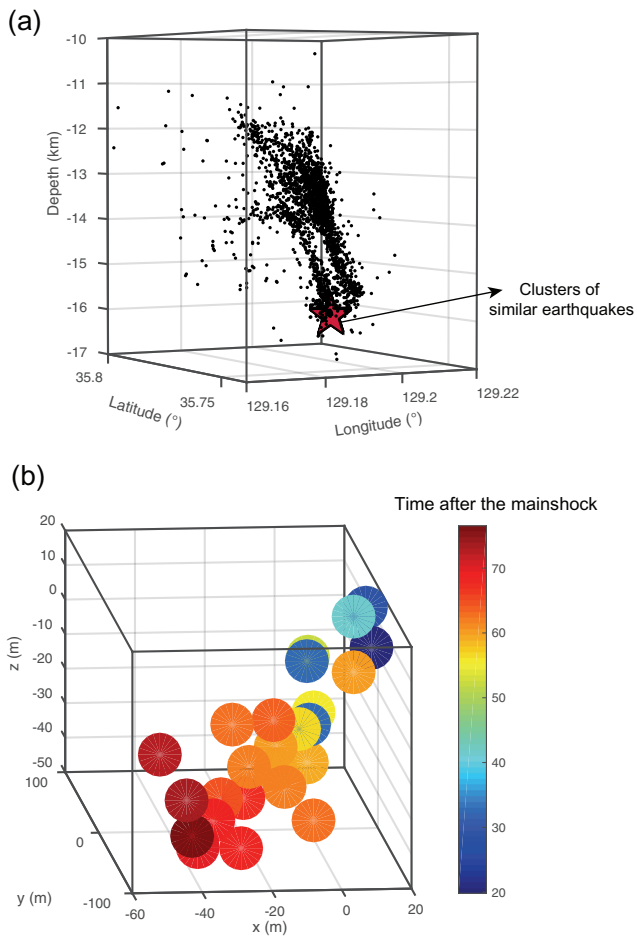

Figure 3.2: (a) The spatial distribution of aftershocks and the location of the earthquake cluster (red star). (b) A zoomed-in 3-D view for the hypocenters in the cluster.

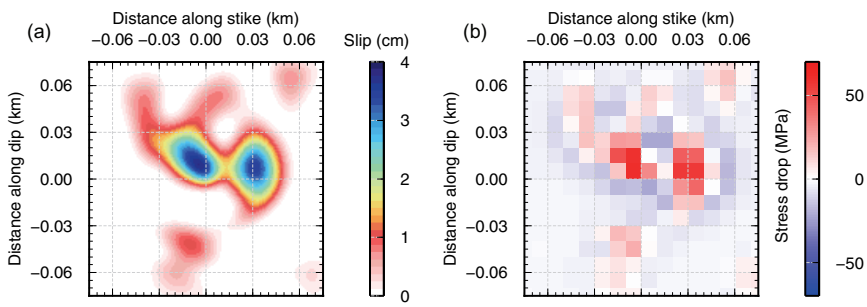

Figure 3.3: (a) The slip distribution of the largest earthquake (ID 1597) in the clusters obtained from source time functions deconvolved by nearby empirical Green's functions. (b) The distribution of stress drop.

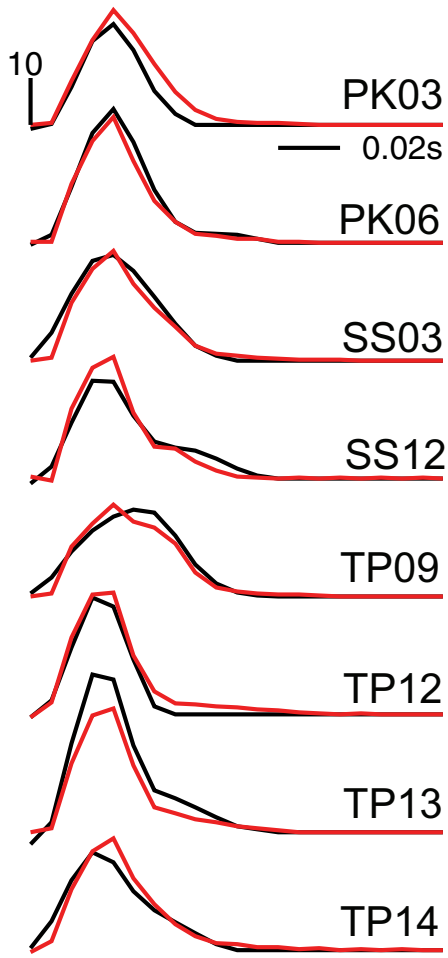

Figure 3.4: (a) The source time functions for the earthquake of ID 1597 obtained from deconvolution method.

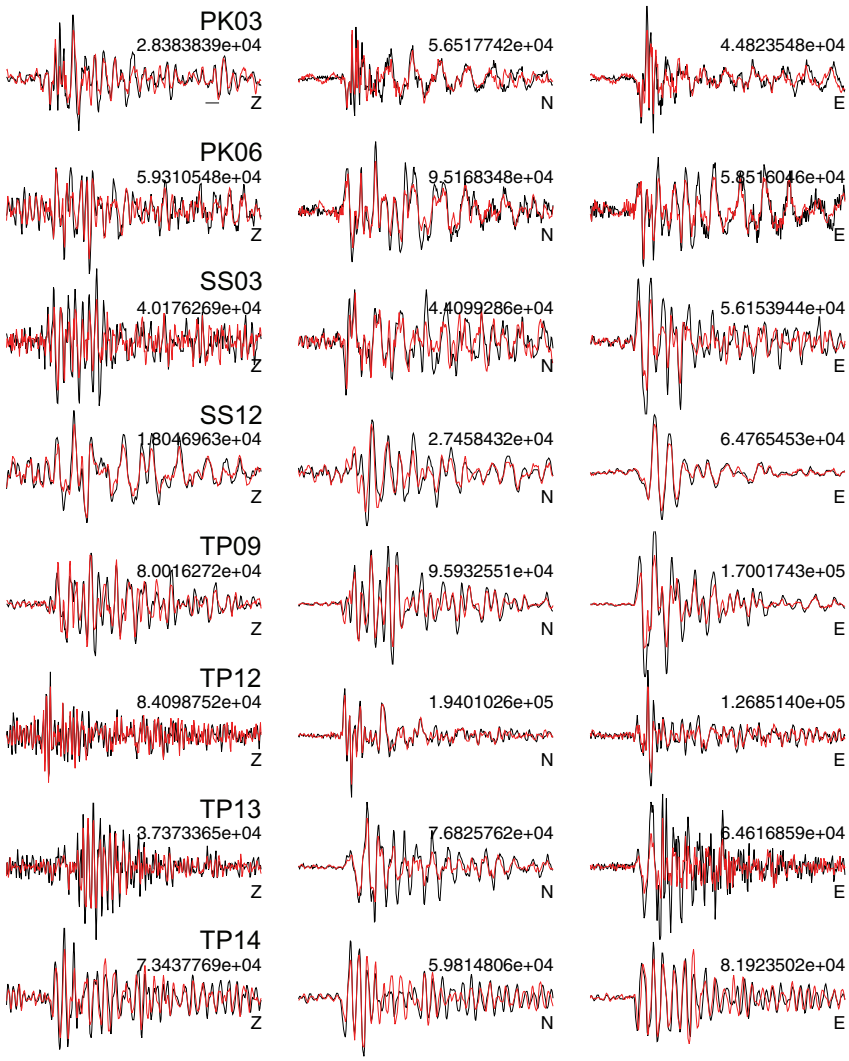

Figure 3.5: (a) The observed (red) and synthetic (red) waveforms for the slip model of Fig. 3.3.

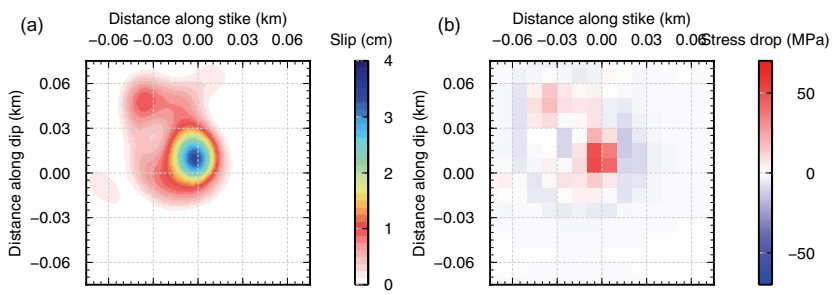

Figure 3.6: The slip distribution of the second largest earthquake (ID 1598) in the clusters obtained from source time functions deconvolved by nearby empirical Green's functions. (b) The distribution of stress drop.

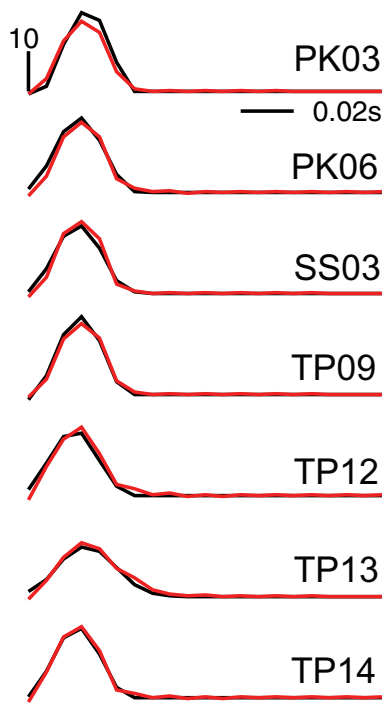

Figure 3.7: The source time functions for the earthquake of ID 1598 obtained from deconvolution method.

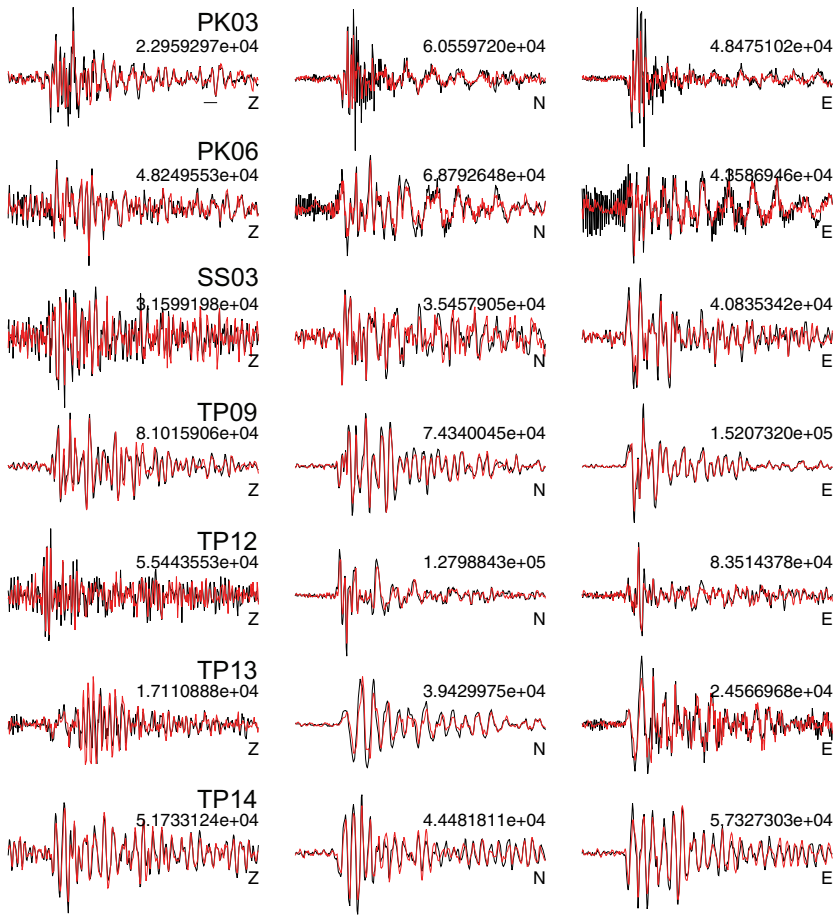

Figure 3.8: The observed (red) and synthetic (red) waveforms for the slip model of Fig. 3.6.

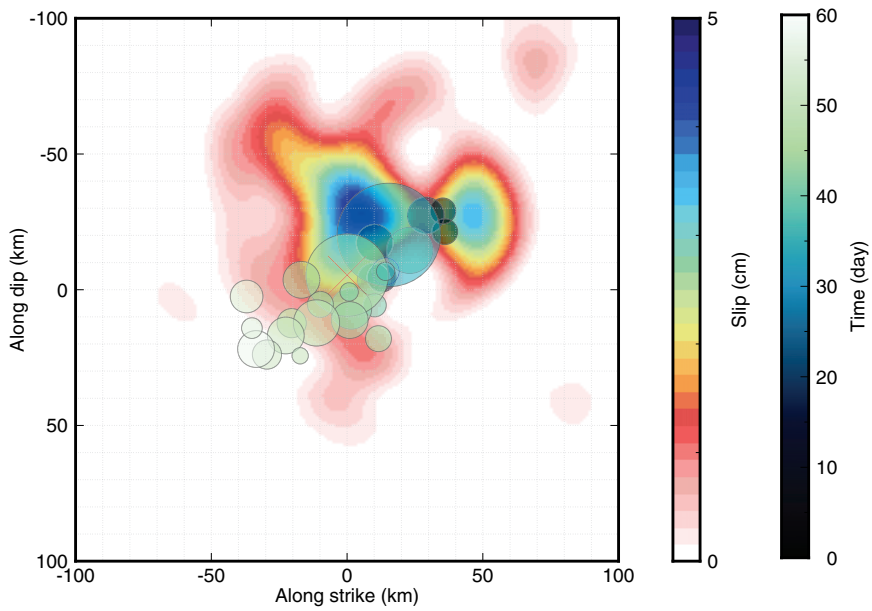

Figure 3.9: Temporal migrations of earthquake projected on the best fitting fault plane. Two slip distribution of Fig. 3.3 and Fig. 3.6 were overlaid after stacking.

Chapter 4

An in-depth seismological analysis revealing a causal link between the 2017 M_W 5.5 Pohang earthquake and EGS project

This chapter is based on a paper entitled "An in-depth seismological analysis revealing a causal link between the 2017 M_W 5.5 Pohang earthquake and EGS project" by Woo, J.-U., Kim, M., Sheen, D.-H., Kang, T.-S., Rhie, J., Grigoli, F., Ellsworth, W.L., and Giardini, D., which was published in Journal of Geophysical Research: Solid Earth.

4.1 Introduction

The 2017 Pohang earthquake of moment magnitude (M_W) 5.5 struck Pohang, South Korea, on November 15, 2017, at 05:29:31 UTC (hereinafter, the Pohang earthquake) (Grigoli et al., 2018; Kim et al., 2018c; Lee et al., 2019b). The magnitude of the earthquake is the second largest in the Korean Peninsula since official earthquake monitoring was first initiated in 1978 by the Korea Meteorological Administration (KMA). However, it is an earthquake that inflicted the most damage in the region (Choi et al., 2019; Kang et al., 2019). Concerned authorities suspected that the enhanced geothermal systems (EGS) geothermal electricity project caused this earthquake (Lee et al., 2019b; Ellsworth et al., 2019). In the project, two geothermal wells, PX-1 and PX-2, with a depth of over 4 km were drilled to expedite water circulation through hot dry rock characterized by artificially enhanced permeability induced by hydraulic stimulation (Kim et al., 2018c; Hofmann et al., 2019). Through these geothermal wells, the EGS project team conducted five hydraulic stimulation experiments (Kim et al., 2017a). The Pohang earthquake occurred approximately two months after the completion of the final hydraulic stimulation experiment (i.e., September 18, 2017).

For various reasons, fluid injections can induce seismicity (Ellsworth, 2013). EGS projects, such as in the Pohang case, require fluid injection processes at high pressures through deep boreholes of a few kilometers (Zang et al., 2014). Such high pressure exerted on the surrounding rock during fluid injection causes cracks that increase the permeability of the rock mass, thus making it easy to extract heated fluid from deeper areas according to the geothermal gradient. This crack-forming process can induce seismicity (Ellsworth, 2013; Maxwell, 2014). Therefore, several studies have questioned the relationship between the occurrence of the 2017 Pohang earthquake and activities of the EGS project (Grigoli et al., 2018; Kim et al., 2018c). However, the magnitude of the Pohang earthquake was much larger than the expected magnitude estimated based on known relationships (McGarr, 2014; Van der Elst et al., 2016; Galis et al., 2017), which has provoked a heated debate (Lee et al., 2019a,b). For refer-

ence, the two largest events related to the EGS project prior to the Pohang earthquake were the 2006 M_W 3.4 Basel earthquake in Switzerland and the 2003 M 3.7 Cooper basin earthquake in Australia, where the released seismic moments were only 0.07 and 0.20% of the seismic moment of the Pohang earthquake (Deichmann and Giardini, 2009; Baisch et al., 2006).

The purpose of this study is to provide a detailed analysis of the seismic activity that occurred near the Pohang EGS site and reveal the relationship between seismicity and injection activities. We have developed a one-dimensional (1-D) seismic velocity model for the EGS project site to better analyze the seismicity of the area. Furthermore, we introduce a series of precise analyses on the seismicity before and during the entire period of the hydraulic stimulation experiments and the Pohang earthquake. These analyses include the absolute and relative locations, magnitude determination, and focal mechanism inversion of each seismic event. The results of these analyses were used for the investigation of the spatiotemporal distribution of seismic activity in and around the EGS project site, as well as to infer the fault geometry responsible for the mainshock. Finally, the hypocenter distribution was described in terms of the state of the geothermal wells to scrutinize the possible relationship between the hydraulic stimulation experiments and seismic activity.

4.2 Materials and methods

4.2.1 Geological tectonic setting

The epicenter of the Pohang earthquake was located in the Pohang basin, which is in the southeastern part of the Cretaceous Gyeongsang basin formed during the Miocene epoch. The geology of the epicentral area in the northeastern Pohang basin can be described as Quaternary alluvium overlying sandstone and mudstone of the Tertiary Yeonil Group (Fig. 4.1a). The Pohang basin developed from transtensional subsidence related to NNW-SSE trending dextral shear movements that acted along

the eastern coast of the Korean Peninsula with the opening of the East Sea (Sea of Japan). This was accompanied by the separation of the Japanese Island Arc from the far-eastern margin of the Eurasian continent, including the Korean Peninsula, in the Miocene (Son et al., 2015). Basement rock beneath the Pohang basin is composed of granitic rocks and a complex of gneisses and schists that form the Yeongnam massif (or Sobaeksan massif) (of Korea, 1998; Lee and Cho, 2012).

Several dominant types of faults bound the Pohang basin, i.e., NE- to NNE-trending normal faults and NW-trending transfer faults to the west, NNW-trending dextral strike-slip faults to the south, and NE- to NNE-trending sinistral strike-slip to dip-slip faults (Son et al., 2002; Cheon et al., 2012; Son et al., 2015). Among these faults, the Gokgang fault near the epicenter is known to be a normal fault with a NE strike and SE dip (Fig. 4.1b; Yun (1994)). Recent outcrop observations have shown that, although the antithetic faults have similar strikes with the Gokgang fault, the NW dips have formed a conjugate normal fault system in this area (Choi et al., 2019). Considering that the southeastern part of the Korean Peninsula is exposed to maximum compressional stress in the ENE-WSW direction (Chang et al., 2010), faults with a normal-faulting sense related to the evolution of the Pohang basin can be reactivated in a reverse-faulting scenario when exposed to the current stress field.

4.2.2 Data acquisition

The purpose of this study is to investigate the mainshock and earthquakes that have occurred near the EGS site. We used the seismic waveform recorded at three different seismic networks to analyze earthquakes. The first network was a permanent network operated by the KMA, the Korea Institute of Geoscience and Mineral Resources (KIGAM), and the Korea Hydro and Nuclear Power (KHNP), which are denoted as KS, KG, and KN, respectively. This network consists of broadband velocity seismometers, short-period velocity seismometers, and accelerometers (Fig. 4.1a). We mainly used stations located within approximately 50 km of the mainshock epicen-

ter for the analysis but also used stations farther afield for the magnitude estimation of the mainshock and for the determination of the focal mechanism solutions of several events. The second network was a temporary network deployed as part of the EGS project, consisting of various instruments: 1) Eleven surface velocity seismometers (PH surface in Fig. 4.1), 2) nine borehole seismometers installed at depths between 100 and 150 m (PH borehole in Fig. 4.2), 3) a borehole geophone array deployed in PX-2 at depths between 1,360 and 1,520 m, with an interstation distance of 10 m (17 sensors), which operated for one month from July 2017, 4) a vertical seismic profile (VSP) installed in PX-1 and PX-2 at depths between 1,350 and 1,550 m, which partly operated during the first, second, and third stimulations (from January 27, 2016, to February 2, 2016, from December 24, 2016, to January 11, 2017, and on April 5, 2017), and 5) a surface (POH01) and borehole seismometer (BH4) installed at a depth of approximately 2,300 m and located approximately 2 km SW of PX-2 (Figs. 4.1b and 4.2a). The last network was a temporary network (PH short-period) installed after the third stimulation (Kim et al., 2018), which consisted of eight short period velocity seismometers located within 3 km of the mainshock epicenter (Fig. 4.1b). Detailed information on the seismic stations used in this study is summarized in Fig. A.1 and Table A.1. In addition to the seismic waveforms, detailed information on the fluid injections from the EGS project team were collected to obtain the relationships between the earthquakes and injections (Figs. 4.3 and A.2–A.6).

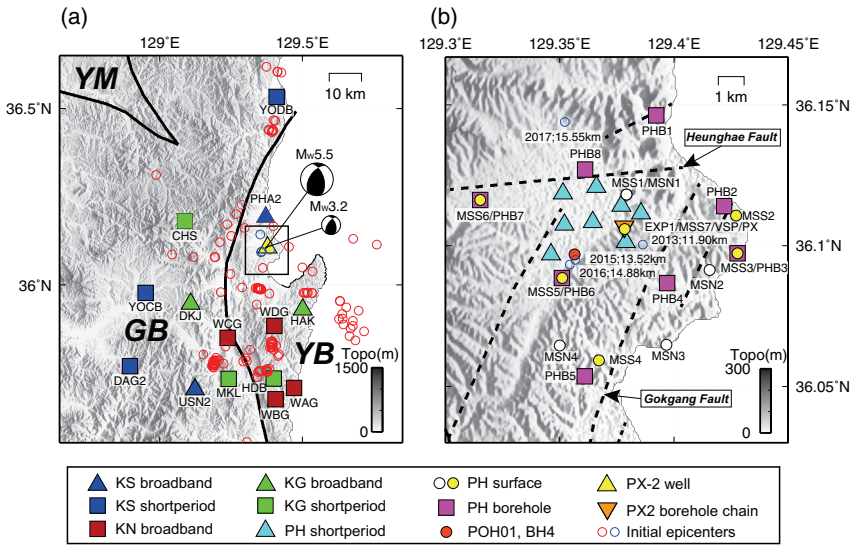

Figure 4.1: (a) Locations of permanent seismic stations used in this study, 140 earthquakes whose epicentral distances from the PX-2 well were more than 5 km (red circles), and 4 earthquakes whose epicentral distances from the PX-2 well were less than 5 km and focal depths deeper than 10 km (blue circles). Major tectonic provinces are separated by thick black lines: YM (Youngnam Massif), GB (Gyeongsang Basin), and YB (Yeonil Basin). The black box is the domain of (b). The focal mechanisms of the two largest events in our earthquake catalog are illustrated. (b) Locations of temporary stations used in this study. Origin years and focal depths of the earthquakes illustrated as blue circles of (a) are also shown. Mapped geological faults and lineaments are denoted by thick dashed lines (Lee et al., 2019a).

4.2.3 Construction of a local 1-D velocity model

Seismic source parameters, such as hypocenters, focal mechanisms, seismic moments, and stress drops, were accurately estimated by constructing an appropriate seismic velocity model. As the Pohang EGS site is situated in Pohang basin, which is expected to have significantly low-velocity layers with shallow depths, hypocentral parameters calculated via a regional velocity model that reflects the average medium properties may result in improper interpretations of the relationship between hydraulic stimulation and seismicity at the EGS site. Therefore, to avoid such misapprehensions, we must develop a local velocity model that represents the study area.

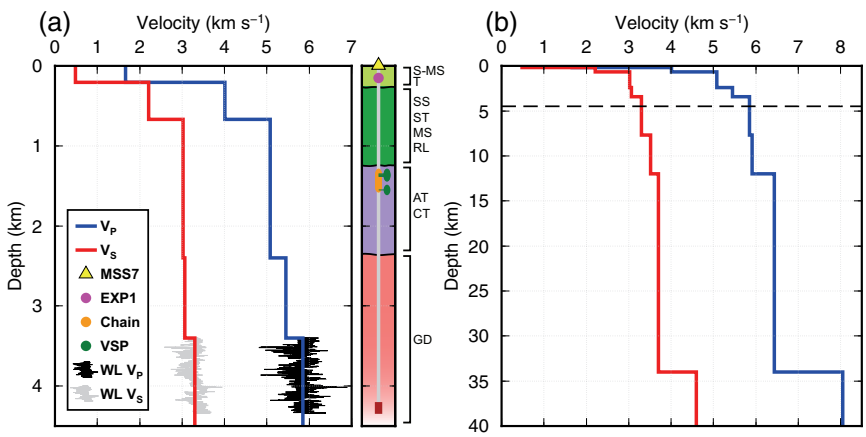

Figure 4.2: Local 1-D velocity model developed for two different depth ranges in this study. Blue and red lines represent the P- and S-wave velocity models, respectively. Vertical distributions of the borehole stations along the PX-2 well are illustrated in the right panel of (a). The PX-2 borehole chain stations are co-located with three VSP stations at depths of 1,360, 1,370, and 1,380 m but are operated for different stimulation periods from the VSP stations. The open section of PX-2 is colored in dark red. A simple geological model modified from Lee et al. (2015) is illustrated in the right panel of (a): S-MS (semi-consolidated mudstone), T (tuff), SS (sandstone), ST (siltstone), MS (mudstone), RL (rhyolite), AT (andesitic tuff), CT (crystal tuff), and GD (Granodiorite). The dashed line in (b) represents the lower depth limit of (a). Well logging data used to determine the P- and S-wave velocities of the fifth layer are overlapped to (a).

We developed a 1-D local velocity model that represents the EGS site based on geological strata observed from drilling cores of the stimulated wells, as well as seismological observations based on active and passive sources (Fig. 4.2). In the layered model, local anisotropy, which can perturb the stress field and affect fault instability (Magnenet et al., 2017), was not introduced. Lithologic variations in core samples provide us with information on seismic discontinuities between layers where there are abrupt changes in the stiffness or elastic moduli of the rock (Lee et al., 2015). The P- and S-wave velocities of each layer were determined from either seismic sources with assumed locations or well-logging data (Figs. 4.1b and 4.2a). For depths below 4.5 km, with no geological data, we adopted the regional model representing the Gyeongsang basin reported in Kim et al. (2011). The constructed 1-D velocity model for the Pohang EGS site was composed of seven layers and a half space. The final seismic velocity model and procedures to construct the model are summarized in Table A.1 (see A.1, available in the electronic supplementary material). The topmost layer of our model had slow P- and S-wave velocities and a high Vp/Vs ratio compared with the other layers. The obtained seismic velocities and thickness of the shallowest layer were matched with semi-consolidated sedimentary rocks deposited from 200–400 m at the surface of sedimentary layers with volcanic intrusions. This was analyzed with a deep borehole drilling project implemented near the Pohang EGS site (Lee, 2003; Lee et al., 2015).

4.2.4 Earthquake detection

Before analyzing the source parameters of the recent earthquakes, we detected the earthquakes that occurred near the EGS site before the occurrence of the mainshock using a template-matching method Shelly et al. (2007); Zhang and Wen (2015); Kato et al. (2016). This method uses templates based on the observed waveforms to find similar waveforms using a waveform cross-correlation between the template and continuous waveforms recorded at an identical station. The advantage of this method is that it can be applied even when the signal-to-noise ratio (SNR) is not high. We se-

Table 4.1: Local 1-D velocity model for the Pohang EGS site.

Top of the layer (km)	P-wave velocity (km/s)	S-wave velocity (km/s)	Vp/Vs ratio	Ramark
0.000	1.67	0.48	3.48	Reflection survey and PS time differences for an event (February 2, 2016; 15:01:34 UTC) between a surface seismometer and borehole sensor
0.203	4.01	2.21	1.81	Reflection survey and rock properties
0.67	5.08	3.03	1.68	Phase arrival times and check shots
2.4	5.45	3.07	1.78	Measurement of the least arrival time error
3.4	5.85	3.31	1.77	Well-logging data
7.7	5.91	3.51	1.68	Upper crust of regional model from Kim et al. (2011)
12.0	6.44	3.70	1.74	Lower crust of regional model from Kim et al. (2011)
34.0	8.05	4.60	1.75	Uppermost mantle of regional model from Kim et al. (2011)

lected the waveforms for 39 events as the templates (Table A.2), including five immediate foreshocks that occurred before the mainshock, which we have clearly identified as earthquakes. As large events can easily be identified due to their high SNR, the main purpose of the template-matching method is to detect small events. Therefore, we selected well-recorded waveforms as the templates from small events.

To detect events that occurred before and during the stimulation, we used the continuous waveform recorded at PHA2 (or PHA; the official name of the seismic station had been changed but hereafter, for convenience, we only refer to it as 'PHA2') from January 1, 2009, until the mainshock occurrence. PHA2, which is operated by the KMA, is the closest station to PX-2 among the permanent stations operated over an extended period. PHA2 is located approximately 10 km north of PX-2. We used the short-period records with a sampling rate of 100 Hz. For comparison, HAK, which is operated by the KIGAM, is the second closest station to PX-2 but the distance is approximately 23 km, which is more than twice as far as PHA2. Therefore, to achieve consistent results, we only used data from PHA2 for earthquake detection.

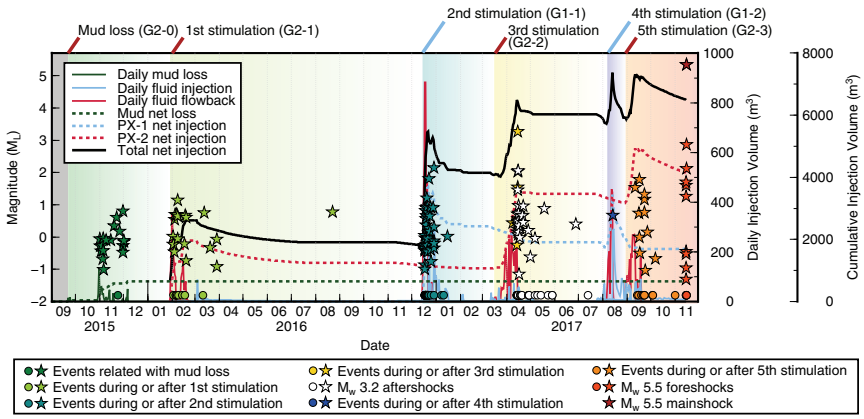

Figure 4.3: Seismicity at the Pohang EGS site and daily cumulative injected volume. The amount of heavy mud loss from PX-2 at a depth of 3,800 m in 2015 is included in the total net injection volume. The beginning of heavy mud loss and the five stimulation periods are illustrated at the top of the graph. The events without magnitude measurements are denoted by circle symbols. The events whose magnitudes are estimated from either assumed or known locations are denoted by star symbols.

The time window for the template waveform was defined as four seconds, from one second before the arrival time of the S wave. The bandpass filter between 5 and 20 Hz was simultaneously applied to the template and continuous waveforms before the waveform cross-correlation. On a daily basis, the correlograms calculated for the three seismogram components were averaged to increase the SNR and median absolute deviation (MAD) of the averaged measured correlogram. The criterion for the detection was set to 14 times the MAD, and we identified 3,547 event candidates. Candidate waveforms were visually inspected to remove false positives and overlapping events, and to screen out seismicity near the EGS site. In this step, waveforms recorded at the other stations were also used to increase the confidence in the detection and categorization. The matched filter did not detect the mainshock because a large magnitude difference between the mainshock and template events break the waveform similarity and render template matching impossible. Finally, we created an initial catalog of 520 earthquakes after adding the mainshock. Figure 4.3 illustrates the temporal distribution of the events that were spatially correlated to the Pohang EGS site.

4.3 Seismic source parameter analysis

4.3.1 Hypocenter determination

Three steps were taken to accurately determine the hypocenters. The first and second steps were the single and double difference methods, respectively, which are widely used in seismology to determine hypocenters. For convenience, we refer to the hypocenters determined by the first and second steps as the initial and relative locations, respectively. In the last step, we shifted the relative locations by considering the difference between the relative location and hypocenter as determined by an individual method for the one specific event that occurred on August 13, 2017, at 21:42:37 UTC (hereafter, referred to as the key event). We defined the shifted relative locations as the final locations.

4.3.1.1 Initial locations

Classic absolute location methods are based on the minimization of time residuals between the theoretical and observed arrival times of body waves (i.e., generally the first P and S onsets) through iterative inversion algorithms. In this study, we used Hypoellipse (Lahr, 1999) to determine the initial locations. We collected all data recorded at operating seismic stations based on the origin times of 520 events and manually picked the P- and S-wave arrival times. We calculated the initial locations when more than four P- and S-wave arrival times were available. The stations located at depths below the bottom of the top layer in the velocity model (e.g., VSP stations, PX-2 borehole chain, and BH4 station) were not used as the arrival times could not be precisely adjusted using elevation corrections in Hypoellipse.

Among the earthquakes in the initial catalog, the 253 initial locations were calculated. These events were then divided into three groups in terms of their epicentral distances from PX-2, as well as their focal depths. The first group consisted of 140 events with epicentral distances larger than 5 km and a maximum epicentral distance of 62 km (i.e., red open circles in Fig. 4.1). There were four events in the second group that occurred in the years 2013, 2015, 2016, and 2017 (i.e., blue open circles in Fig. 4.1). The third group had 109 events with epicentral distances and focal depths less than 5 km and shallower than 10 km, respectively. Considering their large epicentral distances and deep focal depths, it is unlikely that events characterized as either the first or second group were directly related to stimulation of the EGS project. As the main motivation of this study is to clarify the relationship between hydraulic fluid injection and earthquake sequences at the EGS site, we focused on the third group and performed additional analyses for 109 events in that group.

4.3.1.2 Relative locations

To relocate the relative locations from the initial locations, we used the double-difference method, which finds the hypocenters that minimize the residuals between

the theoretical and observed travel time differences of event pairs observed at a common station. We determined the relative locations of 98 events using HypoDD (Waldhauser and Ellsworth, 2000) after excluding 11 events whose travel time measurements were less than eight or whose relative travel time measurements are less than nine, to increase the reliability of the results. The stations located below the first layer were not used again. To maximize the performance of the double-difference method, precise measurement of the travel-time differences among the different events recorded at the same station is important. If two events recorded at the same station have similar hypocenters and focal mechanisms, the waveform cross-correlation can be used to precisely measure the differential travel times. We selected a 1-s time window (–0.5 to 0.5 s) from the manually picked arrival times of the P- and S-waves, increased the sampling rate to 1,000 Hz using cubic spline interpolation, and applied bandpass filtering between 2 and 10 Hz before the cross-correlation. If relative travel-time measurements using cross-correlation are not possible, the relative travel times can be simply calculated from the arrival times used to determine the initial locations. The damped least square QR (LSQR) algorithm was used for the inversion. The error associated with the relative locations was estimated with two individual methods, which are described as follows. First, the synthetic relative travel time data were reproduced by randomly sampling the residuals of the relative travel times calculated using the LSQR and then inverting them a second time. This process was repeated 200 times, such that the errors were estimated via a statistical analysis. Second, a linear equation was constructed using the residual of the relative travel times obtained from the last iteration in the inversion and the estimated least square error using the singular value decomposition (SVD) method. The average 2σ errors of the relative locations in the east, north, and upward directions estimated using the two methods were 20, 13, and 25 m and 15, 10, and 19 m, respectively, showing that the difference in the error estimated using the two methods was not significant.

4.3.1.3 Key event hypocenter determination and final locations

Among the relocated events, the key event on August 13, 2017 (M_W 1.2), was the only event recorded by both the surface stations and a linear vertical array of 160 m that consisted of 17 three-component geophones (group interval of 10 m) deployed in the PX-2 well at a depth of 1,360 m (see supplementary material for more details). The borehole array operated from July 26, 2017, to August 23, 2017, during stimulation operations in the PX-1 well. To process the data recorded with this tool, we must use an ad hoc technique. To locate the key event, we applied a combination of techniques based on array processing and polarization analysis (see supplementary material for details). As a first processing step, we reoriented the borehole array using the approach proposed by Grigoli et al. (2012) and Krieger and Grigoli (2015). We then located the events using the Principal Component Analysis (PCA) technique to estimate the back-azimuth and incidence angle (Noda et al., 2012; Eisermann et al., 2015). Finally, we used the PS time to obtain an estimation of the source-receiver distance that, combined with the azimuth and incidence angle, allowed us to obtain the absolute location of the seismic event. We further constrained the depth of the key event using the PS times of both the shallowest and deepest geophones and tube waves generated at the bottom of the cased well (see supplementary material for further details). The latitude, longitude, focal depth, and origin time of the event were determined as 36.1117°, 129.3734°, 4.210 km, and August 13, 2017, at 21:42:37, respectively. As similar waveforms were recorded by the vertical array seismometers in the PX-2 wellbore, as well as the use of several independent data to evaluate the hypocenter (i.e., travel time, particle motion, and tube waves), the location of the key event was assumed to be the most reliable among the hypocenters of all events. Therefore, this result was used to determine the final locations. The key event determined from the records at the PX-2 borehole chain was located 3 m east, 430 m north, and 161 m vertically upward of its relative location. We shifted the relative locations of all events by the given values to determine the final locations. Most final epicenters were located NW of the PX-2 and distributed

along NW-SE and NE-SW trends (Fig. 4.4). The latitude, longitude, and depth of the mainshock were determined as 36.1061°, 129.3726°, and 4.270 km, respectively. All final focal depths were in the range of 3.5–4.5 km.

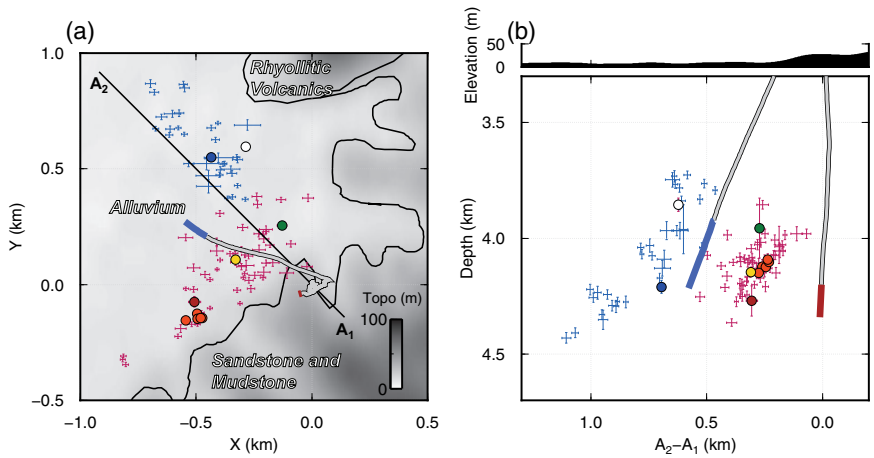

Figure 4.4: (a) Final epicenters of 98 earthquakes with their relative location uncertainties. An event in the M_W 0.9 mud-loss period, the M_W 3.2 event in the third stimulation, the M_W 1.2 key event used for the final location, five immediate foreshocks, and the M_W 5.5 mainshock are denoted by green, yellow, blue, orange, and red circles, respectively. The M_W 2.0 event that occurred on September 11, 2017, which is the only event that had a mismatched origin time and location compared with the stimulation history, is denoted by a white circle. The location uncertainties of the events related to the PX-1 and PX-2 injections are shown in blue and red. The trajectories of the PX-1 and PX-2 wells are shown as two gray curves with two open sections in blue and red. The origin of the coordinate is set to the location of PX-2. The divisions of the geologic formations are from Song (2015). (b) Cross-section of (a) along A1–A2.

4.3.2 Magnitude determination

We must consider the size distribution of the earthquakes (i.e., the magnitudes) to evaluate the seismic activity in a target region. Among the earthquakes identified by the template-matching analysis, the local magnitude (M_L) and M_W of the events, which are considered to be near the EGS site (i.e., the hypocenters are within 5 km of PX-2 or the observed PS times at PHA2 are within 2 s), were determined to quantify the seismicity at the EGS site.

The magnitude scaling relationship proposed by Sheen et al. (2018) was applied to the vertical component to determine the M_L. However, even the permanent seismic stations in South Korea, many of which are conventionally used to measure M_L, show large deviations in terms of the individual station magnitudes of up to approximately 0.54 magnitude units in the horizontal component and approximately 0.29 magnitude units in the vertical component (Sheen et al., 2018). Therefore, we obtained the correction terms for the seismic stations before estimating the M_L (see Text S3 for a detailed description of station corrections). With the station corrections, we estimated the local magnitudes of 40 events based on more than three observations, ranging from 0.15–5.33, with an average standard deviation of 0.14 magnitude units. Note that the M_L of the Pohang earthquake was estimated at 5.33 ± 0.14 from 11 permanent stations within a distance of approximately 50 km from the epicenter. This is similar to 5.34 ± 0.18, which was independently estimated from 77 broadband seismic records from permanent seismic stations in South Korea.

The M_L values of the 72 locatable events near the EGS site were not able to be determined from the synthesized Wood–Anderson displacements as single or double integration into the displacement increased the low-frequency noise or coda waves of the previous events. Instead, they were determined by the peak-amplitudes of the S-wave on the velocigrams and accelerograms of PHA2, which was the only station that had all M_L values. For the events at unknown locations (due to low SNR on the seismograms), the M_L values were determined using the empirical relationships

between the M_L values and peak amplitudes of the S-waves for the 40 events at PHA2. A total of 96 M_L values determined based on the peak amplitudes at PHA2 ranged from –1.30 to 2.03. The uncertainty of the resulting magnitude determinations due to location error and attenuation correction was likely on the order of ± 0.2 magnitude units.

The moment magnitudes of 48 events were determined with a rock density of 2.7 g/cm3 and P-wave velocity of 6.0 km/s in the time and frequency domains. The P-displacement pulse from the accelerometer at PHA2 was used to compute the seismic moment (Aki and Richards, 1980) in the time domain based on the methods reported in Tsuboi et al. (1995) and Prejean and Ellsworth (2001). We measured the moment magnitudes of 46 events in the time domain, which ranged from 0.58 to 2.72. However, it was not possible to compute the seismic moment of the largest two events, i.e., M_L 3.27 on April 15, 2017, and the Pohang earthquake, in the time domain due to the complexity and long duration of the P-pulses. Therefore, the moment magnitudes of these events were estimated in the frequency domain.

The moment magnitude of the M_L 3.27 event was measured with the spectral ratios of the P-wave. We selected the M_L 2.06 (M_W 2.15) event that occurred on April 15, 2017, at 08:16:47 UTC as an empirical green function for the analysis. The average moment ratio from five accelerometers, equipped at the KMA and KIGAM permanent stations, was estimated at approximately 14, which yielded a moment magnitude of 3.29 for the M_L 3.27 event. The moment magnitude of the mainshock was estimated from the P-wave displacement spectra using the methods reported in Rhee and Sheen (2016). We used 20.48 s of the P-waves from 58 broadband seismograms with epicentral distances greater than 150 km. To correct anelastic attenuation along the path, the displacement spectra were scaled with the Q model for P waves reported in Kim et al. (2006). The moment magnitude of the mainshock was determined at 5.56 ± 0.18. Using the Brune (1970), the corner-frequency, stress drop, and source radius of the event were estimated at 0.60 Hz, 56.0 bar, and 3.44 km, respectively. Figure 4.5a shows that

the determined M_{L} values agree with the M_{W} values and estimates from the KMA.

4.3.3 Earthquake-size distribution

Several previous studies on induced seismicity have discussed the frequency– magnitude distribution or the Gutenberg–Richter law (G–R law) as it represents the statistical characteristics of seismic activities in a specific region over a specific time period (Kraft et al., 2016; Zang et al. 2014). This distribution or law can be expressed with the following equation:

$$log_{10}N(\geq \boldsymbol{M}) = \boldsymbol{a} - \boldsymbol{bM} \tag{4.1}$$

where $N(\geq \boldsymbol{M})$ is the number of earthquakes that have a magnitude equal to or greater than $\boldsymbol{M}$ and the $\boldsymbol{a}$- and $\boldsymbol{b}$-values are the seismicity and frequency of large earthquakes compared with smaller earthquakes for a specific region and time, respectively (CF, 1954). We evaluated the $\boldsymbol{a}$- and $\boldsymbol{b}$-values from the estimated magnitude of the earthquakes near the EGS site based on the maximum likelihood method proposed by Aki (1965), with a magnitude bin size of 0.1. Before fitting the observed frequency–size distribution to equation (1), we estimated the minimum magnitude of completeness ($\boldsymbol{M}_{\mathrm{C}}$) that holds equation (1) by maximizing the goodness-of-fit function proposed in Wiemer and Wyss (2000). The standard error of the $\boldsymbol{b}$-value was calculated using an equation proposed by Shi and Bolt (1982).

We investigated the behaviors of the frequency–magnitude distributions for the entire dataset (A1) before the M_{W} 5.5 mainshock. Afterward, two subsets of events in the PX-1 (A2) and PX-2 stimulations periods (A3) were tested separately to compare the statistical parameters of the G–R law. Figure 4.5b shows the frequency–size distribution and fitting lines of equation (1) for the three different groups. The obtained G–R distributions for A1, A2, and A3 had nearly identical $\boldsymbol{b}$-values at 0.66 ± 0.08, 0.61 ± 0.09, and 0.65 ± 0.09, and a-values of 2.08, 1.33, and 1.96, which are proportional to the number of events. The obtained $\boldsymbol{b}$-values were generally lower than commonly observed values in Gyeongsang basin (Hong et al., 2016). The seismogenic indices

($\Sigma = \boldsymbol{a} - logV$; Shapiro et al. (2007, 2010); Shapiro (2018) extracted from the obtained a-values and cumulative injection volumes for A1, A2 and A3 were estimated at –1.69, –1.89, and –1.65, respectively.

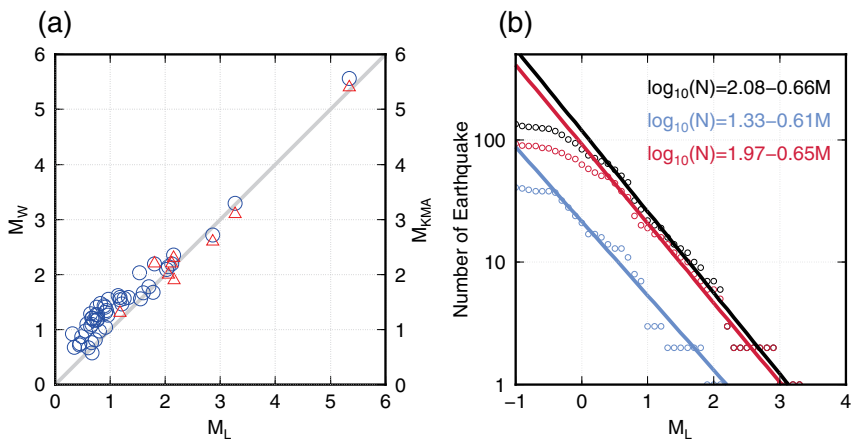

Figure 4.5: (a) Comparisons of the magnitude estimates: local, moment, and KMA magnitudes. The blue circle and red triangle represent the moment and KMA magnitudes corresponding to each local magnitude, respectively. (b) Frequency–Magnitude distribution and best-fitting line for the EGS-related earthquakes before the mainshock. The colors of the symbols and lines represent different earthquake populations: black for all events, blue for events associated with the PX-1 injection, and red for events associated with the PX-2 injection.

4.3.4 Focal mechanism solutions

A distribution of the final locations can help delineate the geometry of the fault plane. However, we must have the focal mechanism solutions to understand the fault type of each event. We constrained the focal mechanism solutions from the P-wave polarities (Lay and Wallace, 1995). We measured the P-wave polarities from the vertical component seismograms. If the polarity was not clear due to low SNR, we determined the polarity using the polarities of the larger events that had similar waveforms. For certain borehole records, we speculate that the vertical sensor may or may not have been deployed correctly. In this case, we analyzed the waveforms of the event that occurred 37 km SW of PX-2, whose focal mechanism was well-constrained by seismograms recorded at local seismographs near the epicenter. We then checked the polarities for suspicious borehole stations by comparing the observed and theoretical P-wave polarities, performing corrections when necessary. To determine the focal mechanism, we applied the HASH (Hardebeck and Shearer, 2002) software with all available records including those at the borehole stations beneath the first layer of our velocity model. We calculated the candidates for focal mechanism solutions by allowing one datapoint error for the polarities to determine the final focal mechanism solution for each event by averaging all possible candidates. The quality of the focal mechanism solutions was evaluated by following the criterion provided in Hardebeck and Shearer (2002). We determined 28 and 25 focal mechanisms with quality A and quality B, respectively. The strike, dip, and rake of the mainshock were determined to be 214º, 51º, and 128º, respectively.

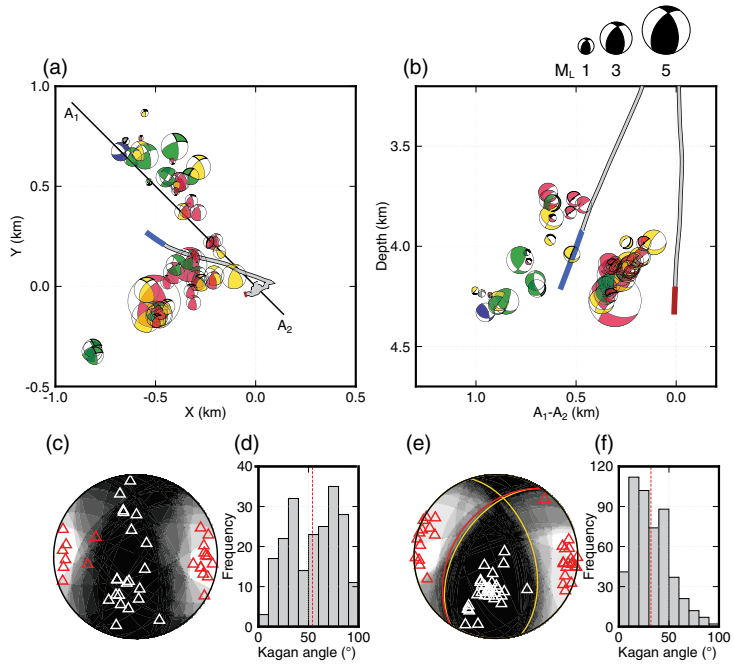

Figure 4.6: (a–b) Distribution of 53 focal mechanism solutions (a) in map view and (b) in a cross-sectional view along A1–A2. Colors of the beachball diagrams represent the fault types determined according to the classification proposed by Zoback (1992): strike-slip (green), thrust (red), strike-slip with thrust component (yellow), strike-slip with normal component (blue), and unclassified faulting type (gray). The origin of the map coordinate is set to the location of the PX-2 well. (c–d) Distribution of the earthquake focal mechanisms in the PX-1 stimulation period and histogram of their Kagan angles. Distributions of P- and T-axes are denoted by red and white triangles, respectively. (e–f) Identical to (c) and (d) but for the PX-2 stimulation period. In (e), the nodal planes of the mainshock are in yellow. The projection of the best fitting plane estimated from the hypocenter distribution is denoted by a red line. Dashed lines in (d) and (f) represent the average value of the Kagan angles (Kagan, 1991).

We classified the fault types of the focal mechanism solutions based on the classification proposed Zoback (1992), identifying 14 strike-slip events, 22 thrust events, and 15 predominantly thrust events with strike-slip components. We did not find any normal faulting events. Only one event had a predominantly normal component with a strike-slip component. These results indicate that the strike-slip and thrust mechanism are dominant in the study area (Figs. 4.6a and 4.6b). The trend and plunge of the average P-axis direction of the 53 events were 96º and 4º, which are consistent with the direction of maximum horizontal stress that occurs under the Korean Peninsula Soh et al. (2018). Previous studies have succinctly shown that the stress field in the region controls the faulting mechanism. Therefore, we inverted the focal mechanism solutions for a stress field in our study area using Michael's method (Michael, 1984; Martínez-Garzón et al., 2014). To avoid the fault-plane ambiguity problem, we adopted the concept of fault instability proposed by Vavryčuk (2014). The results of the stress inversion show that the trend and plunge of the maximum principal stress (σ_1) were 276º and 7º, respectively, which are near the average P-axis direction. In addition, the trends/plunges of σ_2 and σ_3 were determined to 18º/58º and 182º/31º, respectively.

4.3.5 Hierarchical clustering analysis

We applied two different hierarchical clustering analyses (Sibson, 1973; Defays, 1977) to understand the spatial and temporal characteristics of seismicity. The difference between the two methods lies in their definitions of a metric distance between two events. For the first analysis, we used the Kagan angle (Kagan, 1991) as a metric distance between two events for the 53 earthquakes with focal mechanism solutions. The Kagan angle indicates a minimum 3-D rotation angle required for one double-couple earthquake source mechanism and another one. The distance between two clusters is defined as the mean value of the Kagan angle for all possible pairs between the events of each cluster, such that five clusters were classified (i.e., A, B, C, D, and E) based on a criterion of 45º (Figs. 4.7 and A.7). For the second analysis, we used the wave-

form similarity between two events, which is useful when classifying events because additional information, such as the location or focal mechanism solutions, are not required to perform a hierarchical analysis (D'Alessandro et al., 2013; Son et al., 2018). We used the waveforms recorded at PHA2 again as it is the closest permanent station to PX-2. To simultaneously consider the P and S waveforms, we cut the 5-s windows from 0.5 s before the P-wave arrival times. Waveform similarity between two seismograms was estimated as the maximum cross-correlation coefficient (MaxCC), allowing a time shift of up to ± 0.5 s for potential intrinsic picking errors. A band pass filtering between 2 and 20 Hz, as well as a cubic spline interpolation with a sampling rate of 1,000 Hz, were applied before measuring the MaxCC. The metric distance between two events was defined as (1 – MaxCC) while the distance between two clusters was defined as the minimum distance between two events that belong to two different clusters. Exposed to a threshold of 0.25, we identified two clusters (i.e., CW-1 and CW-2) consisting of 24 and 80 earthquakes, respectively (Fig. A.8).

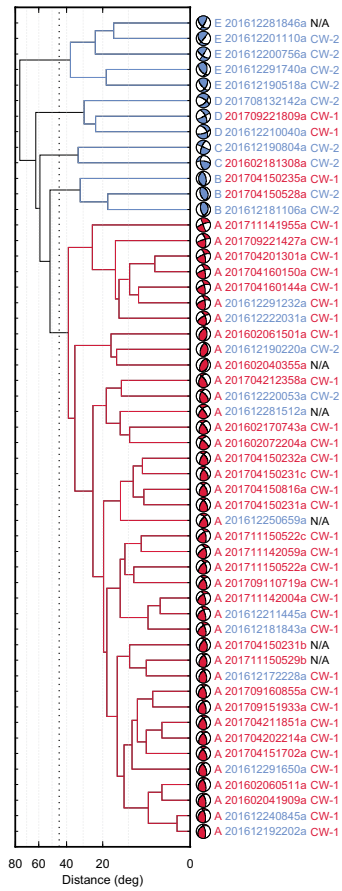

Figure 4.7: A dendrogram of the hierarchically clustered 53 focal mechanism solutions based on the Kagan angle. A threshold of 45° was applied to divide the branches into a large cluster (A) and other clusters (B–E). The focal mechanisms, cluster number, and event IDs corresponding to the leaf nodes are shown on the right side. The colors of the clades, the compressive quadrants of the focal mechanisms, and the mechanism-based cluster separate the largest cluster (red) and the other clusters (blue). The event IDs related to the PX-1 and PX-2 injections are in blue and red, respectively. The results of the clustering analysis based on waveform similarity for the same events are indicated by CW-1 (red) and CW-2 (blue).

4.4 Discussion

4.4.1 Fault reactivation revealed by hypocenter distribution

To investigate the relationship between the hydraulic stimulations into the two wells (i.e., PX-1 and PX-2) and earthquake sequences near the Pohang EGS project site, we divided the 98 relocated events into two groups based on their origin times (Figs. 4.3 and 4.8). The first and second groups (hereafter referred to as G1 and G2) consisted of earthquakes during the PX-1 and PX-2 stimulation periods, respectively. As the M_{W} 0.9 event in the mud loss period, mainshock, and immediate foreshocks were adjacent to the pre-classified G2 events, we additionally included the events in the G2 group.

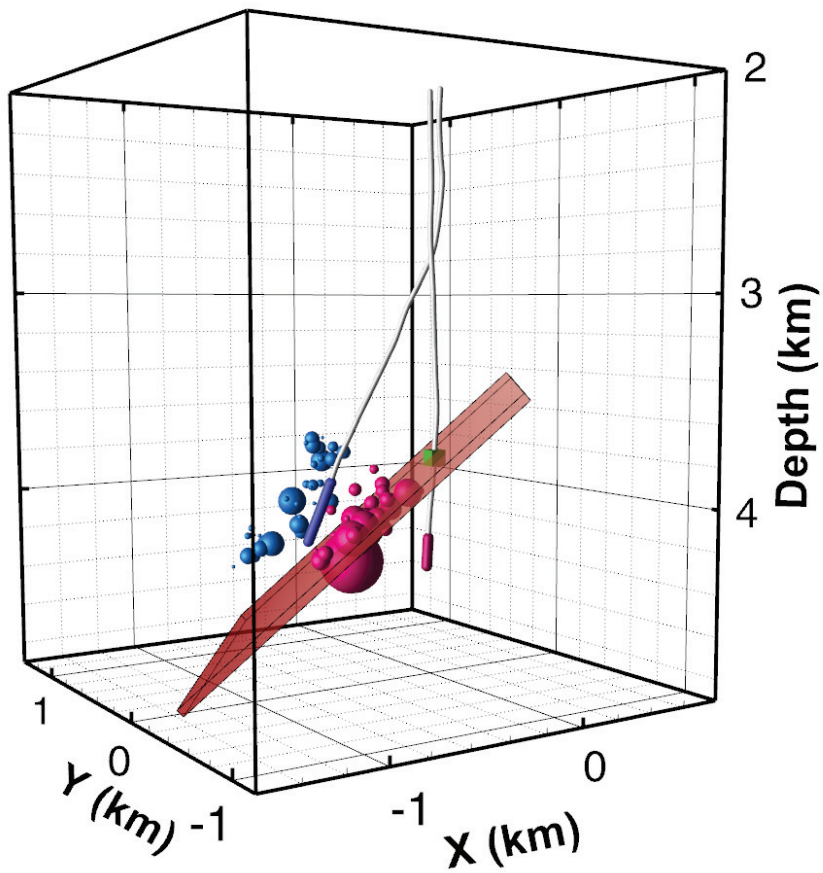

Figure 4.8: A three-dimensional hypocenter distribution of the 98 events with the final location, and the approximate fault plane for the events in the PX-2 stimulation period. The sizes of the symbols are proportional to the local magnitudes of the earthquakes. Gray curves represent the trajectories of PX-1 and PX-2, with two open sections in blue and red. The point at which the best-fitting plane and PX-2 well intersect is denoted by a green cube.

The epicenters of G1 and G2 were clearly separated and distributed along the NW-SE and NE-SW trends, respectively, except for the M_W 2.0 event on September 11, 2017, that occurred in the last stimulation at PX-2 (Figs. 4.4a and A.6). Considering that the experiment was conducted only one month prior to the fourth stimulation at PX-1, and that the event was located in the G1 area, we suggest that this event was a delayed seismic response to the fourth stimulation. The hypocenter distribution of G1 and G2 in Figure 4.4 reveals that G1 events formed a tube-like structure with deepening focal depths in a NW direction, whereas those for G2 appear to have occurred on a fault dipping in a NW direction. We evaluated the similarity of the spatial distribution's shape for G1 or G2 to a planar structure using planarity: $(1 - L_3/L_2)$, where L_2 and L_3 are the immediate and minimum eigenvalues of the covariance matrix for a collocation of x, y, and z, respectively, i.e., $Var([x\ y\ z])$. The results show that the planarity values of the distribution are non-negative and can be as high as 1. Here, one corresponds to a perfect planar structure. The planarities of G1 and G2, with the exclusion of the M_W 2.0 event at G2, were 0.44 and 0.71, respectively, which suggests that the G2 events were closer to a planar structure than those of G1. Using a conventional principal component analysis, we obtained the strike and dip of the approximate fault plane for G2 as N214º and 43ºNW, respectively, which are similar to the focal mechanism of the M_W 5.5 mainshock (i.e., N214º/51ºNW; see Figure 4.6e), the fault plane estimated from the aftershock distribution (Kim et al., 2018c), and the focal mechanism obtained by a moment-tensor inversion (Grigoli et al., 2018). As the G2 fault plane shares the same strike and dip of the Pohang earthquake, as well as the immediate foreshocks, the mainshock appears to have initiated on a pre-existing fault plane, with the occurrence of earthquakes induced by fluid injections in PX-2.

Topographical variations perpendicular to the epicenter distribution of G2 have been observed. The overall altitude of the western region is lower than that of the eastern region (Fig. 4.4a). Unconsolidated alluvial sediments are prevalent on the western side of G2 while the sedimentary layer of sandstone and mudstone are mapped on the

eastern side (Song, 2015). Therefore, the fault, delineated by the spatial distribution of G2, may represent the reactivation of a pre-existing normal fault in the basin structure that developed in an extensional tectonic setting. Including the Gokgang fault, NE striking normal faults that dip in the SE/NW direction can be found throughout the Pohang basin, such that stress inversion from extension to compression resulted in the reactivation of the normal faults (Yoon et al., 2014).

4.4.2 Breakage at the crossing point of the fault and PX-2

When the best-fitting fault plane, which was obtained from the spatial distribution of G2, was extended toward the PX-2 well, it crossed the well at a depth of approximately 3,800 m (Fig. 4.8). This depth nearly coincides with a depth of 3,783 m, which has been inferred as the breakage of the borehole. The image logging test was performed nine months after the M_{W} 5.5 mainshock but an image logging device was unable to descend any further (Lee et al., 2019a). Therefore, it is reasonable to infer that the G2 events, including the mainshock, occurred on the same fault plane with similar focal mechanisms and rupture propagation of the mainshock broke the casing of the PX-2 well.

Nearly two months before the first stimulation of PX-2, 652 m^3 of heavy mud (1.6 gcm^{-3}) was lost during the well drilling process (Lee et al., 2019a). Most of the loss occurred at a depth range of 3.8–4.0 km, which matches with the crossing point between the best-fitting fault plane for G2 and PX-2 well trajectory. The largest event (M_{W} 0.9) in the pre-stimulation period was also on the approximate fault plane. Therefore, it is plausible to assume that the mud was lost along the fault fracture zone, perturbing the stress field due to the inflow of mud into the hydraulic medium and generating microearthquakes on the fault in the pre-stimulation period. Induced seismicity during injection well drilling has also been reported in the Schlattingen geothermal project (Kraft et al., 2016) and Hellisheiði Power Plant (Ágústsson et al., 2015). Reactivation of the fault plane for G2 can be attributed to the mud loss during drilling,

along with the three stimulations in PX-2.

4.4.3 Seismic responses of the PX-1 hydraulic experiment

Based on the spatial distribution and diversity of the focal mechanisms, the G1 events are considered to have occurred on optimally oriented faults as a response to the local stress field unlike the seismicity of G2 with similar fault types (Figs 4.6c–f and 4.7). Therefore, in contrast to the seismicity of PX-2, which delineates a pre-existing fault plane that deviates from PX-2 (e.g., Yeck et al. (2016); Schultz et al. (2017); Lei et al. (2017)), the earthquakes related to the PX-1 hydraulic stimulations should be clustered near the open section of PX-1 as a response to the elevated pore pressure in the proximity of the PX-1 injection interval, possibly due to pore pressure diffusion (Ogwari and Horton, 2016) or poro-elastic responses as suggested by (Cornet, 2016). However, the overall hypocenters of G1 deviate from PX-1 to the NE by approximately 200 m (Fig. 4.4a).

As the final locations were determined by shifting the relocated events to the absolute location of the key event, the accuracy of the final hypocenters was entirely dependent on the estimated absolute location of the key event. To locate the key event, we used the particle-motions-recorded PX-2 borehole chain, where the seismometers are arranged nearly vertically along PX-2. High-resolution phase arrivals measured from 1,000 Hz seismograms with high SNR resolved the focal depth of the event with an uncertainty of 0.1 km. These estimates were cross-validated by two independent estimations from differential PS times at the two farthest sensors and from tube waves generated in the encased wellbores (see Text S2 of the electronic supplement to this article). The azimuth of the key event was also accurately measured from the stacked waveforms of seismograms with high coherency. However, the absolute orientations of the wellbore sensors estimated by the teleseismic events may have intrinsic uncertainties due to the lateral fractions of ray paths (Laske, 1995). Inaccurate estimation of the station orientation can result in horizontal uncertainties for the determined hypocenters

regardless of the accuracy of the estimated azimuth for the key event.

Assuming that the perturbed pore pressure at the open section of PX-1 governed the seismicity in G1, as well as that the optimally oriented fractures ruptured in response to the current tectonic stress, earthquakes that were expected during the stimulations at PX-1 were clustered at the open section of PX-1. If we assume that the orientation error of the borehole sensor is 20° and rotate the absolute location of the key event anticlockwise by 20°, the events in G1 may be shifted to near the open hole interval of PX-1. The shifted final hypocenters do not affect the main observed features discussed above. The best fitting fault plane for G2 still crosses the PX-2 well at a slightly shallower depth of approximately 3.77 km. The crossing point and the projection of the PX-2 open section onto the best-fitting fault plane of G2 are displaced to the NE, such that the migration pattern clearly appears to have initiated near the projection of the open hole interval at PX-2.

4.4.4 Spatiotemporal variations in seismicity for stimulation periods

We investigated the detailed spatial and temporal distribution of earthquakes that occurred during or after five stimulations at PX-1 and PX-2 by subdividing G1 and G2 into seven subgroups based on the stimulation periods. G1 was divided into G1-1 and G1-2 for the second and fourth stimulations performed at PX-1, respectively, while G2 was divided into G2-1, G2-2, and G2-3 for the first, third, and fifth stimulations at PX-2, respectively (Fig. 4.4). The pre-stimulation earthquakes that occurred due to heavy mud loss in PX-2 and the M_{W} 5.5 mainshock sequences were set to G2-0 and G2-M, respectively.

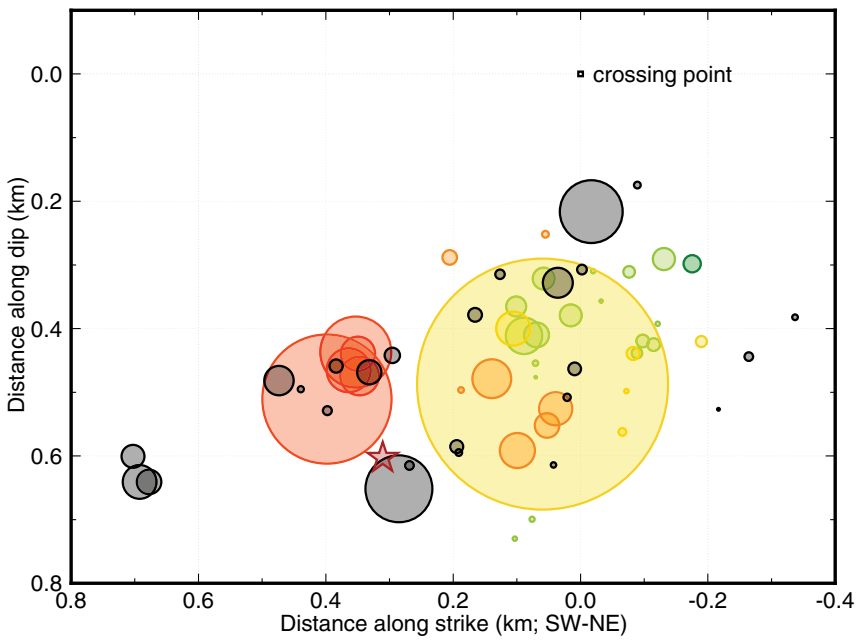

Figure 4.9: Locations of G2 events projected onto the best-fitting fault plane of 214°/43°. Colors represent the occurrence period of the earthquakes: G2-0 (dark green), G2-1 (green), G2-2 (yellow), G2-3 (orange), and G2-M (red). In G2-2, the aftershocks of the M_W 3.2 earthquakes are denoted by gray circles. The origin of the coordinate is set to the intersection (open square) of the PX-2 borehole and fitting plane. The hypocenter of the M_W 5.5 mainshock is denoted by a star symbol. The ruptured area of each earthquake is illustrated by circles based on the assumption of circular cracks reported in Madariaga and Ruiz (2016) for a stress drop of 5.6 MPa, obtained from the spectral ratio method. This value is comparable with the estimation on the periphery of the mainshock hypocenter (Song and Lee, 2019).

We observed no spatial variation between G1-1 and G1-2 despite a lack of seismicity at G1-2. Compared with the hypocenter distribution demonstrated in Hofmann et al. (2019), who analyzed 52 events in the fourth stimulation (including the key event) using the PX-2 borehole geophone array, the relative locations of the 52 events to the key event also overlapped with our results for G1-1. In contrast, G-2 seismicity appears to have sequentially migrated SW as the stimulation experiments were iterated at PX-2 (Fig. 4.9). Moreover, the only relocated event of M_{W} 0.9 in the pre-stimulation period (G2-0) is situated on the NE edge of the events in G2-1. Compared with the events in G2-1, the events of G2-2 slightly expanded to the SW by 100 m and in the down-dip direction by 200 m. One day after the end of the third stimulation, the M_{W} 3.2 event occurred at the SW periphery in the G2-2 seismicity. Its aftershocks, which are thought to have been triggered by stress transfer or post-seismic stress relaxation, are distributed over a wider range of approximately 1 km to both the SW and NE. Barring the aftershocks of the M_{W} 3.2 event, the G2-3 events apparently migrated SW and in down-dip directions by approximately 100 m compared with the G2-2 events. Immediate foreshocks and the mainshock, which occurred two months after the end of the last stimulation at PX-2, are located 200 m to the SW compared with the events in G2-3.

Although a matched-template approach was used to maintain a constant detection power, the observed seismic activity with respect to the injection rates or wellhead pressure varied for each stimulation period (Figs. A.2–A.6). For PX-1, the first detected event of M_{L} –0.3 at the second stimulation occurred approximately 3 d after the onset of its operation, whereas, for the fourth stimulation, it took more than twice as long, i.e., approximately 7 d (Figs A.3 and A.5). In addition, the number of events in G1-1 outnumbered that in G1-2 by over an order of magnitude. The seismic quiescence at the beginning of the later stimulation may represent the Kaiser effect, which indicates a lack of seismicity until the current stress level exceeds the previous loading Baisch et al. (2006); Hofmann et al. (2019); Kwiatek et al. (2019). In the second stim-

ulation, 3,907 m3 of water was injected with a maximum wellhead pressure of 27.7 MPa Hofmann et al. (2019). In contrast, the fourth stimulation applied a cyclic soft stimulation, which allows alternating phases in the flow rate to control the wellhead pressure and maximum event magnitude, such that 1,756 m3 of water was injected with a maximum wellhead pressure of 25.2 MPa without allowing any shut-in period Hofmann et al. (2019). A large amount of bleed-off in the fourth stimulation resulted in a decreased net injection volume for PX-1. Therefore, scarce seismicity in the fourth stimulation may have resulted from the low injection rate, smaller injection volume, and the use of a controlled stimulation procedure (Figs. 4.3 and A.5).

In the three stimulations at PX-2, differences were also observed in the time delay between the first observed event and onset of each stimulation. The first detected M_{L} 0.0 event in the first stimulation occurred three days after the onset of injection, whereas there was a two-week gap between the seismic activity and onset of periodic injection in the third and fifth stimulations. As the injected fluid perturbs local stress fields across a large area over time due to pore pressure diffusion and the poro-elastic effect (e.g., Goebel et al. (2017)), the time delay in seismicity initiation for the two later stimulations may account for the expansion of the area with seismic activities on the best-fitting fault plane of PX-2. The lack of seismicity at the previously activated region may indicate that the loaded stress on the area was far less than the critical stress due to stress release through previous seismic activity. The observed unilateral migration pattern, which has also been observed for the large-scale waste water disposal operation in Oklahoma and southern Kansas (Schoenball and Ellsworth, 2017), hydraulic fracking in Canada (Woo et al., 2017), and at the Yamagata-Fukushima border (Yoshida and Hasegawa, 2018), may have resulted from heterogeneities in the hydraulic parameters, frictional properties, and stress state on the PX-2 fault. Further migration of G2-M to the SW also matches with a two-month gap of seismicity from the onset of the last stimulation. This phenomenon shows that redistribution of the stress field over large areas takes time.

All earthquakes with $M_L > 1$ occurred during periods characterized by bleed-off or shut-in rather than fluid injection. While the maximum magnitude of the earthquakes that occurred during fluid injection was only 0.905, seven events with $M_L > 2$ (one event in G1-1, three events in G2-2, and three events in G2-M) occurred immediately after each stimulation period or in the foreshock sequences. This is not an unusual occurrence as large-magnitude earthquakes have often been observed in other EGS sites such as Cooper Basin, Soultz, and Basel during shut-in periods or after bleeding-off (Häring et al., 2008; Majer et al., 2007; Mukuhira et al., 2017).

4.4.5 Deviation between physics-derived scaling equations for maximum seismic moment and net injection volume for the M_W 5.5 mainshock

Based on the derived equation reported in McGarr (2014) for the relationship between the maximum seismic moment (M_{max}) and volume (V) of the injected fluid, inducing the M_W 5.5 Pohang earthquake required at least a 500-fold greater fluid injection volume. Despite the inconsistency between the observed and expected maximum seismic moments, the M_W 5.5 event is suspected to have had an anthropogenic origin due to its spatiotemporal correlation with the injection workflow (Kim et al., 2018c; Grigoli et al., 2018). To closely analyze the relationship between M_{max} and V at the Pohang EGS site, we compared the seismic moment of the Pohang earthquake and largest prior events with the net injected volumes at their origin times for PX-1, PX-2, and both wells (Fig. 4.10). We observed two main characteristics in the correlation between the two parameters. First, most of the detected earthquakes had moment magnitudes less than the expected M_{max} when using the V, except for the M_W 5.5 mainshock. Based on the three scaling equations in Figure 4.10, the M_W 3.2 event, which was the largest event before the occurrence of the M_W 5.5 event, was already near the upper limit of the maximum magnitude responsible for the net inflow at the moment. Based on Galis et al. (2017), the M_W 5.5 event can be classified as a run-

away rupture or self-sustained rupture, where the majority of the seismic energy was tectonically released along critically stressed faults regardless of the initial rupture process. This is consistent with the modeled stress state and static friction of the fracture obtained from focal mechanism inversions, drilled boreholes, and measured wellhead pressures, which all indicate that the G2 best fitting plane may have been (nearly) critically stressed Ellsworth et al. (2019); Lee et al. (2019a). Second, the size of the $\boldsymbol{M_{max}}$ steeply increased over time, far beyond the expected $\boldsymbol{M_{max}}$ value (Fig. 4.10). This is contrary to the temporal evolution of $\boldsymbol{M_{max}}$ and V observed in a geothermal stimulation in Finland (Kwiatek et al., 2019), which followed several scaling models (see Fig. 5 in Kwiatek et al. (2019)). Van der Elst et al. (2016) revisited the equation proposed by McGarr (2014) using statistical approaches, finding that the seismic moment scales up with $V^{3/(2\boldsymbol{b})}$ rather than V alone. The derived equation from Van der Elst et al. (2016) can partially explain the dramatic change in $\boldsymbol{M_{max}}$ that increased due to V when our estimated $\boldsymbol{b}$-value of 0.66 was used instead of the commonly assumed $\boldsymbol{b}$-value of 1. However, the seismic moment of the Pohang earthquake was still larger than the expected $\boldsymbol{M_{max}}$ by over two orders of magnitude.

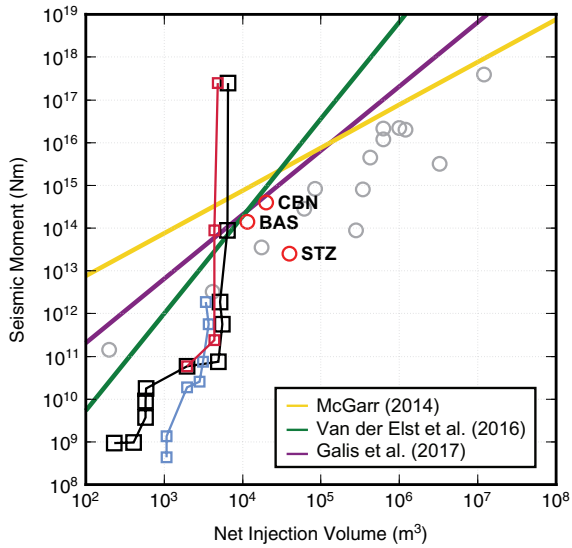

Figure 4.10: Temporal evolution of the correlations between the maximum moment magnitude and net injection volume. Blue, red, and black lines represent the correlations for PX-1, PX-2, and both PX-1 and PX-2. For the comparison, data from a global dataset used in McGarr (2014) are incorporated and denoted by open circles while we overlapped three different equations that scaled the two parameters. Data from three EGS sites are highlighted by red circles: CBN for Cooper Basin, Australia, BAS for Basel, Switzerland, and STZ for Soultz, France. The seismogenic index (Σ; Shapiro et al. (2007, 2010); Shapiro (2018)) and $\boldsymbol{b}$-value for the equations from McGarr (2014) and Van der Elst et al. (2016) were set to –1.7 and 0.66, respectively, based on the frequency–magnitude relationship shown in Fig. 4.5b. The γ value in the equation from Galis et al. (2017) was estimated as 2.1×10^8 by assuming a set of plausible values: (1) a stress drop of 3 MPa following Fig. 4.9, (2) a bulk modulus of 50 GPa from the 1-D velocity model, (3) a dynamic frictional coefficient of 0.5, which is slightly smaller than the average static frictional coefficient of 0.6 (e.g., Townend and Zoback (2000)), and (4) a reservoir thickness of 0.28 km estimated from the plane normal distribution of the G2 hypocenters, as well as the interval between 3,788 and 4,068 m where a large volume of mud was lost. Note that the occurrence of the M_W 5.5 mainshock significantly deviates from the global log-log linear trend.

The hydraulic energy supplied by fluid injection into the two stimulation wells is inconsistent with the observed seismic moments. We calculated the hydraulic energy of the injected fluid using $\boldsymbol{E_h} = \int P(t)Q(t)dt$, where $P(t)$ and $Q(t)$ are the wellhead pressure and injection flow rate, respectively. The seismic energy ($\boldsymbol{E_S} = \Delta\sigma \boldsymbol{M_0}/2\mu$; Lay and Wallace (1995)) released by the $\boldsymbol{M}_{\mathrm{W}}$ 5.5 event corresponds to 3.7 × 10^{13} J based on a stress drop ($\Delta\sigma$) of 5.6 MPa and shear modulus of 30 GPa (μ), which is approximately 50 times larger than the cumulative hydraulic energy of 6.9 × 10^{11} J. In contrast, the total seismic released energy from the mud loss period to the onset of the $\boldsymbol{M}_{\mathrm{W}}$ 3.2 event was 1.2×10^{10} J, corresponding to 4% of the hydraulic energy of 4.8 × 10^{11} J. De Barros et al. (2019) argued that the hydraulic energy is typically significantly larger than the seismic energy due to a large aseismic deformation related to the fluid injection. Therefore, the energy equilibrium for the $\boldsymbol{M}_{\mathrm{W}}$ 5.5 mainshock and possible large aseismic deformations (Guglielmi et al., 2015; Cornet, 2016) require other types of input energy besides the hydraulic energy, such that it is consistent with the large discrepancy between the observed and expected maximum moment magnitudes.

4.5 Conclusion

In this study, we were able to prove that there is a clear causal link between the origin of the 2017 $\boldsymbol{M}_{\mathrm{W}}$ 5.5 Pohang earthquake and injected fluids injected as part of an enhanced geothermal system (EGS) project through spatiotemporal relations. For this, we constructed a local 1-D velocity structure and analyzed the characteristics of the earthquakes that occurred in the vicinity of the EGS site until the occurrence of the Pohang earthquake. We did not detect any earthquakes within 5 km of PX-2 based on our matched filter analysis until an $\boldsymbol{M}_{\mathrm{L}}$ –0.1 event that occurred on November 1, 2015, when a large volume of heavy mud was lost from PX-2. The relocated seismicity indicates that the earthquakes during the PX-1 stimulation periods represented an ellipsoidal distribution to the NW-SE, whereas seismicity during the PX-2 stimulations

had the shape of an NE-SW fault plane dipping to the SE. Except for the aftershocks associated with the second largest M_{W} 3.2 event, earthquakes on the fault plane appear to have migrated to the SW during an inter-stimulation period. A series of hierarchical clustering analyses suggested that they share similar fault parameters. The intersection depth between the fault plane and PX-2 was approximately 3,800 m, which corresponds to the intervals of heavy mud loss, as well as the breakage of the borehole inferred by an image-logging device. However, unlike the earthquakes in the stimulation periods, the seismic moment of the Pohang earthquake far exceeded the possible ranges estimated by both the $M_{max} - V$ scaling laws and energy equilibrium. These results provide strong evidence that the M_{W} 5.5 Pohang earthquake initiated on the fault zone that was reactivated by fluid injection, representing a self-sustained rupture process that released a large amount of energy via tectonic loading rather than being a directly induced earthquake via fluid injection. The Pohang earthquake case provides the lesson that large earthquakes on well-developed and critically stressed faults can be triggered even if fluid injection does not apply significant stress perturbations. We must carefully observe such potentially hazardous faults in advance to reduce the risk of damaging earthquakes.

Chapter 5

Aftershock sequences and statistics of the 2017 M_{W} 5.5 Pohang earthquake, South Korea: fault heterogeneity and possible post-seismic relaxation

5.1 Introduction

On 15 November 2017, a moderate-sized earthquake of moment magnitude (M_W) 5.5 or local magnitude (M_L) 5.4 struck the city of Pohang, located in the southeastern part of the Korean Peninsula, which damaged infrastructure, injured 90 people, and made 1,500 homeless (Kim et al., 2018c,a; Grigoli et al., 2018; Hong et al., 2018). The earthquake (hereafter referred to as the mainshock) was the second-largest earthquake event among earthquakes recorded instrumentally in South Korea since 1978, according to the catalog of the Korea Meteorological Administration (KMA). A close examination of the seismic source characteristics of such a rarely observed moderate-sized earthquake and its foreshock-mainshock-aftershock sequence is necessary not only to evaluate the current stress field (Zoback, 1992; Soh et al., 2018) and fault properties, but also to understand aftershock triggering mechanisms (King et al., 1994; Kilb et al., 2000). Estimation of statistical parameters (i.e., the Gutenberg-Richter b-value and the Omori law p-value) from a large number of microearthquakes in conjunction with the seismic source properties of aftershocks can give information on fault heterogeneities, such as crack density, slip distribution, applied shear stress, viscoelastic properties, and heat flow (Wiemer and Katsumata, 1999; Murru et al., 2007). One important point to note is that the mainshock occurred near an enhanced geothermal system (EGS) site (Grigoli et al., 2018; Kim et al., 2018c; Lee et al., 2019b). A body of evidence supports the claim that the mainshock was triggered by five fluid-injection experiments as well as an associated loss of heavy drilling muds and released tectonic energy on a critically stressed fault (Ellsworth et al., 2019; Woo et al., 2019a). The periods of stimulation experiments conducted on two hydraulic wells (PX-1 and PX-2) were closely correlated with microseismicity observed near the wells. Induced seismicity mapped in the vicinity of the EGS indicated the presence of a previously unmapped fault. Microseismicity triggered on this fault migrated to the location of the mainshock. A breakout was observed in the PX-2 well at intervals corresponding to the assumed fault. The groundwater levels of PX-1 and PX-2 decreased abruptly by 121 m and 793 m, re-

spectively, immediately after the mainshock but gradually recovered by 0.076 m/day and 0.1986 m/day, respectively (Lee et al., 2019a). Previous studies of aftershock distributions in the Pohang Basin determined the presence of complex fault geometries (Hong et al., 2018; Kim et al., 2019). Separately, Grigoli et al. (2018) reported that obtaining a significant non-double-couple (non-DC) component when inverting the moment tensor for a mainshock can be attributed to the complexity of the rupture process in a multi-fault system. The spatial pattern of early aftershocks associated with two 2016 Gyeongju earthquakes (M_{L} 5.1 and M_{L} 5.8), which occurred on two subparallel faults approximately 40 km away from the Pohang mainshock, is differentiated from the presence of two or three fault segments with varying strikes and dips for the early aftershocks associated with the 2017 Pohang earthquakes (Uchide and Song, 2018; Son et al., 2018; Woo et al., 2019b). In this study, we created an earthquake catalog for the foreshock-mainshock-aftershock sequence from data recorded by local permanent seismic networks, temporary seismometers deployed as part of the aftershock monitoring system, and the temporary Pohang EGS monitoring system. Earthquakes were detected using a machine-learning data mining technique for data obtained during the first ten days and a conventional automatic detection algorithm was employed for the aftershock monitoring system as a whole. Each detected earthquake was located by manual picking and visual inspection and then precisely relocated by the double-difference method (Waldhauser and Ellsworth, 2000). Using the spatial distribution of over 4000 earthquakes, we modeled fault systems as a series of multiple fault segments by mapping the spatio-temporal distribution of the statistical parameters $\boldsymbol{b}$ and $\boldsymbol{p}$. Mapping the distribution of earthquake magnitudes provides an independent analysis of the characteristics of aftershock activities and can be used to analyze spatial heterogeneities of material properties, such as stress state, level of asperities, and heat flow rate (Scholz, 1968; Wiemer and Katsumata, 1999; Wiemer and Wyss, 2000; Ávila-Barrientos et al., 2015); assess seismic hazards via epidemic-type aftershock sequence modeling (ETAS; Ogata (1998)); and conduct probabilistic

seismic hazard analysis (PSHA; Cornell (1968)). In this study, we evaluated the relative magnitude of each earthquake by using amplitude ratios relative to earthquakes of known M_{L}.

5.2 Data and method

5.2.1 Seismic networks

Continuous seismic waveform data used to detect and analyze seismic source parameters were collected from four different networks (Fig. 5.1). The first data set was obtained from a combined permanent seismic network operated by KMA, the Korea Institute of Geoscience and Mineral Resources (KIGAM) and the Korea Hydro and Nuclear Power (KHNP). The permanent seismic networks of KMA, KIGAM, and KHNP are named KS, KG, and KN, respectively. The second set of continuous waveform data were recorded by nine borehole seismometers installed at depths of between 100 and 150 m, which operated to monitor microseismic events for the Pohang EGS project. Three of the temporary borehole seismometers recorded the mainshock, while the operation of the other borehole seismometers started within the next 2 days; all of them operated until the end of November 2017. The third continuous waveform data set was collected by 37 broad-band seismometers installed after the mainshock by KIGAM, Pukyong National University, and Seoul National University. The first seismometer installed temporarily for monitoring aftershocks started its operation approximately 1 h after the onset of the mainshock. Lastly, we used waveforms of 214 early aftershocks, occurred within four hours from the mainshock, recorded at eight short-period temporary seismometers deployed by Pusan National University (Kim et al., 2018c). The temporary seismometers operated by Pusan National University, the other two universities, and KIGAM were densely spaced and located within 10 km, 5 km, and 20 km from the EGS site, respectively (Fig. 5.1).

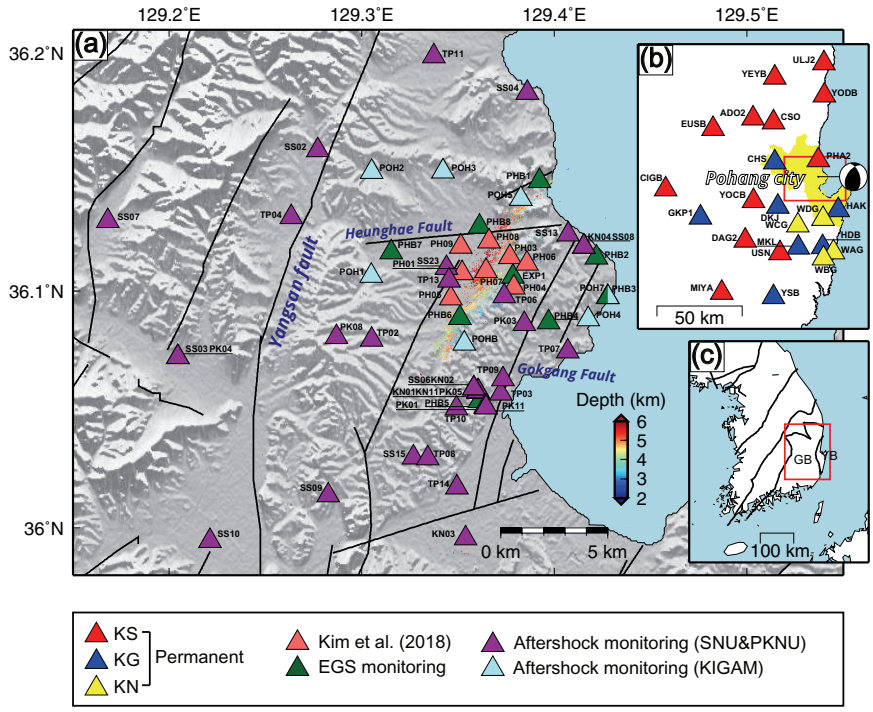

Figure 5.1: Map of (a) temporary and (b) permanent seismic stations used for analysis of source parameters, geologic lineaments, faults, and relocated hypocenters. Three surface ruptures near the study area are illustrated in (a). The focal mechanism of the mainshock that was determined from the polarity of first arrivals is illustrated in (b). (c) shows the location of the Gyeongsang Basin (GB) and the Yeonil Basin (YB) where many NE-NNE sinistral strike-slip surface ruptures and NW transfer faults have developed. The red boxes in (b) and (c) represent the domain of (a) and (b), respectively.

5.2.2 Detection and hypocenter determination

Since stabilizing temporary seismometers for aftershock monitoring can take many hours, conventional algorithms for earthquake detection, such as STA/LTA (Withers et al., 1998; Trnkoczy, 1999), are of limited use for locating early aftershocks because of the incompleteness of the local seismometer network. In this study, we utilized the Fingerprint and Similarity Threshold (FAST) data-mining algorithm that uses waveform similarity to detect such early aftershock sequences (Yoon et al., 2015, 2017; Bergen and Beroza, 2018) with a conventional energy-based algorithm for the period for aftershock monitoring system. The FAST algorithm finds pairs of waveforms having similar spectrograms without any prior information, allowing us to obtain pairs of earthquake candidates with correlative signals. The performance of the FAST algorithm to discriminate true events from earthquake candidates can be improved by measuring similarity at multiple stations (Bergen and Beroza, 2018). We applied the FAST method to ten days of continuous seismograms recorded between 14 Nov 2017 and 23 Nov 2017 to cover the period of operation of the aftershock monitoring system. We used three-component seismograms obtained from two short-period (PHA2 and DKJ) and one broadband (CHS) seismometers, which are located less than 30 km from the mainshock. The three borehole seismometers of the EGS monitoring system that were operational at the onset of the mainshock were not used in this study due to the high level of ambient background noise. The sampling rate of the seismograms was fixed at 100 Hz and the frequency range of the bandpass filter was set to 2–20 Hz. All parameters employed in the FAST algorithm routines were either determined manually from performance trials and or were previously applied values (Yoon et al., 2017, 2019a) and are summarized in Table S1. We detected 1,580 candidate events via the FAST search, leading to a subset of 1,357 locatable earthquakes from visual inspection. This is comparable to the number of events in the earthquake catalog published by Kim et al. (2018), which utilized eight local seismographs deployed within 3 km of the EGS site for earthquake detection: the FAST algorithm successfully detected

169/174 or 97% of earthquakes for the same period. While the aftershock monitoring network was operational (i.e., from 11 November 2017 to 28 February 2018), we applied an automatic algorithm to detect and locate microseismic earthquakes (Sabbione and Velis, 2013). Continuous waveforms were transformed into characteristic functions for measuring the ratio between the short-term average (STA) and the long-term average (LTA). We declared candidate earthquakes when the STA/LTA ratio exceeded 5 for a given time window of 4 s at more than three stations. For each triggered time window, the normalized squared envelope functions of (Baer and Kradolfer, 1987) were calculated to determine the time at which to maximize the function value (hereafter referred to as the BK function). Since the BK function can be maximized for the arrivals of either the P-wave or the S-wave, the maximum value of the BK function was tested to discriminate whether the measured local maximum corresponded to the first arrival. If we observed a local high BK function value before the maximum of the BK function in a given time window, we set two consecutive time samples as the arrivals of the P- and S-waves. Otherwise, we searched for other local maximum after the triggered time window and set the maxima as the P- and S-wave phase arrivals when a secondary maximum was available. The phase arrivals determined in this way were visually confirmed by using a Wadati plot (Wadati and Oki, 1933). We determined the initial hypocenters of the detected earthquakes via Hypoellipse (Lahr, 1999), with phase arrival times being determined by manual inspection and a 1-D layered seismic velocity model for the Pohang EGS site (Woo et al. (2019a); Table 1). In this procedure, we combined the earthquakes detected from either the FAST algorithm or the STA/LTA method with events with $M_{\mathrm{L}} > 2.0$ listed in the KMA and (Kim et al., 2018c) event catalogs. Earthquakes with an onset difference of less than 2 s were regarded as duplicate events. Station corrections were calculated based on a comparison of the hypocentral parameters for five immediate foreshocks reported by (Woo et al., 2019a) and their theoretical arrival times using the assumed seismic velocity model (Table 1).

Table 5.1: The 1-D layered seismic velocity structure for the Pohang EGS site.

Depth to the top of the layer (km)	P-wave velocity (kms^{-1})	S-wave velocity (kms^{-1})
0.0	1.67	0.48
0.203	4.01	2.21
0.67	5.08	3.03
2.4	5.45	3.07
3.4	5.85	3.31
7.7	5.91	3.51
12	6.44	3.70
34	8.05	4.60

Initial hypocenters were relocated with hypoDD (Waldhauser and Ellsworth, 2000) by using travel time differences obtained from waveform cross-correlation measurements as well as picked phase times as inputs to the double-difference algorithm. All relocated events were shifted by 39 m, 28 m, and 96 m in eastwards, northwards, and downwards, respectively, to match the centroid of the five immediate foreshocks with the results of (Woo et al., 2019a), of which recordings at 17 PX-2 borehole chains were applied to obtain accurate hypocenters. The 1-D velocity model of (Woo et al., 2019a) was applied for the relocation procedure. We resampled waveforms to 1000 Hz with a cubic spline after first having applied a 2–10 Hz bandpass filter. Each seismogram was reduced to a 1 s time window centered at each phase arrival time. We allow a time shift up to 0.1 s for the cross-correlation measurements. Time shifts that maximized the cross-correlation coefficient (CC) between two pairs of waveforms were used only if the maximum CCs were greater than 0.85. The squared maximum CCs were used to weight the measurements. The relative locations were calculated by least-squares fitting of the data and the location uncertainties were evaluated by using bootstrapping analysis (Waldhauser and Ellsworth, 2000). Synthetic travel time differences between

paired events were reconstructed by random selection of a set of residuals and relative locations for these synthetic travel times were calculated 200 times.

5.2.3 Detection and hypocenter determination

Waveform similarity can be assessed to estimate the relative magnitudes of earthquakes (Shelly et al., 2016; Yoon et al., 2019b). We adopted a simple magnitude-amplitude relationship modified from the equation of (Shelly et al., 2016) that considers the differences in hypocentral distance between two earthquakes:

$$d\boldsymbol{M} = clog_{10}(a/r) \tag{5.1}$$

where $d\boldsymbol{M}$, a, and r represent the ratios of magnitude, amplitude, and hypocenteral distance, and c is a coefficient for the magnitude-amplitude relationship (Shelly et al., 2016). The coefficient c in Equation 1 varies with the earthquake magnitude scale that is used: for example, Shelly et al. (2016) reported that $c = 1$ for $\boldsymbol{M}_{\mathrm{L}}$ and $c = 2/3$ for $\boldsymbol{M}_{\mathrm{W}}$. In this study, we used a set of $\boldsymbol{M}_{\mathrm{L}}$s of aftershocks and Equation (1) to estimate the coefficient c, following the method of Woo et al. (2019b). If the CC of a waveform pair was greater than 0.85, we calculated the amplitude ratio as the slope of the eigenvector for the largest eigenvalue of the covariance matrix of the two waveforms (Shelly et al., 2016). Thus, for earthquakes with known values of $\boldsymbol{M}_{\mathrm{L}}$, we were able to estimate the parameter c. We can also determine relative magnitudes of earthquakes by using our estimated value of c in Equation (1). Estimated relative magnitudes ($\boldsymbol{M}_{\mathrm{Rel}}$) were arithmetically averaged to produce a representative value and uncertainties were obtained from their standard deviations. The Gutenberg-Richter law (G-R law) describes the relationship between earthquake frequency and magnitude. Its statistical properties are widely accepted and applied to the investigation of seismo-tectonic properties in a specific region over a certain time period. Examples of application of the G-R law include work on aftershock sequences by (Wiemer and Katsumata, 1999; Woo et al., 2019b), on earthquake swarms by (Farrell et al., 2009), on induced seismicity

by (Shapiro et al., 2007), and in laboratory experiments by (Scholz, 1968). The earthquake frequency distribution with magnitude can be written as:

$$log_{10}N(\geq \boldsymbol{M}) = \boldsymbol{a} - \boldsymbol{bM} \tag{5.2}$$

where N is the number of earthquakes equal to or greater than a magnitude $\boldsymbol{M}$, and $\boldsymbol{a}$ and $\boldsymbol{b}$ are scaling constants. a is proportional to the overall seismicity in a given spatio-temporal interval, whereas $\boldsymbol{b}$ represents the ratio of the number of large earthquakes to small earthquakes. The behavior of $\boldsymbol{b}$-values has been attributed to crack density (Mogi, 1962), stress drop (Wyss, 1973), and tectonic stresses (Scholz, 1968; Schorlemmer et al., 2005). We determined the magnitude of completeness ($\boldsymbol{M}_{\mathrm{C}}$) for 3,521 magnitudes based on a modified goodness-of-fit method of Wiemer and Wyss (2000), following Woo et al. (2019b). Then, we evaluated the $\boldsymbol{b}$-value for a set of magnitudes using the maximum likelihood method of Aki (1965) with a magnitude bin of 0.1. The uncertainty of $\boldsymbol{b}$-values was estimated with the method of Shi and Bolt (1982). Omori's law describes the decay rate of aftershocks. Its parameters are also broadly applied to interpret regional seismic and tectonic properties (Omori, 1894; Utsu, 1961). The extended form of Omori's law can be written as:

$$R(t) = \boldsymbol{K}(t + \boldsymbol{c})^{-\boldsymbol{p}} \tag{5.3}$$

where $\boldsymbol{K}$, $\boldsymbol{c}$, and $\boldsymbol{p}$ are the scaling coefficients that describe the aftershock decay rates in a given region. $\boldsymbol{p}$, which represents the power of the aftershock decay rates, has a range of 0.6 to 1.8 and is considered to be a function of stress and temperature in the crust (Utsu et al., 1995; Wiemer and Katsumata, 1999). We mapped the spatial variation of $\boldsymbol{p}$-values by binning 250 magnitudes and by selecting magnitudes greater than $\boldsymbol{M}_{\mathrm{C}}$. The three parameters and their associated uncertainties were determined following the maximum likelihood method presented by Ogata (1983).

5.3 Results

Of the 4,446 earthquakes with initial locations, we relocated seven foreshocks, the mainshock, and 3,938 aftershocks using hypoDD (Waldhauser and Ellsworth, 2000), having excluded earthquakes with fewer than seven traveltime difference measurements. Uncertainties of relative locations to within two standard deviations were estimated as 25 m in the east-west direction, 18 m in the north-south direction, and 37m vertically. Figure 5.2 presents the spatial distribution of aftershocks, both in plan view and cross-sections, four in the dip direction (A1-A2, B1-B2, C1-C2, and D1-D2) and one in the strike direction (E1-E2). From the map, we determined the apparent strike of aftershocks (crossline of E1-E2) to be 210°, which corresponds to the azimuth of the first principal vector obtained from two-dimensional principal component analysis (PCA) (Jolliffe, 2011). From cross-sections in the dip direction (A1-A2 to D1-D2), we observed that the spatial distribution of aftershocks delineates at least four different fault segments (Fig. 5.2). In the most northeastern part of the study area, a sub-vertical fault with a strike of 223° was identified from the aftershock distribution. An M_{L} 3.5 earthquake with a focal mechanism consistent with the inferred fault geometry occurred on this fault plane 4 days after the mainshock. Among the relocated earthquakes, the first observed event on the fault plane occurred within 72 s of the onset of the mainshock, which indicates that reactivation of the fault segment was initiated by the mainshock rupture or soon afterward. Two slightly different fault geometries, both dipping northwestward, are distinguished in the middle of sections B1-B2 and C1-C2 from the spatial distribution of the aftershocks. The aftershock distribution along B1-B2 has a wider range of focal depths, a shallower dip, and a strike closer to north-south than that of C1-C2. Both the mainshock and the M_{L} 4.3 aftershock are located adjacent to a virtual boundary of B1-B2 and C1-C2 and their focal mechanisms are consistent with the observed fault geometry. Earthquakes in the southwestern part of D1-D2 occurred after the largest aftershock (M_{L} 4.6) and their focal depths deepened to the south-east, dipping in the opposite direction to the three other fault segments observed

on A1-A2, B1-B2 and C1-C2. Such a conjugate fault geometry is clearly consistent with one nodal plane of the focal mechanism of the largest M_{L} 4.6 aftershock.

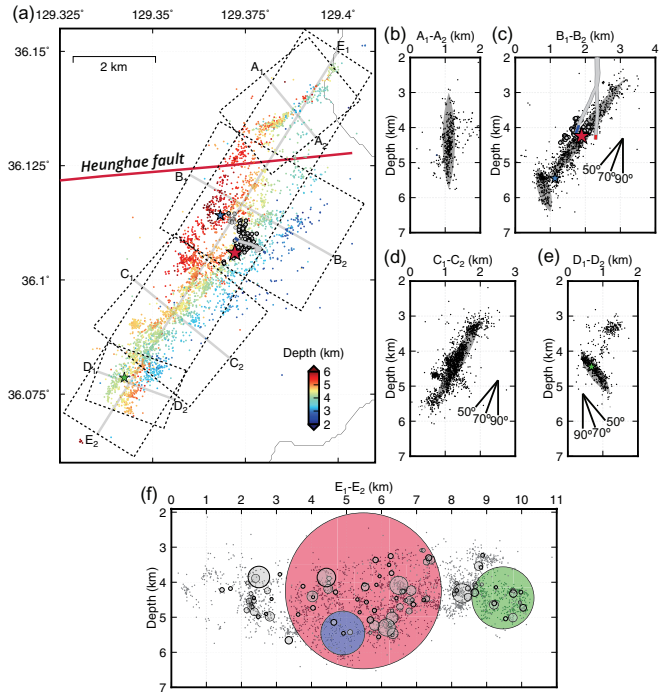

Figure 5.2: (a) Distribution of the 3946 epicenters relocated via hypoDD (Waldhauser and Ellsworth, 2000) by using traveltime differences. The earthquakes projected onto each of the cross-sections A1-A2 to E1-E2 shown in (b) to (f) fall within the rectangles denoted by dashed black lines in (a). The trajectory of two stimulation wells PX-1 and PX-2 are illustrated as gray lines in (c) with open sections colored in blue and red. The mainshock and two largest aftershocks (M_{L} 4.3 and M_{L} 4.6) are denoted as red, blue, and green stars, respectively. (b–f) Depth distribution of the relocated hypocenters along the cross-sections of A1-A2 to E1-E2. Possible interpretations for delineated faults from the aftershock distribution are marked as gray lines in (b), (c), (d), and (e). The circles in (f) represent the rupture radii of earthquakes with $M_{\mathrm{Rel}} > 1.5$, assuming a stress drop of 5.6 MPa, which corresponds to an approximated value for the mainshock estimated by the spectral ratio method (Woo et al., 2019a). The red, blue, and green circles in (f) indicate the rupture size of the three largest earthquakes with M_{L} 5.4, 4.3, and 4.6, respectively.

Table 5.2: Parameters of the faults involved in the aftershock sequences.

Properties	Fault 1 (F1)	Fault 2 (F2)	Fault 3 (F3)	Fault 4 (F4)
Strike (°)	222.7	207.4	223.1	26.3
Dip (°)	77.4	59.8	61.2	68.2
Fault length (km)	2.8	2.4	3.4	2.1
Fault width (km)	1.9	3.5	2.9	1.4
Fault thickness (km)	0.9	0.8	0.7	0.8

From the complex fault geometry delineated by the four cross-sections, we constructed a simplified fault model to describe the observed aftershock distribution. For the three segments that reactivated with the occurrence of the mainshock, we described their geometry using the aftershocks that occurred within one day of the mainshock. Because the mainshock was situated on a virtual boundary between two faults (F2 and F3) with slightly different strikes and dips, we divided the aftershock area based on the hypocenter of the mainshock and an apparent strike of 210°, which we estimated from PCA of data in map view. The aftershocks on the most northeasterly fault segment (F1) were de-clustered from the adjoining fault (F2) using the simple assumption that the Heunghae Fault vertically intersects them both. Earthquakes that occurred up to 1 day after the largest M_{L} 4.6 aftershock were used to investigate the most southwesterly fault segment (F4). Faults F1 $\sim$ F4 were used to divide the study area into four regions and earthquakes were assigned to a region on the basis of the location of their hypocenter. We applied PCA analysis with bootstrapping to earthquakes that were resampled 200 times to estimate strike, dip, fault length, and fault width. The fault length and width were determined as the difference between the 2.5th and 97.5th percentile of the strike and dip components. The resulting fault geometry is summarized in Table 2.

We determined c using the 266 relocated earthquakes with known M_{L}. We evaluated c as 0.85 by PCA (Fig. 5.3), which is larger than the case for the M_{W} magnitude scale ($c = 2/3$) scale but smaller than the case for the M_{L} magnitude scale ($c = 1$). The difference in c implies that the M_{L} magnitude does not naturally match M_{W} for earthquakes within the range of magnitudes included in this study, filtered to a frequency range of 2 – 10 Hz. The observed value of c is relatively high compared with 0.7 that was estimation using the M_{L}s of the Gyeongju aftershock sequences (Woo et al., 2019b), which may be the result of systematic differences between M_{L} and KMA magnitude. We estimated the magnitudes of 3,521 earthquakes with measurements ≥ 5. Figures 5.3b and 5.3c illustrate the comparison of M_{Rel} with M_{L} and the variations of M_{Rel} with time. Since M_{Rel} is exactly proportional to M_{L} without any scaling parameters, we propose that M_{Rel} can replace M_{L} as the magnitude scale for subsequent analysis.

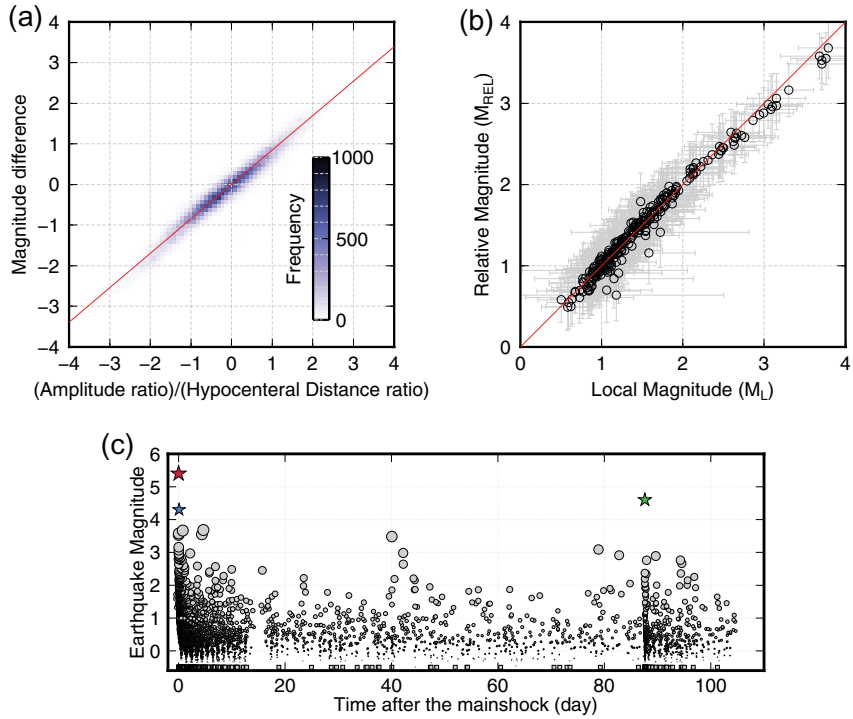

Figure 5.3: (a) Determination of the scaling parameter c in Equation (1) from known M_{L} magnitudes. The amplitude ratios measured from two similar waveforms observed at a station are measured and counted to estimate the scaling parameter for given M_{L}s. The red line indicates the scaling parameter c of 0.74 calculated from the slope of the first principal components between magnitude differences and the ratio of amplitude divided by hypocenteral distances. (b) Comparison between M_{L} and M_{Rel}. The red line indicates identity relation. (c) The distribution of earthquake magnitudes with their origin time. The three largest earthquakes (M_{L} 5.4, 4.3, and 4.6) are denoted as red, blue, and green stars, respectively, with their M_{L}s. The microearthquakes of which magnitudes cannot be measured from Equation (1) are denoted as square symbols at the bottom of the graph.

We examined temporal variations of seismic b-values by binning 600 earthquake magnitudes (M_{Rel}) into a set (Fig. 5.4a). There was an overlap of four hundred earthquakes between two consecutive bins. The M_{C} decreased from 0.8 to 0.2 during the first 3 days of the early aftershock sequence, which is indicative of a decrease in the background noise level for that period. The b-value for the first bin was evaluated as 0.66, which is consistent with b-values for earthquakes detected during fluid injection into the Pohang EGS site before the occurrence of the mainshock (Woo et al., 2019a). The b-value increased with time for the first three days up to a maximum of 0.98 and fluctuated during a month. After a month, it decreased to 0.77 until the largest aftershock of M_{L} 4.6 occurred. We tested the temporal changes of b-values with a fixed M_{C} of 0.8, corresponding to the maximum values over the whole period, to investigate whether the observed temporal variations of b-values were biased by the choice of M_{C} (gray dots of Fig. 5.4a) and confirmed that the main features were not significantly changed. Figure 5.4b illustrates the magnitude-frequency distributions of three data sets highlighted in Figure 5.4a. The spatial variation of b-values was investigated for the vertical cross-section along the apparent strike of 210°. Earthquakes within 1.5 km of each 0.5 $\times$ 0.5 km grid cell on the cross-section were binned into that cell. We analyzed the b-value only if each bin contained at least 250 earthquakes. Figure 5.4c illustrates the spatial distribution of b-values on the vertical cross-section. The estimated b-values are between 0.63 and 0.86, all of which are lower than the typically assumed b-value of 1 (Wyss, 1973). Since M_{L} is approximated by M_{Rel}, such low b-values can be interpreted as an increase in applied shear stress and effective stress (Scholz, 1968; Wyss, 1973), low material heterogeneity (Mogi, 1962), or a high stress drop (Wyss, 1973). Considering that the slip tendency of the mainshock is indicative of a critically stressed fault (Chang et al., 2020) and the stress drop of the mainshock is not higher than that of other earthquakes in South Korea (Rhee and Sheen, 2016; Woo et al., 2019a), our preferred interpretation is that the generally low b-values in the aftershock area may result from high applied stress in this region. We estimated

a $\boldsymbol{b}$-value of 0.69 near the hypocenter of the mainshock, which is comparable to the values observed for the earthquakes during the fluid injection (= 0.66).

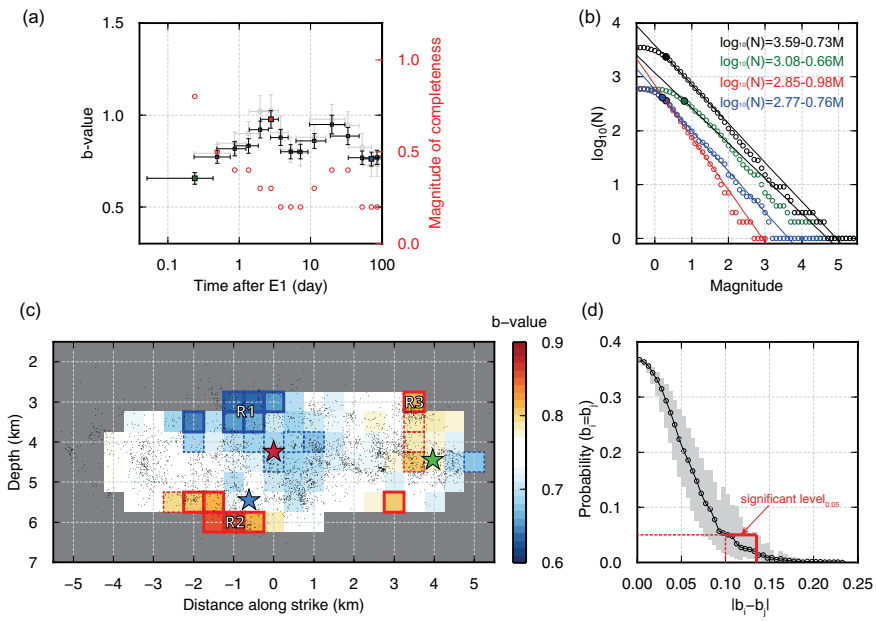

Figure 5.4: (a) Temporal variations of seismic b-values and M_C for each bin of each time period. We combined M_{Rel}s obtained from Equation (1) with M_Ls of the three largest earthquakes. A set of 600 earthquakes constitute a bin for measuring b-values and there is an overlap of 400 earthquakes between two consecutive bins. The standard deviations of each of the magnitude bins are represented as vertical and horizontal error bars. The black, red, and blue dots indicate three typical bins for the evaluation of b-values in (b). The gray dots and error bars represent b-values and their standard errors calculated based on a maximum M_C of 1 for all bins. (b) Four examples of the curves used to estimate the two scaling parameters of the G-R law. For each case, the color used for plotting the data and the equation of G-R law corresponds to a specific bin of (a). The filled circles indicate the cutoff magnitudes of M_C that honor Equation (1) for larger magnitudes. (c) Two dimensional spatial variations of b-values at a vertical profile along both the apparent strike of 212°. Hypocenters of three largest earthquakes are denoted as red, blue, and green stars, respectively. (d) Two-sigma interval distribution of probabilities that differences of paired b-values (Δb) in (c) is insignificant. The Δbs are binned by 0.05. The difference is statistically significant with a significance level of 5% if $\Delta b > 0.1$ for half the cases and $\Delta b > 0.135$ for all cases.

The significance of temporal and spatial differences in $\boldsymbol{b}$-values can be verified by Utsu's test (Utsu, 1992), in which the probability that the $\boldsymbol{b}$-values between two sets of earthquakes are the same is defined via Akaike Information Criterion (Akaike, 1974). We first tested the statistical significance of the temporal differences of $\boldsymbol{b}$-values among early (< 1 day), intermediate ($\sim$ 3 days), and late aftershocks ($\sim$ 80 days), which are highlighted in green, red, and blue, respectively, in Figs. 5.4a and 5.4b. The probability that the $\boldsymbol{b}$-value for the intermediate period is not significantly higher than those of the early and late aftershocks was estimated as 2.6×10^{-7} and 1.0×10^{-3}, respectively, indicating that the temporal increase and decrease of $\boldsymbol{b}$-values are statistically reasonable with a significance level of 5%. Similar variations of $\boldsymbol{b}$-values with time can be found for the 2016 Gyeongju earthquake (Woo et al., 2019a) and other cases (Smith, 1981; Chan et al., 2012; Gulia et al., 2018), which can be interpreted as local stress changes due to the mainshock rupture or a mixed effect of a changing spatial distribution of $\boldsymbol{b}$-value and a heterogeneous population of aftershocks with time (Fig. 5.4c). We also applied Utsu's test for all pairs of spatially varying $\boldsymbol{b}$-values for which the difference is statistically significant with a significance level of 5% if $\Delta\boldsymbol{b} > 0.1$ for half the cases and $\Delta\boldsymbol{b} > 0.135$ for all cases (Fig. 5.4d). Therefore, we roughly divided the aftershock area into three sub-regions: R1 with relatively low $\boldsymbol{b}$-values; R2 with high $\boldsymbol{b}$-values and $\Delta\boldsymbol{b} > 0.1$; and R3 with high $\boldsymbol{b}$-values and $\Delta\boldsymbol{b} > 0.135$. (Dashed lines and solid lines are used in Figure 5.4c to indicate the significant difference level of 5% with median and conservative thresholds, respectively). The $\boldsymbol{M}_{\mathrm{L}}$ 4.3 and $\boldsymbol{M}_{\mathrm{L}}$ 4.6 earthquakes are located near R2 and R3 and have high $\boldsymbol{b}$-values relative to the values of the hypocenter area (R1), which can be interpreted as indicating material heterogeneity with respect to the conjugate fault system (Figs. 5.2c and 5.2e). Alternatively, spatial variations of pore pressure or applied stress may contribute to $\boldsymbol{b}$-value heterogeneity. The $\boldsymbol{p}$-values that describe the power law decay rate of aftershocks were estimated for two data sets: (1) period A, between the onset of the mainshock and the $\boldsymbol{M}_{\mathrm{L}}$ 4.6 aftershock; and (2) period B, after the onset of $\boldsymbol{M}_{\mathrm{L}}$ 4.6 aftershock. This grouping was chosen because the

occurrence of the largest aftershock resulted in increased seismicity, which resets the decay rate for the mainshock (Fig. 5.3c). For each data set, we estimated the p-value that represents the whole data set and the spatial variation of p-values at the cross-sections along the apparent strike of 212°, with the same bins used for estimating the spatial variations of b-values. The p-value of period A was estimated as 1.10, which is larger than the value for period B (= 0.78). Such a difference may result from differing initial stress levels for periods A and B with respect to the stress perturbation of the mainshock sequence, spatial heterogeneity of the internal structure for the conjugate fault system (Fig. 5.2e; Wiemer and Katsumata (1999)), or just an insufficient number of earthquakes in the calculation of p-values for period B. With the exception of p-values for period B, the p-values of the period A were higher in the southwestern region than those in the northeastern region. This could be indicative of a spatial variation of heat flow (i.e., Kisslinger and Jones, 1991; Wiemer and Katsumata (1999)) or an insufficient number of aftershocks to allow accurate fitting of the aftershock power decay law for the southwestern aftershock region prior to the occurrence of the M_{L} 4.6 aftershock.

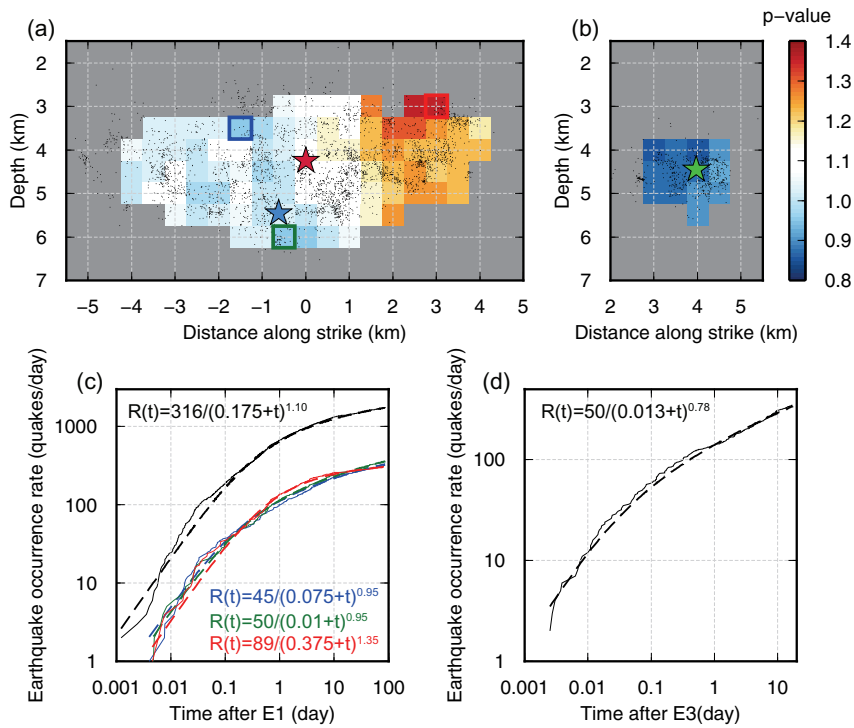

Figure 5.5: (a) Two dimensional spatial variations of $\boldsymbol{p}$-values for a cross-section along the apparent strike 212° for earthquake sequences before the occurrence of the largest aftershock (M_{L} 4.6). (b) Two dimensional spatial variations of $\boldsymbol{p}$-values for the same depth profile shown in (a), but for seismic sequences after the onset of the M_{L} 4.6 earthquake. (c and d) aftershock decay rates and their corresponding Omori's law plots with the estimated parameters obtained from the whole data set used for mapping $\boldsymbol{p}$-values in (a) and (b), respectively.

5.4 Discussion

5.4.1 Expansion of aftershock areas with time

Expansion of early aftershock sequences is widely observed (Tajima and Kanamori, 1985; Peng and Zhao, 2009; Fukuyama et al., 2003; Kato and Obara, 2014). Some temporal evolution of aftershock areas have been interpreted to be the result of afterslip or post-seismic deformation (Helmstetter and Shaw, 2009; Peng and Zhao, 2009; Perfettini et al., 2018; Ross et al., 2018). Speeds of along-strike expansion of the aftershock zone were measured on a logarithmic time scale and showed that propagating aftershock can cause the expansion of aftershocks (Peng and Zhao, 2009; Frank et al., 2017; Perfettini et al., 2018; Ross et al., 2018). In the present study, we examined the spatio-temporal distribution of aftershocks on a logarithmic time scale to consider possible post-seismic deformation following the mainshock (Fig. 5.6). In a map view, we observed that the aftershock zone has roughly expanded along the apparent strike direction, especially during the first day (Figs. 5.6a and 5.6c), whereas no clear trends were observed in a vertical sense (Fig. 5.6b).

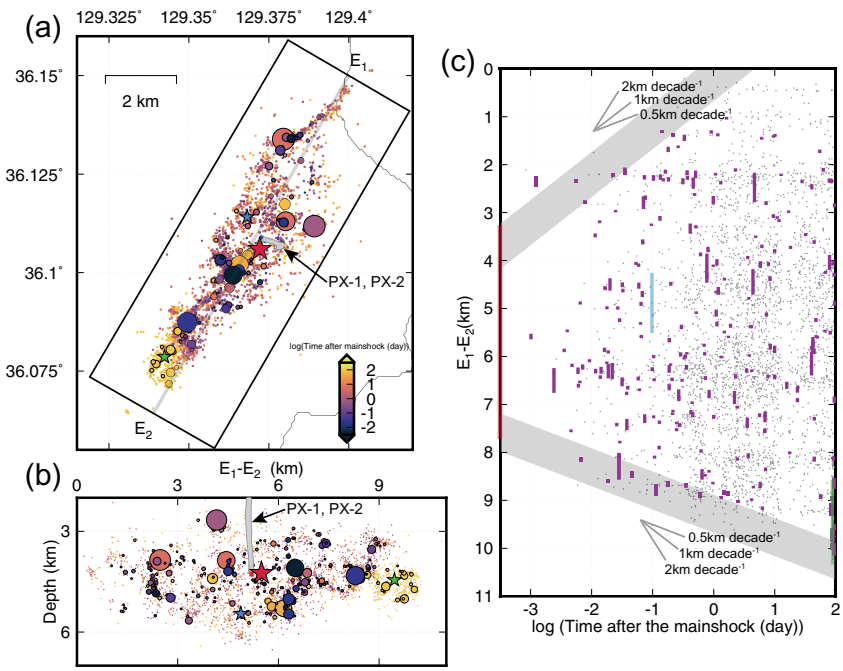

Figure 5.6: Temporal distribution of seismicity presented in (a) plan view, (b) a depth profile along the apparent strike of 212°, and (c) a unidirectional projection along the apparent strike. We illustrate the radius of earthquakes with $M_{\mathrm{Rel}} \geq 1.5$ by assuming a circular crack rupture and a stress drop of 5.6 MPa from Woo et al. (2019). In (a) and (b), the location of the mainshock and the two largest consecutive aftershocks of M_{L} 4.6 and M_{L} 5.4 are represented as red, blue and green stars, respectively. The rupture radii of the three largest earthquakes are displayed in (c) with colors to match the star symbols in (a) and (b). The trajectory of two stimulation wells PX-1 and PX-2 are illustrated as gray lines in (a) and (b). The thick gray lines in (c) represent the linear scaling relationship between the along-strike expansion of earthquake sequences with logarithmic time scale.

The speed of virtual aftershock migration fronts for the bilateral expansion along the strike direction were $\sim$ 1 km decade-1 northeastward and $\sim$ 0.5 km decade-1 southwestward (Fig. 5.6c), which may indicate post-seismic deformations related to aseismic afterslip (Peng and Zhao, 2009; Perfettini et al., 2018). The difference in the migration speeds can be attributed to different rate-and-state parameters described by Dieterich (1994) following the equations published by Perfettini et al. (2018). However, in our case, we also observe a significant $\boldsymbol{p}$-value variation in the northeastern and southwestern parts of the study area (Fig. 5.5a). Such variations of $\boldsymbol{p}$-values require a different model than the rate-dependent friction law (Helmstetter and Shaw, 2009; Mignan, 2015). Assuming that power law rheology governs post-seismic velocity (Montési, 2004), which is proportional to $(1 + t/t^*)^{-p}$, where t^* is a characteristic time of the aftershock, the slip velocity or the aftershock occurrence rate decays with time as a power of p. For regions with low $\boldsymbol{p}$-values, the slip velocity decreases relatively slowly and the accumulated post-seismic displacement required to rupture asperities can takes short time compared to that of the regions with high $\boldsymbol{p}$-values. Therefore, the $\boldsymbol{p}$-value variation observed for the aftershock area during period A may be related to the differing seismic migration speeds (Figs. 5.5a and 5.6c). We did not further compare $\boldsymbol{p}$-values and the migration speed in this study, since it may require more complex analysis than a simplified form of Omori's law (Narteau et al., 2002). Furthermore, there is an absence of data for very early (« 1 day) or late (> 100 days) aftershock rates. The expansion of the aftershock zone can also be explained by a cascade of sequentially triggered aftershocks in terms of changes to the static Coulomb stress (Ellsworth and Bulut, 2018). Since no clear evidence of post-seismic deformation was observed from differential InSAR analysis (Song and Lee, 2019), the observed expansion of aftershocks during a single day could possibly be attributed to changes to the static stress field caused by the aftershock sequences rather than a result of aseismic deformation. However, the descending image of differential InSAR reveals surface deformation during the first day after the mainshock, whereas the ascending

image reveals deformation during the next 19 days. This implies that the co-seismic deformation associated with afterslips related to the expansion of aftershock zone that occurred within 20 days of the mainshock might be captured by the InSAR image. Therefore, the possibility of afterslip-driven aftershocks cannot be discounted, even without the observation of post seismic deformation.

5.4.2 High percentage of non-DC components observed for the mainshock and two largest aftershocks

The moment tensor solutions of the mainshock and two largest earthquakes have high percentages (>30%) of non-DC components (Grigoli et al., 2018; Hong et al., 2018), in contrast to the normally observed moment tensor solutions in South Korea. Such high non-DC components of the moment tensor solutions of the three largest earthquakes can result from complex shear faulting of multiple DCs, tensile opening/closing, and shear faulting in anisotropic and heterogeneous media (Miller et al., 1998). It has already been established that the spatial distribution of the Pohang earthquake sequence indicates that multiple fault segments were reactivated in a complex fault system and the faulting types of the focal mechanism vary throughout the aftershock area (Kim et al., 2019; Chang et al., 2020). Hence, a combination of multiple DC moment tensor solutions with varying senses of slip motion could be one of the causes of the three largest earthquakes having high non-DC components. We propose the following sequence of events to explain the mainshock and major aftershock sequence associated with the M_{W} 5.5 Pohang earthquake. We infer that the nucleation of the mainshock rupture was initiated at the junction between F2 and F3 and that the rupture propagated along F2 and F3 with possible intervention of F1. Later, the M_{L} 4.3 earthquake was initiated between two adjacent conjugate faults dipping southwestward and northeastward in the deeper aftershock region below the mainshock (Fig. 5.2c). Finally, the M_{L} 4.6 earthquake nucleated at the southwestern tip of the aftershock area and subsequent aftershocks occurred on a previously unrecorded

southeastward dipping fault, suggesting that the rupture of the M_L 4.6 earthquake sequences was initiated at the intersection of conjugate faults F3 and F4. Although the three earthquakes were located at the intersection of multiple fault planes, it is hard to envisage that all the earthquakes located in the surrounding area ruptured on multiple fault planes. Some M_L 3 $\sim$ 3.6 earthquakes without non-DC components were located in the vicinity of the interconnecting faults (Choi et al., 2018), which may suggest that a certain amount of seismic energy is required for the simultaneous movement of multiple fault segments. The fault dimensions for the three largest earthquakes are inferred to be greater than 1 km, based on the assumption of a constant stress drop of 5.6 MPa on a circular crack (i.e., Fig. 5.2f), leading us to propose that a kilometer rupture scale is the threshold to rupture multiple fault planes. Low b-values observed throughout the aftershock area can be considered as stress concentrations within areas of high asperities (Wiemer and Katsumata, 1999). High asperities in the regions adjoining two or more fault segments may concentrate tectonic energy either as an earthquake nucleation point or as barriers to rupture propagation. This may explain why only $M_L > 4$ non-DC component earthquakes were observed. The sonic log data of the PX-2 borehole recorded the existence of anisotropic structures in the Pohang Basin (Ellsworth et al., 2019). Such anisotropic materials can also cause earthquakes with high non-DC components. However, it is our preferred interpretation that non-DC components in the three largest earthquakes result from the fault complexity because low, non-DC earthquakes for M_L 3 $\sim$ 3.6 earthquakes were also observed.

5.4.3 Comparison between aftershock activities and induced seismicity at the EGS site during stimulation.

The seismicity recorded during the five hydraulic stimulation experiments at the Pohang EGS site and the inferred focal mechanisms revealed a fault plane located near the PX-2 well (Woo et al., 2019). PX-2 seismicity was clustered on a plane with a strike of 214° and a dip of 43° and migrated southwestward, heading toward the loca-

tion of the mainshock (Woo et al., 2019a). However, the fault geometry for the induced earthquakes related to the PX-2 well has a 20° shallower dip angle than the moment tensor solution of the mainshock and aftershocks. It suggests that complex fault segments exist locally throughout the aftershock region and that a simple fault plane does not explain the detailed fault structures. The M_{L} 4.3 earthquakes have deeper focal depths and their focal mechanism has steeper dips than that of the mainshock, which can also be regarded as a result of complex fault geometry. Observation of various types of focal mechanisms in aftershock sequences (Kim et al., 2019; Chang et al., 2020) are also a manifestation of the complex geometry, which is in contrast to the nearly identical focal mechanisms for the PX-2 seismicity (Woo et al., 2019a). The b-values observed during the Pohang EGS project have insignificant variations, with an average value of 0.66 (Woo et al., 2019a; Langenbruch et al., 2019); whereas, the b-values estimated for the early aftershock sequences are statistically different from the b-values for a bin of approximately 3 days after the mainshock (Fig. 5.4). If we assume that b-values act as a stress-meter (Scholz, 2015; Rigo et al., 2018; Woo et al., 2019b) and temporal variation of b-values during the aftershock period represents the level of stress state, the invariant b-values observed during the stimulation period suggest that stress perturbations caused by fluid injection may be far lower than the accumulated tectonic stress, indicating the existence of a critically stressed fault system before the mainshock.

5.4.4 Reactivation of a multi-segment fault system and spatial variations of b-values and p-values

The complexity of the Pohang aftershock distributions was modeled as four fault segments, following the approach of Hong et al. (2018); Kim et al. (2018c, 2019) (Fig. 5.7. The seismicity along a subvertical fault, F1, in the northeastern of the study area clearly represents migration of the aftershock front northeastward during the first day of the aftershock sequences (Fig. 5.6). Although this fault plane is located $\sim$ 3 km

away from the mainshock hypocenter, it may have been reactivated as a part of the mainshock rupture process. Alternatively, it may have been dynamically triggered by the mainshock considering circumstantial evidence that aftershock activity on the fault segments was initiated within just 2 min and the slip distribution of the mainshock calculated from the static deformations with InSAR data is largest in the northeastern part of the fault model (Song and Lee, 2019). Aftershocks on F1 are cut by the Heunghae Fault, which has surface expression (Fig. 5.1), detaching F1 from F2 and F3. Therefore, in either case, the reactivation of F1 may require a certain stress threshold to be ruptured preferentially to F2 and F3. Two slightly different geometries of F2 and F3 are suggested by Hong et al. (2018), reflecting a complex fault system near the Pohang EGS site. While the b-values vary slightly on F2, the observed p-values were higher for F3, at least until the occurrence of the M_{L} 4.6 event. The different behaviors of the two statistical parameters imply that the two fault segments exist under different physical conditions, such as: differential stress states (Scholz, 1968), local heterogeneity of the rock matrix that may interact with viscous materials (Wyss, 1973; Bayrak et al., 2013), or variable spatial distribution of heat flow (Kisslinger and Jones, 1991). b-values decreased to ~ 0.7 when fault segment F4 was reactivated by the M_{L} 4.6 aftershock. The lower b-values may indicate F4 was already highly stressed when the M_{L} 4.6 earthquake was triggered. The observed p-values for period B were generally much lower than those for period A, which may be the result of using short time periods for analysis during period B or just uneven seismicity observed for periods A and B.

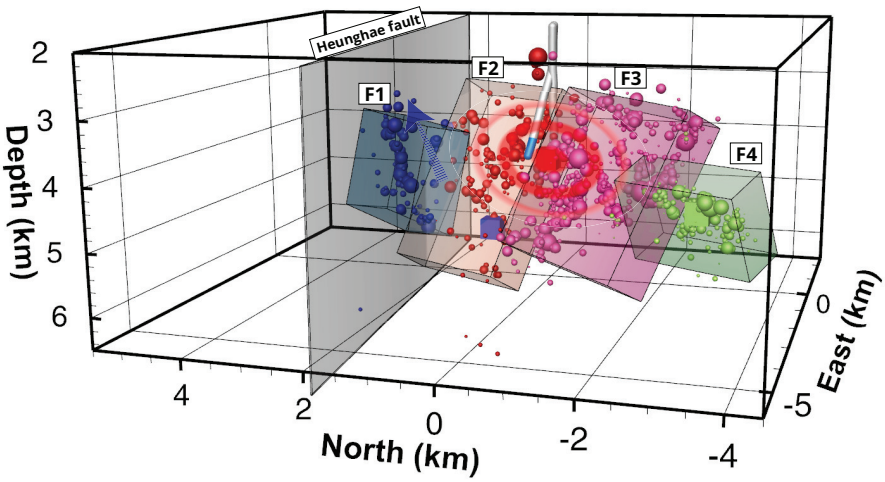

Figure 5.7: Schematic diagram that illustrates four fault segments inferred from the hydraulic stimulation wells of PX-1 and PX-2 and the distribution of aftershocks. The three cubes colored in red, blue, and green show the hypocenters of the mainshock and the two largest aftershocks of M_{L} 4.3 and 4.6, respectively. The occurrence of the mainshock triggered seismicity on fault segments F2 and F3, and possibly affected the re-activation of F1. Fault segment F4, located to the southwest of F3, was not delineated until the largest aftershock (M_{L} 4.6) occurred.

5.5 Conclusion

In this study, we detected over 4000 earthquakes related to the M_W 5.5 (M_L 5.4) Pohang earthquake by using both unsupervised data-mining and a conventional automatic earthquake detection method. From the spatio-temporal distribution of relocated seismicity, we observed that four fault segments were responsible for the aftershocks. All the faults strike northeast-southwest, but have different dip angles and dip directions. The three largest earthquakes are located at the boundaries of two adjoining fault segments, which may have focused the stress released by multiple faults, resulting in high, non-DC earthquake mechanisms. By measuring amplitude ratios between two similar earthquakes, we estimated relative magnitudes of earthquakes to infer the statistical parameters related to earthquake frequency and magnitude. The observed spatio-temporal distribution of b-values indicates that they were spatially variable, but generally as low as ~ 0.7, and increased with time. The observed p-values were different for the northeastern and southwestern parts of the study area, implying that heterogeneities in material properties such as frictional heat can lead to two different speeds of aftershock expansion rate with logarithmic time. The complexity of faulting in the aftershock zone will influence the duration and magnitude of seismic activity that is caused by the locally perturbed stress field that is a result of the mainshock We hope that our findings can be applied to aftershock mechanisms in complex fault systems in general and can be applied to provide quantitative seismic hazard assessments.

Chapter 6

Finite fault inversion of the M_{W} 5.5 2017 Pohang earthquakes: reactivation of multiple fault segments

6.1 Introduction

The M_W 5.5 Pohang earthquake that occurred on 15 November 2017 struck South Korea with strong ground motion (Kim et al., 2018c; Grigoli et al., 2018; Hong et al., 2018). The earthquake was recorded as the second largest one among the instrumentally recorded events since 1978 by Korean Meteorological Administration (KMA). With a relatively lower focal depth observed for the seismicity in South Korea, it generated unprecedented static deformations that can be recorded by InSAR images, with a few centimeters (Song and Lee, 2019). Since the earthquake occurred beneath the Pohang Basin, it generated a more significant damages compared with the 2016 M_L 5.8 Gyeongju earthquake that occurred 40km to SW direction by basin effect and liquefactions (Choi et al., 2019).

A significant issue was raised related to the Pohang mainshock because it was closely located to the Pohang enhance geothermal system (EGS) site and the termination of the last fluid stimulation experiments ended in September 2017, just two month before the mainshock and a series of multidisciplinary studies were conducted to closely examine the causal relation between fluid injection and the seismicity near the Pohang EGS site (Lee et al., 2019b; Ellsworth et al., 2019). The tight correlation between the seismic activities and the injected fluids suggest that the earthquake were triggered by the fluid injection, considering that the amount of injected volume of fluid is far small compared with the magnitude of the mainshock.

The observed aftershocks suggest that at least three multiple segments of fault planes with varying strikes and dips were reactivated by the mainshock. Evaluation of the rupture evolution in a fault system with such complex fault geometry will improve our understanding of not only the source characteristics related to rupture process but also the role of fluid in the slip propagation. A high percentage of non-double-couple components observed for the Pohang main shock (i.e., Grigoli et al. (2018) may be explained with the combination of slips on such separated fault segments with different slip vectors. The observed properties can be also important in terms of accessing

seismic hazards. The Pohang earthquake also provides a unique opportunity to validate the finite fault models with both seismic records as well as InSAR data.

In this study, we estimated a finite fault model for the Pohang mainshock by using local seismograms recorded within $\sim$ 50 km from the mainshock area based on the multiple time window inversion method, which resolves spatiotemporal slip distribution (Fig. 6.1). The fault geometries of multiple fault segments were constructed based on the aftershock distribution. The seismic velocity models for the calculation of synthetic seismograms were made for each seismic station by fitting the seismograms of smaller earthquakes evenly distributed in aftershock region. The obtained slip distribution was compared with the distribution aftershocks and statistical parameter of $\boldsymbol{b}$-value.

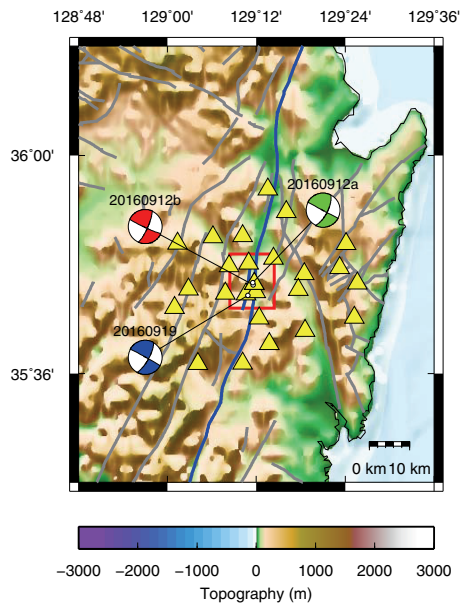

Figure 6.1: Locations of stations used for this study. Yellow and blue triangles indicate seismograms recorded by accelerometers and velocity seismometers, respectively. Major geological lineaments and faults are denoted as black lines. The Yangsang fault is highlighted as red lines. The Pohang aftershocks and the focal mechanisms solutions of the mainshock are illustrated. (Inset) The Location of Gyeongsang basin (GB) and the Yeonil Basin (YB).

6.2 Inversion method and data

The distribution of Pohang aftershock clearly indicates that multiple segments with varying strikes and dips were reactivated (Woo et al., 2019a). Simplifying such complexities in fault system can cause improper evaluation of slip images (Ragon et al., 2018). We hence considered multiple fault segments into an apriori input parameters of the finite fault inversion. Strike, dip, fault length and fault width of each fault segment were modeled based on seismicity that occurred within 1 day from the mainshock onset (Table 1). Northeast fault segment (F1) have steeper dip of x° compared to the other two segments (F2 and F3), which interconnects with each other at the location of mainshock (Fig. 6.2).

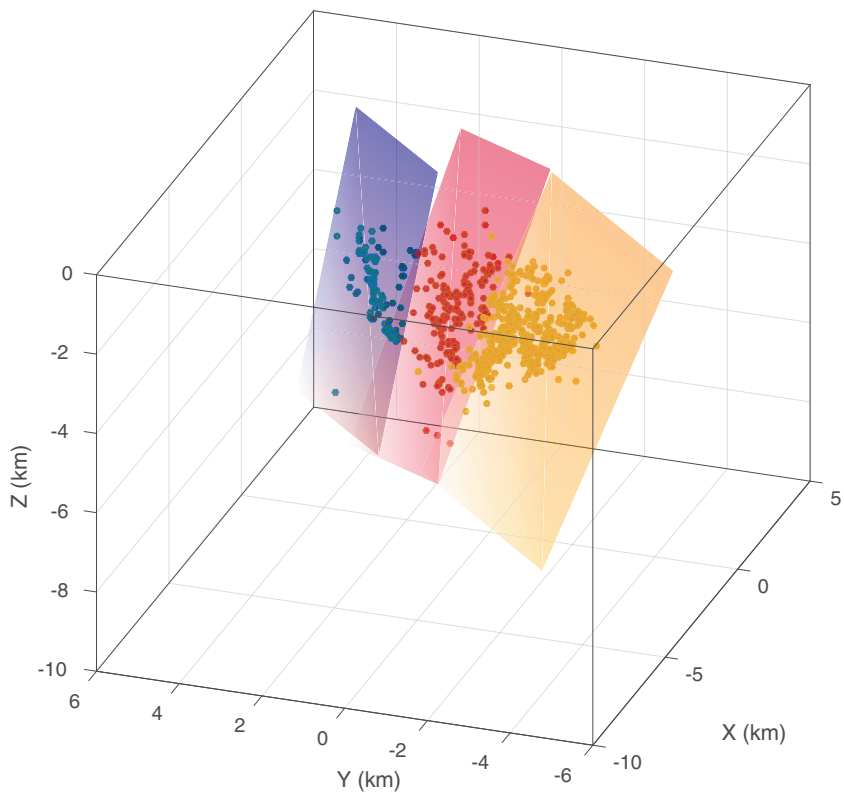

Figure 6.2: Modeling fault segments used for finite fault inversion. Detailed dividing procedures are described in the previous chapter. We used three fault segment by excluding the fault segment related to the largest aftershocks that occurred three months after the mainshock.

Table 6.1: The fault parameters of three fault segments

Fault index	Strike (°)	Dip (°)	Fault Length (km)	Fault Width (km)
F1	222	87	4	7
F2	198	58	3	7
F3	222	65	6	7

The spatiotemporal distribution of rupture process on the assumed faults was estimated by multiple-time-window linearized problem (Hartzell and Heaton 1983; ide et al., 1996; Kubo et al., 2016):

$$\boldsymbol{Gm} = \boldsymbol{d} + \boldsymbol{e} \tag{6.1}$$

where $\boldsymbol{G}$ represents a set of Green's functions calculated from each subfault and each time step, $\boldsymbol{m}$ is unknown slip amount, and $\boldsymbol{d}$ is a set of observed seismograms. Each fault segment described in Table 6.2 were divided in to 1 km × 1 km subfaults along strike and dip direction. The slip velocity function was assumed as an isosceles triangle with 1 s duration and four time steps with 0.5 s time legs were set for the multiple-time-window. The initiation of rupture process in each subfault was controlled by a circular rupture from the hypocenter of the mainshock with a constant rupture velocity (V_{rup}). The rupture directivity effect on each subfault was considered by introducing 9 point sources evenly distributed on the subfault.

To obtain reliable slip distribution and to avoid overfitting problem from a number of model parameters, we constrained slip distribution by using non-negative least-square method (Lawson and Hanson, 1974) as well as spatial and temporal smoothing regularizations in equation (1) (Ide et al., 1996). Considering that a mainshock focal mechanism favorable oriented to the aftershock distribution has a rake of $\sim$ 130° and the largest aftershock that occurred on F1 are corresponds to right-later strike slip with rake of $\sim$ 180°, two types of orthogonal slip vectors with rakes of 145 ± 45° were allowed to describe the variation of rakes on subfaults. Spatial and temporal smoothing operators were constructed as 2-D and 1-D Laplacians to the total amount of slip distributions and the time step of each subfault and rake, respectively. We optimized the two coefficients by L-curve test (Hansen and O'Leary, 1993) where the curvature is maximum for the logarithms of the L-2 norms of residual vector and model vector.

The observed waveforms that constitute the data vector in equation (1) consist of three-component seismograms recorded by 6 strong-motion seismometers and 9 broadband seismometers operated by Korean Meteorological Administration (KMA),

Korea Institute of Geoscience and Mineral Resources (KIGAM), or Korea Hydro & Nuclear Power Co (KHNP). All stations have epicentral distances up to ∼50 km from the mainshock and their azimuthal gap ranges up to ∼ 150° due to the unavailability of seismometers in coastal area (Fig. 6.1). Each seismogram with the removal of instrumental responses was cut based on the onset time of the mainshock and applied 0.05 – 1 Hz bandpass filtering and resampled as 10 Hz. In the construction of data vector, we only used 30s time window (300 data points) from 2 s before the manually picked P-wave arrival times. Synthetic seismograms used for the construction of Green's function matrix were calculated based on the AXITRA code (Cotton and Coutant, 1997) using discrete wavenumber method of (Bouchon and Aki, 1977). The updated 1-D velocity model for each seismic station was used for the calculation (See the details in the section of update seismic velocity model.). After removing third polynomial trends, they were processed in a same way with the observed seismograms. Since the seismogram generated for relative deeper subfaults has smaller amplitude, which can cause depth-dependent weights of slip amounts, we normalized the synthetic seismograms representing bases of each slip knowns by L-2 norm and multiplied obtained slip images by the normalizing factors, again.

The apparent rupture velocity (V_{rup}) which reconcile the rupture initial time at specific point on the modeled fault geometry should be properly selected based on reasonable approaches. For the given 1-D velocity model for the Pohang EGS site, the shear wave velocities ranges from 3.03 km/s to 3.51 km/s, which can be considered as the upper limit of V_{rup}. We iteratively tested a range of V_{rup} from 2.4 km/s to 5 km/s for the given inversion problems without any regularizations and measured the variance reductions between the observed and calculated waveforms. We choose the V_{rup} as 3.6 km/s that maximize the variance reduction. This can be considered to be relatively high compared with the shear velocity in the Pohang basin but the V_{rup} merely controls the upper limit of rupture initiation time on fault segments and does not directly represent a real rupture propagation speed. We applied a checkerboard test

to evaluate the resolution of inverse problem. Synthetic waveforms were made based on the checkered slip distribution with constant slip history on each subfault and it was inverted with two smoothing parameters optimized by L-curve test (Fig. 6.3). The assumed slip model with 3 km × 3 km check size was successively recovered, which suggests that the inverse problem can resolve slip distribution between three different fault segments.

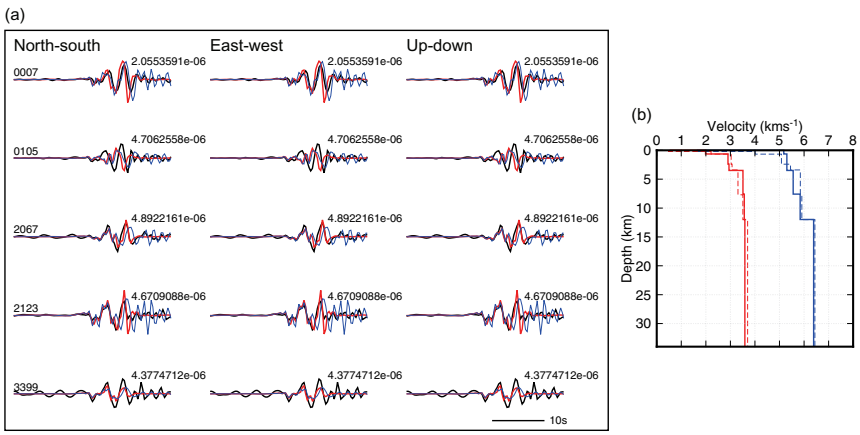

Figure 6.3: An example of improvement of velocity model for station CHS. (a) The observed waveforms (black) and synthetic waveforms calculated with initial velocity model (blue) and improved velocity model (red). The number on the right side of each waveform represents the largest amplitude of observed seismogram in meter. The number on the left side indicates the event ID used for the inversion procedure. (b) The initial velocity model (dashed lines) and the improved velocity model (solid lines) by using downhill simplex method for P-waves (blue lines) and S-waves (red lines).

6.2.1 Update of velocity model

To achieve robust finite fault models for an earthquake, assumed Green's functions as a component of inverse problem should be accurate or obtained slip images can be biased by the problem of overfitting. We therefore developed 1-D layered seismic velocity models for each station so that can explain seismograms of earthquakes in aftershock area, which can be considered as a point source relative to the rupture area of the mainshock. Considering that the displacement waveforms of most aftershocks are clearly observed due to microseism from coastal area, earthquakes with local magnitudes greater than 3 were only used for the construction of 1-D velocity models. An earthquake that occurred right after the mainshock within 10 minutes was not also used due to the coda of the mainshock. The source parameters of selected five earthquakes and the mainshock are summarized in Table 6.2.

The 1-D velocity model of each seismic station was obtained via the downhill simplex method (Nelder and Mead, 1965) which iteratively updates velocity models without any parametric derivatives. We used a 1-D initial model for the Pohang EGS site that was developed from well-logging data and seismic records from vertical seismic profiles and surface seismometers (Woo et al., 2019a). The objective function for optimization of a given model was set to the squared sum of misfits between observed and synthetic displacements for each channel of the selected earthquakes. A bandpass filter of 0.15-1 Hz was applied to each observed seismograms before the inversion and sampling rates were reduced from 100 Hz to 3.125 Hz. The program AXITRA code (Cotton and Coutant, 1997) using discrete wavenumber method of (Bouchon and Aki, 1977) was used for the calculation of synthetic seismograms. We updated 7 P- and 7 S-wave velocities of each layer as well as 6 interface depths between two connecting layers. Any low velocity layers were not allowed to avoid anomalously low/high velocities for possible tiny depth intervals and the moho depth and seismic velocities beneath the moho were fixed. Updated velocity a model effectively not only reduces the L-2 norm misfit between observed and modeled seismograms but increased the cross-correlation

Table 6.2: The source parameters of five selected earthquakes.

	Ev1	Ev2	Ev3	Ev4	Ev5
Latitude (°)	36.1077	36.0874	36.1130	36.1338	36.1021
Longitude (°)	129.3746	129.3495	129.3802	129.3796	129.3658
Depth (km)	4.146	4.318	3.865	3.851	5.291
Year	2017	2017	2017	2017	2017
Month	4	11	11	11	12
Day of month	15	15	19	19	25
Hour	2	6	14	21	7
Minute	31	9	45	5	19
Second	12.99	49.88	47.79	15.48	22.58
Julian date	105	319	323	323	359
$\boldsymbol{M_0}$ (Nm)	$7.63^{1}3$	$1.55^{1}4$	$1.2^{1}4$	$2.82^{1}4$	$1.4^{1}4$
$\boldsymbol{M}_{\mathrm{W}}$	3.2	3.4	3.4	3.6	3.4
Strike (°)	214.5	90.8	33.5	233.5	39.4
Dip (°)	58.3	74.1	84.6	84.7	81.3
Rake (°)	128	-132.4	148.5	-174	165
$\boldsymbol{K}_{\mathrm{KMA}}$	3.1	3.5	3.5	3.6	3.5

coefficient up to $\sim$ 0.7. The variance reductions $(1 - \Sigma(obs - syn)^2/\Sigma(obs)^2)$ for updated velocity models ranges from -9% to 48%. In addition to the background microseism in low frequency range (<1 Hz), limitation in the updated model may be attributed to the 2-D or 3D propagation effect, heterogeneity of density and anisotropy, existence of low velocity model and local minimization in the inverse problem.

6.3 Slip distribution of the mainshock

The finite fault model obtained by using the updated velocity model for each seismic station and optimization of smoothing constraints are illustrated in the Figs. 6.4 and 6.5. Since the three fault segments are aligned to the strike direction, we apparently paste the three segments into a fault plane. The rupture initiated at the centroid propagated to downward and SW direction on the F3 during first 1s and the maximum slip amount of $\sim$ 15 cm was observed at 1.2 s after the onset and 3 km away from the hypocenter. The rupture then propagated towards upward and NE direction for $\sim$ 1 s on the F2 and another rupture on the F1 was broadly observed during 2 $\sim$ 3.5 s after the rupture initiation. The slip rate function of the mainshock indicates that the mainshock consist of two dominant subevents at 1.2 s and 2.7 s, and they can be found at sub-regions of F3 and F1, respectively. The total seismic moment was estimated as 2.03×10$^{17} Nm$ ($\boldsymbol{M}_{\mathrm{W}}$ 5.50), from the obtained slip distribution and depth-depth shear modulus for the given initial 1-D model (Woo et al., 2019a). The variance reduction between observed and synthetic seismograms for the obtained slip model was calculated as 78.9% (Fig. 6.6).

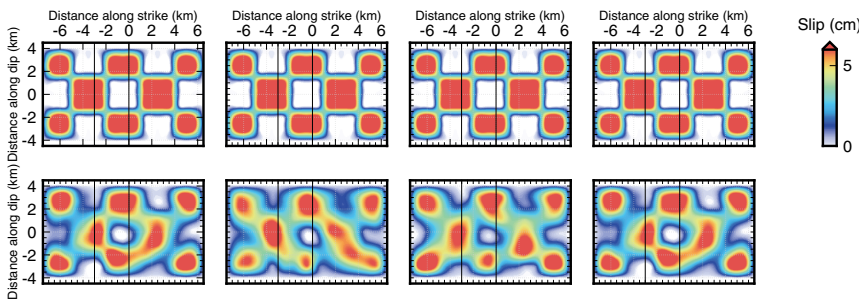

Figure 6.4: Checkerboard tests with a grid size of 3 km. (Top) The input checker board at a rupture time of 0.0, 0.5, 1.0, and 1.5 s. (Bottom) the inverted slip distribution at a rupture time of 0.0, 0.5, 1.0, and 1.5 s. Two vertical lines of each figure divides fault segments into three parts.

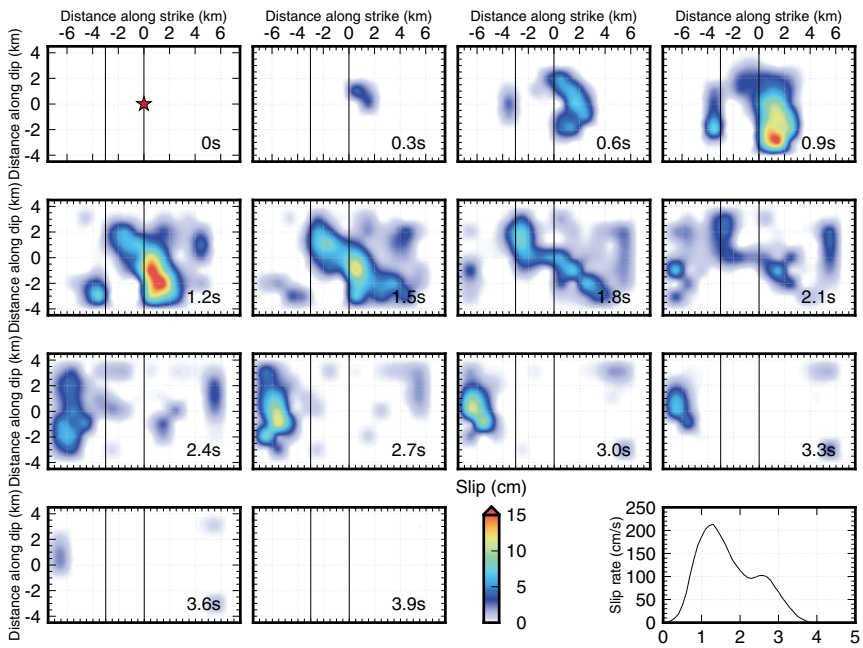

Figure 6.5: Snapshots of the slip distribution of the Pohang mainshock with a time interval of 0.3 s and the corresponding slip rate functions (right bottom). Two vertical lines of each figure divides fault segments into three parts. The mainshock is denoted as a red stars at the first snapshot.

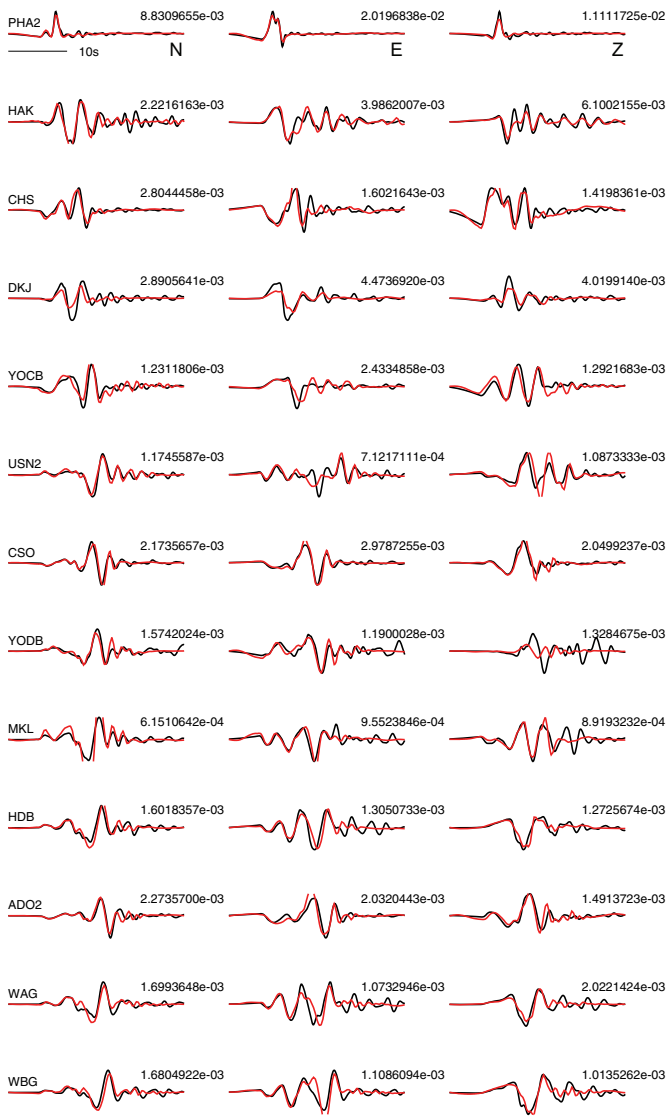

Figure 6.6: Waveform comparison between observed (black lines) and calculated waveforms (red lines) at the vertical (left), north-south (middle), and east-west components (right) of each station. The station name and the maximum amplitude of each seismogram are represented on the left side (only for the vertical components and right side. The total variance reduction was estimated as 80%.

We observed variations of rakes on the assumed fault plane from the distribution of the cumulative slip vectors (Fig. 6.7) despite of the assumption of a set of uniform rake angles in the inversion procedure. The rake of the subfault on the F1 was $\sim 180^{\circ}$ which represents typical types of right-lateral slip. On the other hand, the slip vectors of the F2 and F3 have components of both strike-slip up-dip motions and the up-dip parts of slip vectors are larger for F2. Such variation of the rake angle as well as the fault geometry can cause the high percentage of non-double-couple component of the obtained moment tensor solution of the mainshock Grigoli et al. (2018). The distribution of the stress drop was evaluated based on the obtained slip model by using the method of (Ripperger and Mai, 2004). Mean and maximum stress drop of the mainshock were estimated as 1.7 MPa and 6.6 MPa, respectively, which is distinctively matched with the geodetic slip model of Song and Lee (2019). The range of stress drop is also similar to the the stress drop estimated from the spectral ratio (Woo et al., 2019a) and comparable with the injection-induced earthquakes of 2011 M_{W} 5.6 Prague earthquakes (Sun and Hartzell, 2014) and M 5.8 Pawnee earthquake (Moschetti et al., 2019).

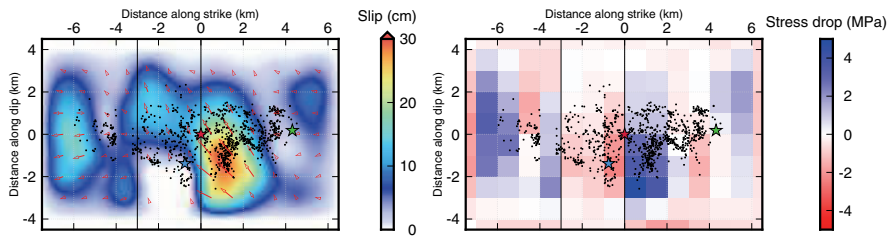

Figure 6.7: Distribution of cumulative slip (left) and stress strop (right) of the obtained finite fault model. Two vertical lines of each figure divides fault segments into three parts. The arrow represents the slip vector of each subfault. The mainshock, M_{L} 4.3 aftershock, and M_{L} 4.6 aftershock projected on fault segments are denoted as red, blue and green star, respectively. Aftershocks that occurred within 1 day after the mainshock are also projected on the fault segments (black dots). The distribution of stress drop was calculated by the method of Ripperger and Mai (2004).

We projected observed aftershock distributions for 1 day after the mainshock on the assumed fault segments to compare the aftershock density with the rupture area (Fig. 6.7). The M_{L} 4.3 aftershock that occurred 140 minutes after the mainshock are located at peripheries of the major slip area of F3, which possible resulted from a barrier (e.g., Pizzi et al. (2017)) at the deep intersection part between the F2 and F3. The M_{L} 4.6 aftershock also occurred on the edge of the assumed rupture area where the static stress changes are expected to be high. Although the seismicity observed for the F1 are inversely proportional to the slip area, overall seismicity on the F1 and F2 seems to be irrelevant to corresponding slip distributions. It can be attributed to the microstructures deviated from the assumed fault geometry in F2 and F3, with fault thickness of 590m and 480m, respectively. Fractures with mixed orientations in a complex fault system can be re-activated near or on the mainshock fault area with a time delay when the static or dynamic stress changes locally perturbs tectonic stress fields and the changed favorably orientated fault plane are in a critically state. The focal mechanisms obtained for the aftershock area also have two different populations of faulting types: thrust and strike-slip event (Chang et al., 2020; Kim et al., 2019). It represents the existence of mirocracks deviated from the assumed fault model and the similarity between the amplitudes of two smaller principal stress components.

6.4 Discussion

As expected from the aftershock distribution, we observed that the rupture process of the mainshock is concerned with at least three fault segments. Systematic differences in the slip vectors of the fault segments can resulted in the high percentage of non-double-couple component of the mainshock (Grigoli et al., 2018) by combining a couple of double-couple moment tensors although the double-couple constrained moment tensors can also explains the observed waveforms in low frequency ranges less than 0.1 Hz (Woo et al., 2019a). The different rake angles among the assumed fault

geometry can be caused by the variability of slip tendency (Morris et al., 1996) on a given fault geometry and the current stress field of which maximum principal stress is homogeneous throughout the Korean Peninsula (Soh et al., 2018). In the spatio-temporal slip distribution, fault segments were sequentially reactivated at a different rupture time, which may indicates critically stressed fault segment released tectonic stress loading towards the deeper part of F3 and the other fault segments of F2 and F1 were consecutively ruptured as a result of the previously perturbed stress due to the movement of F3. As the first reactivated fault segment, initiated rupture was propagated to SW and downwards rupture propagation, which is matched with the migrating direction of the induced seismicity observed for the stimulation periods for the PX-2. With a simple assumption that fluid can be diffused through layers with high permeability and the pore pressure changes due to fluid diffusion or poroelastic effects in heterogeneous medium can cause directional seismicity (Shapiro and Dinske, 2009; Segall and Lu, 2015), injected fluid may reduce effective normal stresses in the nearly critical stress state in F3. However, considering the amount of injected water is far short compared with the moment magnitude of earthquake (McGarr and Barbour, 2018; Woo et al., 2019a), such effect might be insignificant to perturb stress state. The coherent migration pattern can be also attributed to the aseismic creeps promoted by injected fluid by controlling rate-and-state friction law (Cappa et al., 2019) and aseismic fault slip can migrate faster than pore-pressure diffusion (Bhattacharya and Viesca, 2019), aside from the possibility that initial stress state are already built favorably to generate a self-sustained rupture process (Galis et al., 2015). Logarithmic expansion of aftershock area along the strike direction may imply the existence of the regions with a fault-strengthening behavior with aseismic deformation (Woo et al., 2019a). The rupture propagation to the F2 and then F1 has time delay compared with the F3, which also can be considered as barriers for the rupture propagation stepping into one another fault plane (Das and Aki, 1977; Aki, 1979). The role of seismic barriers is important as not only a stopper and an initiator of rupture propagation but also a stress concen-

trator (Aki, 1979; Walters et al., 2018). In this case, the bending faults of F2 and F3 and a step-over fault of F1 that was cut by Heunghae fault regulated a complex rupture process (Fig. 6.7). The regions with relatively low seismic $\boldsymbol{b}$-values observed for the Pohang aftershock statistics are generally matched with the main rupture area (Woo et al., 2019a). If we assume the $\boldsymbol{b}$-values act as a a stress meter (i.e., Schorlemmer et al. (2005); Chen et al. (2016)) and thus the lower $\boldsymbol{b}$-values represent higher stress state, such correlation suggests that the rupture propagation was initiated from the regions with high stress state. The peak slip area observed deeper than the hypocenter does not coincide with the local minima of the $\boldsymbol{b}$-values at a shallower focal depth similar to the proposition of Wiemer and Katsumata (1999), which may indicate that slip motions were controlled by the amount of asperities inferred from low $\boldsymbol{b}$-values. The delayed rupture process to the F2 by 1s could also result from the high asperities with low $\boldsymbol{b}$-values. Compared with two 2016 Gyeongju earthquakes with M_{L} >5, which represent simple rupture directivities Kim et al. (2017b); Uchide and Song (2018) at a relatively planar structure, the slip distribution of the Pohang mainshock is described in a more complex way. The Pohang mainshock has the slip duration of $\sim$ 4 s which is twice longer than the finite fault model of the Gyeongju mainshock (i.e., Uchide and Song (2018)) and the slip distribution is also far larger than that of the Gyeongju mainshock. It can be directly related to the differences in stress drops, which is significantly dependent on the focal depth (Huang et al., 2017). However, considering that $\boldsymbol{b}$-values observed throughout the Pohang aftershock area are generally lower than the Gyeongju aftershocks and the component of thrust faulting are observed only for the Pohang mainshock, higher stress regimes may partially retard the rupture propagation, which causes longer rupture duration and lower stress drop. The distribution of the slip model from the InSAR data have a simple geometry compared with our model and smaller moment magnitude (Song and Lee, 2019). Our slip model has the peak-slip areas at deeper and SW part of the aftershock area, which is different from the locations for the slip model of Song and Lee (2019). Considering that the INSAR data

generally have lower potentials for the slip resolution at deeper region, such difference can be caused by introducing a damping regularization, which avoids the overfitting of InSAR data. Smaller slip distribution of the Song and Lee (2019) than our finite fault model can be explained in terms of the regularization problem. However, the average and the peak stress drops for both finite fault model are similar to each other. We expect that the joint inversion of the seismograms and the InSAR images will gives a more robust slip distribution.

6.5 Conclusion

In this study, we estimated the slip distribution of the Pohang mainshock from widely used multiple time window method and complex fault geometries obtained by aftershock distribution. The obtained rupture propagated to SW and downward direction and generated maximum peak slips up to $\sim$ 30 cm. The rupture then propagated to the opposite direction, and slip patches located NE direction are sequentially reactivated over the potential barriers between two interconnecting fault segments. Two largest aftershocks are located on the edge of the slip distribution, which represents the existence of local asperities in assumed fault geometry. Long rupture duration of 4 s and large slip dimension of 40km2 suggest relatively low stress drops, which may be caused the retardation of rupture propagation by patches with strong asperities with a high stress state and relatively low $\boldsymbol{b}$-values of $\sim$ 0.7. Complex slip behaviors observed for the Pohang mainshock illustrate how the rupture propagate in a critically stress region with possible fluid interaction and complex fault geometries and reconcile the importance of barriers or strong asperities on fault planes than can control the seismic activates as well as the slip distribution.

Chapter 7

Discussions and concluding remarks

Throughout the previous five chapters, I analyzed detailed source parameters of the 2016 M_{L} 5.8 Gyeongju earthquake and the 2017 M_{W} 5.5 Pohang earthquake via multifaceted approaches. In this section, we briefly stated commonly observed properties for the two earthquake sequences of which the magnitude of each mainshock is greater than 5.

I observed that multiple fault segments were reactivated throughout the aftershock regions. The two largest earthquake of Gyeongju sequences of M_{L} 5.1 and M_{L} 5.8 were situated on subparallel fault planes, respectively. In the very early sequence for the M_{L} 5.1 earthquakes during 50 mins, earthquakes are clustered on the fault plane for the M_{L} 5.1 earthquake whereas the later earthquake after the mainshock were located on the other fault plane, which may hold the seismicity on the fault plane of M_{L} 5.1. I delineated at least three fault segments that were re-activated by the rupture process of the Pohang mainshock. The fault plane for the largest Gyeongju aftershock of M_{L} 4.5 that occurred 7 days after the mainshock corresponds to the conjugate fault plane which is very similar to the case for the largest Pohang aftershock of M_{L} 4.6 that occurred at a conjugated fault plane at the edge of aftershock area after 3 month from the mainshock.

The most of observed fault types of earthquake can be divided into two regimes: strike-slip fault and thrust fault. This can be explained by E-W principal stress acting throughout the Korean peninsula. The spatial variations of the amplitudes of vertical stress and minimum horizontal stress can be attributed to the faulting types and the variation can be observed in kilometer scales for the two aftershock areas for the M_{L} 5.8 Gyeongju earthquake and the M_{L} 5.4 Pohang earthquake. At a depth below $\sim$ 15 km, the faulting types of Gyeongju aftershocks were dominated by strike-slip faults, which may related from the rheological process near the brittle-ductile transition zones.

The surface rupture traces can be used for the interpretations of the observed fault geometry. Although they are usually partially deviated from the seismically observed

fault planes, it does not mean that the generation mechanisms of faults with surface expressions are not totally relevant to the deep-seated fault ruptures. They can be unfavorably aligned to the current stress field which can be considered not to be re-activated until the stress state changes. The observed fault structures have relatively steep dip angles which can be generated in the procedures for the formation of basin structures (Talwani, 2016). However, it is very challengeable to identify each potential fault systems in critically stressed, due to the resolution limitation of delineated faults via the geophysical explorations and geologic surface on surface rupture traces.

I observed increased b-value during first 3 days of aftershock sequences. This behaviors were observed for the other aftershock sequences such as 2004 ms 6.0 Parkfield earthquake (Shcherbakov et al. 2006); 1999 M_W 5.8 event between Izmit and Lake Sapanca (Raub et al. 2017). In terms of role of b-values as stress-meters, the increased b-values can be regarded as the release of stress in the aftershock region. However, the interpretation seems to require more examples of other aftershock sequences for the robustness with detailed analyses on earthquake magnitude estimation.

For the Gyeongju and Pohang earthquakes, earthquakes with magnitudes more than 4 were situated on either fault edge or the interconnecting points between two faults. The main rupture areas of the three earthquakes with M_L >5 were deviated from the hypocenter of each earthquake. These observations indicate that the initiated rupture at the edge of fault system migrated throughout the whole fault area. The slip patches of the Pohang mainshock shows bilateral propagation of the rupture front on the assumed fault model. This behavior, however, cannot be regarded as common physical properties for the intraplate earthquakes considering that the location of asperities and the possible aseismic deformations on the faults may not be correlated and the rupture process of earthquakes were diverse from region to region. Nevertheless, possible concentrations of stress on the intersection of faults may partially attribute to the common observation.

Aforementioned characteristics of source parameters for two moderate earthquakes

provide weak evidences that explain the general properties of intraplate earthquakes. With a large number of ancient recordings on the seismicity in intraplate regions and instrumental recordings with densely installed local networks, our understanding on the intraplate earthquakes can be improved via newly developed techniques for the laboratory scale of rock experiments to the regional scale observed from aftershock distribution.

Bibliography

Abdelfattah, A. K., Mogren, S., and Mukhopadhyay, M. (2017). Mapping b-value for 2009 harrat lunayyir earthquake swarm, western saudi arabia and coulomb stress for its mainshock. *Journal of Volcanology and Geothermal Research*, 330:14–23.

Adams, J., Wetmiller, R., Hasegawa, H., and Drysdale, J. (1991). The first surface faulting from a historical intraplate earthquake in north america. *Nature*, 352(6336):617–619.

Ágústsson, K., Kristjánsdóttir, S., Flóvenz, Ó. G., and Gudmundsson, O. (2015). Induced seismic activity during drilling of injection wells at the hellisheiði power plant, sw iceland. In *Proceedings World Geothermal Congress*.

Akaike, H. (1974). A new look at the statistical model identification. *IEEE transactions on automatic control*, 19(6):716–723.

Aki, K. (1965). Maximum likelihood estimate of b in the formula log n= a-bm and its confidence limits. *Bull. Earthq. Res. Inst., Tokyo Univ.*, 43:237–239.

Aki, K. (1979). Characterization of barriers on an earthquake fault. *Journal of Geophysical Research: Solid Earth*, 84(B11):6140–6148.

Aki, K. and Richards, P. G. (1980). *Quantitative Seismology: Theory and Methods*. Freeman.

Aktar, M., Özalaybey, S., Ergin, M., Karabulut, H., Bouin, M.-P., Tapırdamaz, C.,

Biçmen, F., Yörük, A., and Bouchon, M. (2004). Spatial variation of aftershock activity across the rupture zone of the 17 august 1999 izmit earthquake, turkey. *Tectonophysics*, 391(1-4):325–334.

Ansari, S. (2017). Aftershocks properties of the 2013 shonbe mw 6.3 earthquake, central zagros, iran. *Journal of Asian Earth Sciences*, 147:17–27.

Assumpçao, M., Schimmel, M., Escalante, C., Roberto Barbosa, J., Rocha, M., and Barros, L. V. (2004). Intraplate seismicity in se brazil: stress concentration in lithospheric thin spots. *Geophysical Journal International*, 159(1):390–399.

Ávila-Barrientos, L., Zúñiga, F., Rodríguez-Pérez, Q., and Guzmán-Speziale, M. (2015). Variation of b and p values from aftershocks sequences along the mexican subduction zone and their relation to plate characteristics. *Journal of South American Earth Sciences*, 63:162–171.

Baer, M. and Kradolfer, U. (1987). An automatic phase picker for local and teleseismic events. *Bulletin of the Seismological Society of America*, 77(4):1437–1445.

Baisch, S., Weidler, R., Voros, R., Wyborn, D., and de Graaf, L. (2006). Induced seismicity during the stimulation of a geothermal hfr reservoir in the cooper basin, australia. *Bulletin of the Seismological Society of America*, 96(6):2242–2256.

Bayrak, Y., Yadav, R., Kalafat, D., Tsapanos, T., Çınar, H., Singh, A., Bayrak, E., Yılmaz, Ş., Öcal, F., and Koravos, G. (2013). Seismogenesis and earthquake triggering during the van (turkey) 2011 seismic sequence. *Tectonophysics*, 601:163–176.

Bergen, K. J. and Beroza, G. C. (2018). Detecting earthquakes over a seismic network using single-station similarity measures. *Geophysical Journal International*, 213(3):1984–1998.

Bhattacharya, P. and Viesca, R. C. (2019). Fluid-induced aseismic fault slip outpaces pore-fluid migration. *Science*, 364(6439):464–468.

Bianchi, M. B., Assumpção, M., Rocha, M. P., Carvalho, J. M., Azevedo, P. A., Fontes, S. L., Dias, F. L., Ferreira, J. M., Nascimento, A. F., Ferreira, M. V., et al. (2018). The brazilian seismographic network (rsbr): improving seismic monitoring in brazil. *Seismological Research Letters*, 89(2A):452–457.

Bodin, P. and Horton, S. (2004). Source parameters and tectonic implications of aftershocks of the m w 7.6 bhuj earthquake of 26 january 2001. *Bulletin of the Seismological Society of America*, 94(3):818–827.

Bohnhoff, M., Grosser, H., and Dresen, G. (2006). Strain partitioning and stress rotation at the north anatolian fault zone from aftershock focal mechanisms of the 1999 izmit m w= 7.4 earthquake. *Geophysical Journal International*, 166(1):373–385.

Bouchon, M. and Aki, K. (1977). Discrete wave-number representation of seismic-source wave fields. *Bulletin of the Seismological Society of America*, 67(2):259–277.

Brune, J. N. (1970). Tectonic stress and the spectra of seismic shear waves from earthquakes. *Journal of geophysical research*, 75(26):4997–5009.

Byerlee, J. (1978). Friction of rocks. In *Rock friction and earthquake prediction*, pages 615–626. Springer.

Cappa, F., Scuderi, M. M., Collettini, C., Guglielmi, Y., and Avouac, J.-P. (2019). Stabilization of fault slip by fluid injection in the laboratory and in situ. *Science advances*, 5(3):eaau4065.

CF, G. B. R. (1954). Seismicity of the earth and associated phenomena. *Priceton NJ: Priceton Univ. Pr*, pages 1–310.

Chan, C.-H., Wu, Y.-M., Tseng, T.-L., Lin, T.-L., and Chen, C.-C. (2012). Spatial and temporal evolution of b-values before large earthquakes in taiwan. *Tectonophysics*, 532:215–222.

Chang, C., Lee, J. B., Kang, Tae-Seob Chang, C., Townend, J., Woo, J.-U., Rhie, J. R., Kim, J., and Park, J.-Y. (2020). Stress state and fault slip susceptibility prior to the 2017 mw 5.5 pohang earthquake triggered by enhanced geothermal system stimulation. *submitted in Geochemistry, Geophysics, Geosystems*.

Chang, C., Lee, J. B., and Kang, T.-S. (2010). Interaction between regional stress state and faults: Complementary analysis of borehole in situ stress and earthquake focal mechanism in southeastern korea. *Tectonophysics*, 485(1-4):164–177.

Chang, K. (1977). Late mesozoic stratigraphy, sedimentation and tectonics of southeastern korea. *J. Geol. Soc. Korea*, 13:76–90.

Chen, Y. (1988). *The great Tangshan earthquake of 1976: an anatomy of disaster*. Pergamon.

Chen, Y.-L., Hung, S.-H., Jiang, J.-S., and Chiao, L.-Y. (2016). Systematic correlations of the earthquake frequency-magnitude distribution with the deformation and mechanical regimes in the taiwan orogen. *Geophysical Research Letters*, 43(10):5017–5025.

Cheon, Y., Son, M., Song, C. W., Kim, J.-S., and Sohn, Y. K. (2012). Geometry and kinematics of the ocheon fault system along the boundary between the miocene pohang and janggi basins, se korea, and its tectonic implications. *Geosciences Journal*, 16(3):253–273.

Choi, J.-H., Ko, K., Gihm, Y. S., Cho, C. S., Lee, H., Song, S. G., Bang, E.-S., Lee, H.-J., Bae, H.-K., Kim, S. W., et al. (2019). Surface deformations and rupture processes associated with the 2017 m w 5.4 pohang, korea, earthquake. *Bulletin of the Seismological Society of America*, 109(2):756–769.

Cornell, C. A. (1968). Engineering seismic risk analysis. *Bulletin of the seismological society of America*, 58(5):1583–1606.

Cornet, F. H. (2016). Seismic and aseismic motions generated by fluid injections. *Geomechanics for Energy and the Environment*, 5:42–54.

Cotton, F. and Coutant, O. (1997). Dynamic stress variations due to shear faults in a plane-layered medium. *Geophysical Journal International*, 128(3):676–688.

Das, S. and Aki, K. (1977). Fault plane with barriers: a versatile earthquake model. *Journal of geophysical research*, 82(36):5658–5670.

De Barros, L., Cappa, F., Guglielmi, Y., Duboeuf, L., and Grasso, J.-R. (2019). Energy of injection-induced seismicity predicted from in-situ experiments. *Scientific reports*, 9(1):1–11.

De Gori, P., Akinci, A., Pio Lucente, F., and Kılıç, T. (2014). Spatial and temporal variations of aftershock activity of the 23 october 2011 m w 7.1 van, turkey, earthquake. *Bulletin of the Seismological Society of America*, 104(2):913–930.

Defays, D. (1977). An efficient algorithm for a complete link method. *The Computer Journal*, 20(4):364–366.

Deichmann, N. and Giardini, D. (2009). Earthquakes induced by the stimulation of an enhanced geothermal system below basel (switzerland). *Seismological Research Letters*, 80(5):784–798.

Dieterich, J. (1994). A constitutive law for rate of earthquake production and its application to earthquake clustering. *Journal of Geophysical Research: Solid Earth*, 99(B2):2601–2618.

Dreger, D., Nadeau, R. M., and Chung, A. (2007). Repeating earthquake finite source models: Strong asperities revealed on the san andreas fault. *Geophysical Research Letters*, 34(23).

Durá-Gómez, I. and Talwani, P. (2009). Finding faults in the charleston area, south carolina: 1. seismological data. *Seismological Research Letters*, 80(5):883–900.

D'Alessandro, A., Mangano, G., D'Anna, G., and Luzio, D. (2013). Waveforms clustering and single-station location of microearthquake multiplets recorded in the northern sicilian offshore region. *Geophysical Journal International*, 194(3):1789–1809.

Eisermann, A. S., Ziv, A., and Wust-Bloch, G. H. (2015). Real-time back azimuth for earthquake early warning. *Bulletin of the Seismological Society of America*, 105(4):2274–2285.

Ellsworth, W. L. (2013). Injection-induced earthquakes. *Science*, 341(6142):1225942.

Ellsworth, W. L. and Bulut, F. (2018). Nucleation of the 1999 izmit earthquake by a triggered cascade of foreshocks. *Nature Geoscience*, 11(7):531–535.

Ellsworth, W. L., Giardini, D., Townend, J., Ge, S., and Shimamoto, T. (2019). Triggering of the pohang, korea, earthquake (m w 5.5) by enhanced geothermal system stimulation. *Seismological Research Letters*, 90(5):1844–1858.

Enescu, B., Enescu, D., and Ito, K. (2011). Values of b and p: their variations and relation to physical processes for earthquakes in japan and romania. *Rom. J. Phys*, 56:590–608.

Farrell, J., Husen, S., and Smith, R. B. (2009). Earthquake swarm and b-value characterization of the yellowstone volcano-tectonic system. *Journal of Volcanology and Geothermal Research*, 188(1-3):260–276.

Ferreira, J. M., Oliveira, T., Takeya, M. K., and Assumpção, M. (1998). Superposition of local and regional stresses in northeast brazil: evidence from focal mechanisms around the potiguar marginal basin. *Geophysical Journal International*, 134(2):341–355.

Frank, W. B., Poli, P., and Perfettini, H. (2017). Mapping the rheology of the

central chile subduction zone with aftershocks. *Geophysical Research Letters*, 44(11):5374–5382.

Frohlich, C. (1992). Triangle diagrams: ternary graphs to display similarity and diversity of earthquake focal mechanisms. *Physics of the Earth and Planetary Interiors*, 75(1-3):193–198.

Fukuyama, E., Ellsworth, W. L., Waldhauser, F., and Kubo, A. (2003). Detailed fault structure of the 2000 western tottori, japan, earthquake sequence. *Bulletin of the Seismological Society of America*, 93(4):1468–1478.

Galis, M., Ampuero, J. P., Mai, P. M., and Cappa, F. (2017). Induced seismicity provides insight into why earthquake ruptures stop. *Science advances*, 3(12):eaap7528.

Galis, M., Pelties, C., Kristek, J., Moczo, P., Ampuero, J.-P., and Mai, P. M. (2015). On the initiation of sustained slip-weakening ruptures by localized stresses. *Geophysical Journal International*, 200(2):890–909.

Gangopadhyay, A. and Talwani, P. (2003). Symptomatic features of intraplate earthquakes. *Seismological Research Letters*, 74(6):863–883.

Goebel, T., Weingarten, M., Chen, X., Haffener, J., and Brodsky, E. (2017). The 2016 mw5. 1 fairview, oklahoma earthquakes: Evidence for long-range poroelastic triggering at> 40 km from fluid disposal wells. *Earth and Planetary Science Letters*, 472:50–61.

Gomberg, J., Bodin, P., and Reasenberg, P. A. (2003). Observing earthquakes triggered in the near field by dynamic deformations. *Bulletin of the Seismological Society of America*, 93(1):118–138.

Grigoli, F., Cesca, S., Amoroso, O., Emolo, A., Zollo, A., and Dahm, T. (2014). Automated seismic event location by waveform coherence analysis. *Geophysical Journal International*, 196(3):1742–1753.

Grigoli, F., Cesca, S., Dahm, T., and Krieger, L. (2012). A complex linear least-squares method to derive relative and absolute orientations of seismic sensors. *Geophysical Journal International*, 188(3):1243–1254.

Grigoli, F., Cesca, S., Rinaldi, A. P., Manconi, A., Lopez-Comino, J. A., Clinton, J., Westaway, R., Cauzzi, C., Dahm, T., and Wiemer, S. (2018). The november 2017 mw 5.5 pohang earthquake: A possible case of induced seismicity in south korea. *Science*, 360(6392):1003–1006.

Guglielmi, Y., Cappa, F., Avouac, J.-P., Henry, P., and Elsworth, D. (2015). Seismicity triggered by fluid injection–induced aseismic slip. *Science*, 348(6240):1224–1226.

Gulia, L., Rinaldi, A., Tormann, T., Vannucci, G., Enescu, B., and Wiemer, S. (2018). The effect of a mainshock on the size distribution of the aftershocks. *Geophysical Research Letters*, 45(24):13–277.

Han, M., Kim, K.-H., Son, M., and Kang, S. Y. (2017). Current microseismicity and generating faults in the gyeongju area, southeastern korea. *Tectonophysics*, 694:414–423.

Hansen, P. C. and O'Leary, D. P. (1993). The use of the l-curve in the regularization of discrete ill-posed problems. *SIAM journal on scientific computing*, 14(6):1487–1503.

Hardebeck, J. L. and Michael, A. J. (2006). Damped regional-scale stress inversions: Methodology and examples for southern california and the coalinga aftershock sequence. *Journal of Geophysical Research: Solid Earth*, 111(B11).

Hardebeck, J. L. and Shearer, P. M. (2002). A new method for determining first-motion focal mechanisms. *Bulletin of the Seismological Society of America*, 92(6):2264–2276.

Häring, M. O., Schanz, U., Ladner, F., and Dyer, B. C. (2008). Characterisation of the basel 1 enhanced geothermal system. *Geothermics*, 37(5):469–495.

Hauksson, E. and Shearer, P. (2005). Southern california hypocenter relocation with waveform cross-correlation, part 1: Results using the double-difference method. *Bulletin of the Seismological Society of America*, 95(3):896–903.

Helmstetter, A. and Shaw, B. E. (2009). Afterslip and aftershocks in the rate-and-state friction law. *Journal of Geophysical Research: Solid Earth*, 114(B1).

Hofmann, H., Zimmermann, G., Farkas, M., Huenges, E., Zang, A., Leonhardt, M., Kwiatek, G., Martinez-Garzon, P., Bohnhoff, M., Min, K.-B., et al. (2019). First field application of cyclic soft stimulation at the pohang enhanced geothermal system site in korea. *Geophysical Journal International*, 217(2):926–949.

Hong, T.-K., Lee, J., Kim, W., Hahm, I.-K., Woo, N. C., and Park, S. (2017). The 12 september 2016 ml5. 8 midcrustal earthquake in the korean peninsula and its seismic implications. *Geophysical Research Letters*, 44(7):3131–3138.

Hong, T.-K., Lee, J., Park, S., and Kim, W. (2018). Time-advanced occurrence of moderate-size earthquakes in a stable intraplate region after a megathrust earthquake and their seismic properties. *Scientific reports*, 8(1):1–8.

Hosono, K. and Yoshida, A. (2002). Do large aftershocks decrease similarly to smaller ones? *Geophysical research letters*, 29(10):120–1.

Huang, Y., Ellsworth, W. L., and Beroza, G. C. (2017). Stress drops of induced and tectonic earthquakes in the central united states are indistinguishable. *Science advances*, 3(8):e1700772.

Hwang, B.-H., Son, M., Yang, K., Yoon, J., and Ernst, W. G. (2008). Tectonic evolution of the gyeongsang basin, southeastern korea from 140 ma to the present, based

on a strike-slip and block rotation tectonic model. *International Geology Review*, 50(4):343–363.

Ide, S., Takeo, M., and Yoshida, Y. (1996). Source process of the 1995 kobe earthquake: determination of spatio-temporal slip distribution by bayesian modeling. *Bulletin of the Seismological society of America*, 86(3):547–566.

Jaeger, J. C., Cook, N. G., and Zimmerman, R. (2009). *Fundamentals of rock mechanics*. John Wiley & Sons.

Johnston, A. C. (1989). The seismicity of 'stable continental interiors'. In *Earthquakes at North-Atlantic passive margins: Neotectonics and postglacial rebound*, pages 299–327. Springer.

Jolliffe, I. (2011). International encyclopedia of statistical science. 2011. *Principal Component Analysis*, pages 1094–1096.

Kagan, Y. (1991). 3-d rotation of double-couple earthquake sources. *Geophysical Journal International*, 106(3):709–716.

Kang, S., Kim, B., Bae, S., Lee, H., and Kim, M. (2019). Earthquake-induced ground deformations in the low-seismicity region: a case of the 2017 m5. 4 pohang, south korea, earthquake. *Earthquake Spectra*, 35(3):1235–1260.

Kato, A., Fukuda, J., Nakagawa, S., and Obara, K. (2016). Foreshock migration preceding the 2016 mw 7.0 kumamoto earthquake, japan. *Geophysical Research Letters*, 43(17):8945–8953.

Kato, A. and Obara, K. (2014). Step-like migration of early aftershocks following the 2007 mw 6.7 noto-hanto earthquake, japan. *Geophysical Research Letters*, 41(11):3864–3869.

Kilb, D., Gomberg, J., and Bodin, P. (2000). Triggering of earthquake aftershocks by dynamic stresses. *Nature*, 408(6812):570–574.

Kim, H.-S., Sun, C.-G., and Cho, H.-I. (2018a). Geospatial assessment of the post-earthquake hazard of the 2017 pohang earthquake considering seismic site effects. *ISPRS International Journal of Geo-Information*, 7(9):375.

Kim, K.-H., Kang, T.-S., Rhie, J., Kim, Y., Park, Y., Kang, S. Y., Han, M., Kim, J., Park, J., Kim, M., et al. (2016a). The 12 september 2016 gyeongju earthquakes: 2. temporary seismic network for monitoring aftershocks. *Geosciences Journal*, 20(6):753–757.

Kim, K.-H., Kim, J., Han, M., Kang, S. Y., Son, M., Kang, T.-S., Rhie, J., Kim, Y., Park, Y., Kim, H.-J., et al. (2018b). Deep fault plane revealed by high-precision locations of early aftershocks following the 12 september 2016 ml 5.8 gyeongju, korea, earthquake. *Bulletin of the Seismological Society of America*, 108(1):517–523.

Kim, K.-H., Ree, J.-H., Kim, Y., Kim, S., Kang, S. Y., and Seo, W. (2018c). Assessing whether the 2017 mw 5.4 pohang earthquake in south korea was an induced event. *Science*, 360(6392):1007–1009.

Kim, K.-H., Seo, W., Han, J., Kwon, J., Kang, S. Y., Ree, J.-H., Kim, S., and Liu, K. (2019). The 2017 ml 5.4 pohang earthquake sequence, korea, recorded by a dense seismic network. *Tectonophysics*, page 228306.

Kim, M., Yoon, B., Lee, C., Park, K. G., Yoon, W.-S., Song, Y., and Lee, T. J. (2017a). Microseismic monitoring during hydraulic stimulation in pohang (korea) for egs pilot project. In *AGU Fall Meeting Abstracts*.

Kim, S., Rhie, J., and Kim, G. (2011). Forward waveform modelling procedure for 1-d crustal velocity structure and its application to the southern korean peninsula. *Geophysical Journal International*, 185(1):453–468.

Kim, S. K., Yang, J. Y., and Oh, J. (2006). Q-values for p and s waves in the southern

korean peninsula based on the coda-normalization method. *Geosciences Journal*, 10(4):465–477.

Kim, Y., He, X., Ni, S., Lim, H., and Park, S.-C. (2017b). Earthquake source mechanism and rupture directivity of the 12 september 2016 m w 5.5 gyeongju, south korea, earthquake. *Bulletin of the Seismological Society of America*, 107(5):2525–2531.

Kim, Y., Rhie, J., Kang, T.-S., Kim, K.-H., Kim, M., and Lee, S.-J. (2016b). The 12 september 2016 gyeongju earthquakes: 1. observation and remaining questions. *Geosciences Journal*, 20(6):747–752.

Kim, Y.-S., Kim, T., Kyung, J. B., Cho, C. S., Choi, J.-H., and Choi, C. U. (2017c). Preliminary study on rupture mechanism of the 9.12 gyeongju earthquake. *Journal of the Geological Society of Korea*, 53(3):407–422.

King, G. C., Stein, R. S., and Lin, J. (1994). Static stress changes and the triggering of earthquakes. *Bulletin of the Seismological Society of America*, 84(3):935–953.

Kisslinger, C. and Jones, L. M. (1991). Properties of aftershock sequences in southern california. *Journal of Geophysical Research: Solid Earth*, 96(B7):11947–11958.

Kraft, T., Herrmann, M., and Diehl, T. (2016). Analysis of induced microseismicity at the geothermal project schlattingen (canton thurgau, switzerland). Technical report, ETH Zurich.

Krieger, L. and Grigoli, F. (2015). Optimal reorientation of geophysical sensors: A quaternion-based analytical solution. *Geophysics*, 80(2):F19–F30.

Kwiatek, G., Saarno, T., Ader, T., Bluemle, F., Bohnhoff, M., Chendorain, M., Dresen, G., Heikkinen, P., Kukkonen, I., Leary, P., et al. (2019). Controlling fluid-induced seismicity during a 6.1-km-deep geothermal stimulation in finland. *Science advances*, 5(5):eaav7224.

Kyung, J. B. (2003). Paleoseismology of the yangsan fault, southeastern part of the korean peninsula. *Annals of Geophysics*, 46(5).

Lahr, J. C. (1999). *HYPOELLIPSE: A computer program for determining local earthquake hypocentral parameters, magnitude, and first motion pattern*. US Geological Survey Denver, Colorado.

Langenbruch, C., Ellsworth, W. L., Woo, J.-U., and Wald, D. J. (2019). Value at induced risk: Injection-induced seismic risk from low-probability, high-impact events. *Geophysical Research Letters*.

Laske, G. (1995). Global observation of off-great-circle propagation of long-period surface waves. *Geophysical Journal International*, 123(1):245–259.

Lay, T. and Wallace, T. C. (1995). *Modern global seismology*. Elsevier.

Lee, J., Ryoo, Y., Park, S. C., Ham, Y. M., Park, J. S., Kim, M. S., Park, S. M., Cho, H. G., Lee, K. S., Kim, I. S., et al. (2018). Seismicity of the 2016 m l 5.8 gyeongju earthquake and aftershocks in south korea. *Geosciences Journal*, 22(3):433–444.

Lee, K. and Jin, Y. G. (1991). Segmentation of the yangsan fault system: Geophysical studies on major faults in the kyeongsang basin. *지질학회지*, 27(4):434–449.

Lee, K., Yeo, I., Lee, J., Kang, T., Rhie, J., Sheen, D., Chang, C., Son, M., Cho, I., Oh, S., et al. (2019a). Summary report of the korean government commission on relations between the 2017 pohang earthquake and the egs project. *Geological Society of Korea and Korean Government Commission on the Cause of the Pohang Earthquake*, page 205.

Lee, K.-K., Ellsworth, W. L., Giardini, D., Townend, J., Ge, S., Shimamoto, T., Yeo, I.-W., Kang, T.-S., Rhie, J., Sheen, D.-H., et al. (2019b). Managing injection-induced seismic risks. *Science*, 364(6442):730–732.

Lee, M. W. (2003). *Velocity ratio and its application to predicting velocities*. US Department of the Interior, US Geological Survey.

Lee, S.-R. and Cho, K.-O. (2012). Precambrian crustal evolution of the korean peninsula. *The Journal of the Petrological Society of Korea*, 21(2):89–112.

Lee, T. J., Song, Y., Park, D.-W., Jeon, J., and Yoon, W. S. (2015). Three dimensional geological model of pohang egs pilot site, korea. In *Proceedings of the World Geothermal Congress, Melbourne, Australia*, volume 19.

Lei, X., Huang, D., Su, J., Jiang, G., Wang, X., Wang, H., Guo, X., and Fu, H. (2017). Fault reactivation and earthquakes with magnitudes of up to mw4. 7 induced by shale-gas hydraulic fracturing in sichuan basin, china. *Scientific reports*, 7(1):1–12.

Lin, J. and Stein, R. S. (2004). Stress triggering in thrust and subduction earthquakes and stress interaction between the southern san andreas and nearby thrust and strike-slip faults. *Journal of Geophysical Research: Solid Earth*, 109(B2).

Madariaga, R. and Ruiz, S. (2016). Earthquake dynamics on circular faults: A review 1970–2015. *Journal of Seismology*, 20(4):1235–1252.

Magnenet, V., Cornet, F., and Fond, C. (2017). A nontectonic origin for the present-day stress field in the paris basin (france). *Journal of Geophysical Research: Solid Earth*, 122(11):9313–9327.

Majer, E. L., Baria, R., Stark, M., Oates, S., Bommer, J., Smith, B., and Asanuma, H. (2007). Induced seismicity associated with enhanced geothermal systems. *Geothermics*, 36(3):185–222.

Martínez-Garzón, P., Kwiatek, G., Ickrath, M., and Bohnhoff, M. (2014). Msatsi: A matlab package for stress inversion combining solid classic methodology, a new simplified user-handling, and a visualization tool. *Seismological Research Letters*, 85(4):896–904.

Matos, C., Custódio, S., Batló, J., Zahradník, J., Arroucau, P., Silveira, G., and Heimann, S. (2018). An active seismic zone in intraplate west iberia inferred from high-resolution geophysical data. *Journal of Geophysical Research: Solid Earth*, 123(4):2885–2907.

Maxwell, S. (2014). *Microseismic imaging of hydraulic fracturing: Improved engineering of unconventional shale reservoirs*. Society of Exploration Geophysicists.

McGarr, A. (2014). Maximum magnitude earthquakes induced by fluid injection. *Journal of Geophysical Research: solid earth*, 119(2):1008–1019.

McGarr, A. and Barbour, A. J. (2018). Injection-induced moment release can also be aseismic. *Geophysical Research Letters*, 45(11):5344–5351.

Mendoza, C. and Hartzell, S. H. (1988). Aftershock patterns and main shock faulting. *Bulletin of the Seismological Society of America*, 78(4):1438–1449.

Meng, L., Ampuero, J.-P., Stock, J., Duputel, Z., Luo, Y., and Tsai, V. (2012). Earthquake in a maze: Compressional rupture branching during the 2012 mw 8.6 sumatra earthquake. *Science*, 337(6095):724–726.

Michael, A. J. (1984). Determination of stress from slip data: faults and folds. *Journal of Geophysical Research: Solid Earth*, 89(B13):11517–11526.

Mignan, A. (2015). Modeling aftershocks as a stretched exponential relaxation. *Geophysical Research Letters*, 42(22):9726–9732.

Miller, A. D., Foulger, G., and Julian, B. R. (1998). Non-double-couple earthquakes 2. observations. *Reviews of Geophysics*, 36(4):551–568.

Mogi, K. (1962). Study of the elastic shocks caused by the fracture of heterogeneous materials and its relation to earthquakes phenomena. *Bulletin of the Earthquake Research Institute*, 40:125–173.

Montési, L. G. (2004). Controls of shear zone rheology and tectonic loading on post-seismic creep. *Journal of Geophysical Research: Solid Earth*, 109(B10).

Morris, A., Ferrill, D. A., and Henderson, D. B. (1996). Slip-tendency analysis and fault reactivation. *Geology*, 24(3):275–278.

Moschetti, M. P., Hartzell, S. H., and Herrmann, R. (2019). Rupture model of the m5. 8 pawnee, oklahoma, earthquake from regional and teleseismic waveforms. *Geophysical Research Letters*, 46(5):2494–2502.

Mukuhira, Y., Dinske, C., Asanuma, H., Ito, T., and Häring, M. (2017). Pore pressure behavior at the shut-in phase and causality of large induced seismicity at basel, switzerland. *Journal of Geophysical Research: Solid Earth*, 122(1):411–435.

Murru, M., Console, R., Falcone, G., Montuori, C., and Sgroi, T. (2007). Spatial mapping of the b value at mount etna, italy, using earthquake data recorded from 1999 to 2005. *Journal of Geophysical Research: Solid Earth*, 112(B12).

Narteau, C., Shebalin, P., and Holschneider, M. (2002). Temporal limits of the power law aftershock decay rate. *Journal of Geophysical Research: Solid Earth*, 107(B12):ESE–12.

Nelder, J. A. and Mead, R. (1965). A simplex method for function minimization. *The computer journal*, 7(4):308–313.

Noda, S., Yamamoto, S., Sato, S., Iwata, N., Korenaga, M., and Ashiya, K. (2012). Improvement of back-azimuth estimation in real-time by using a single station record. *Earth, planets and space*, 64(3):305–308.

of Korea, G. S. (1998). Geology of korea.

Ogata, Y. (1983). Estimation of the parameters in the modified omori formula for aftershock frequencies by the maximum likelihood procedure. *Journal of Physics of the Earth*, 31(2):115–124.

Ogata, Y. (1998). Space-time point-process models for earthquake occurrences. *Annals of the Institute of Statistical Mathematics*, 50(2):379–402.

Ogwari, P. and Horton, S. (2016). Numerical model of pore-pressure diffusion associated with the initiation of the 2010–2011 guy–greenbrier, arkansas earthquakes. *Geofluids*, 16(5):954–970.

Park, S.-C., Yang, H., Lee, D. K., Park, E. H., and Lee, W.-J. (2018). Did the 12 september 2016 gyeongju, south korea earthquake cause surface deformation? *Geosciences Journal*, 22(2):337–346.

Peng, Z. and Zhao, P. (2009). Migration of early aftershocks following the 2004 parkfield earthquake. *Nature Geoscience*, 2(12):877–881.

Perfettini, H., Frank, W., Marsan, D., and Bouchon, M. (2018). A model of aftershock migration driven by afterslip. *Geophysical Research Letters*, 45(5):2283–2293.

Pizzi, A., Di Domenica, A., Gallovič, F., Luzi, L., and Puglia, R. (2017). Fault segmentation as constraint to the occurrence of the main shocks of the 2016 central italy seismic sequence. *Tectonics*, 36(11):2370–2387.

Prejean, S. G. and Ellsworth, W. L. (2001). Observations of earthquake source parameters at 2 km depth in the long valley caldera, eastern california. *Bulletin of the Seismological Society of America*, 91(2):165–177.

Rabak, I., Langston, C., Bodin, P., Horton, S., Withers, M., and Powell, C. (2010). The enola, arkansas, intraplate swarm of 2001. *Seismological Research Letters*, 81(3):549–559.

Ragon, T., Sladen, A., and Simons, M. (2018). Accounting for uncertain fault geometry in earthquake source inversions–i: theory and simplified application. *Geophysical Journal International*, 214(2):1174–1190.

Rastogi, B., Gupta, H., Mandal, P., Satyanarayana, H., Kousalya, M., Raghavan, R., Jain, R., Sarma, A., Kumar, N., and Satyamurty, C. (2001). The deadliest stable continental region earthquake occurred near bhuj on 26 january 2001. *Journal of Seismology*, 5(4):609–615.

Raub, C., Martínez-Garzón, P., Kwiatek, G., Bohnhoff, M., and Dresen, G. (2017). Variations of seismic b-value at different stages of the seismic cycle along the north anatolian fault zone in northwestern turkey. *Tectonophysics*, 712:232–248.

Reasenberg, P. A. and Simpson, R. W. (1992). Response of regional seismicity to the static stress change produced by the loma prieta earthquake. *Science*, 255(5052):1687–1690.

Rhee, H.-M. and Sheen, D.-H. (2016). Lateral variation in the source parameters of earthquakes in the korean peninsula. *Bulletin of the Seismological Society of America*, 106(5):2266–2274.

Rigo, A., Souriau, A., and Sylvander, M. (2018). Spatial variations of b-value and crustal stress in the pyrenees. *Journal of Seismology*, 22(1):337–352.

Ripperger, J. and Mai, P. (2004). Fast computation of static stress changes on 2d faults from final slip distributions. *Geophysical research letters*, 31(18).

Robinson, D., Henry, C., Das, S., and Woodhouse, J. (2001). Simultaneous rupture along two conjugate planes of the wharton basin earthquake. *Science*, 292(5519):1145–1148.

Rong, K., Yoon, C. E., Bergen, K. J., Elezabi, H., Bailis, P., Levis, P., and Beroza, G. C. (2018). Locality-sensitive hashing for earthquake detection: a case study of scaling data-driven science. *Proceedings of the VLDB Endowment*, 11(11):1674–1687.

Ross, Z. E., Kanamori, H., Hauksson, E., and Aso, N. (2018). Dissipative intraplate

faulting during the 2016 mw 6.2 tottori, japan earthquake. *Journal of Geophysical Research: Solid Earth*, 123(2):1631–1642.

Sabbione, J. I. and Velis, D. R. (2013). A robust method for microseismic event detection based on automatic phase pickers. *Journal of Applied Geophysics*, 99:42–50.

Schoenball, M. and Ellsworth, W. L. (2017). A systematic assessment of the spatiotemporal evolution of fault activation through induced seismicity in oklahoma and southern kansas. *Journal of Geophysical Research: Solid Earth*, 122(12):10–189.

Scholz, C. (1968). The frequency-magnitude relation of microfracturing in rock and its relation to earthquakes. *Bulletin of the seismological society of America*, 58(1):399–415.

Scholz, C. H. (2015). On the stress dependence of the earthquake b value. *Geophysical Research Letters*, 42(5):1399–1402.

Schorlemmer, D., Wiemer, S., and Wyss, M. (2005). Variations in earthquake-size distribution across different stress regimes. *Nature*, 437(7058):539–542.

Schultz, R., Wang, R., Gu, Y. J., Haug, K., and Atkinson, G. (2017). A seismological overview of the induced earthquakes in the duvernay play near fox creek, alberta. *Journal of Geophysical Research: Solid Earth*, 122(1):492–505.

Segall, P. and Lu, S. (2015). Injection-induced seismicity: Poroelastic and earthquake nucleation effects. *Journal of Geophysical Research: Solid Earth*, 120(7):5082–5103.

Shapiro, S. (2018). Seismogenic index of underground fluid injections and productions. *Journal of Geophysical Research: Solid Earth*, 123(9):7983–7997.

Shapiro, S. A. and Dinske, C. (2009). Fluid-induced seismicity: Pressure diffusion and hydraulic fracturing. *Geophysical Prospecting*, 57(2):301–310.

Shapiro, S. A., Dinske, C., and Kummerow, J. (2007). Probability of a given-magnitude earthquake induced by a fluid injection. *Geophysical research letters*, 34(22).

Shapiro, S. A., Dinske, C., Langenbruch, C., and Wenzel, F. (2010). Seismogenic index and magnitude probability of earthquakes induced during reservoir fluid stimulations. *The Leading Edge*, 29(3):304–309.

Shcherbakov, R., Turcotte, D. L., and Rundle, J. B. (2006). Scaling properties of the parkfield aftershock sequence. *Bulletin of the Seismological Society of America*, 96(4B):S376–S384.

Sheen, D.-H., Kang, T.-S., and Rhie, J. (2018). A local magnitude scale for south koreaa local magnitude scale for south korea. *Bulletin of the Seismological Society of America*, 108(5A):2748–2755.

Shelly, D. R., Beroza, G. C., and Ide, S. (2007). Non-volcanic tremor and low-frequency earthquake swarms. *Nature*, 446(7133):305–307.

Shelly, D. R., Ellsworth, W. L., and Hill, D. P. (2016). Fluid-faulting evolution in high definition: Connecting fault structure and frequency-magnitude variations during the 2014 long valley caldera, california, earthquake swarm. *Journal of Geophysical Research: Solid Earth*, 121(3):1776–1795.

Shi, Y. and Bolt, B. A. (1982). The standard error of the magnitude-frequency b value. *Bulletin of the Seismological Society of America*, 72(5):1677–1687.

Sibson, R. (1973). Slink: an optimally efficient algorithm for the single-link cluster method. *The computer journal*, 16(1):30–34.

Smith, W. D. (1981). The b-value as an earthquake precursor. *Nature*, 289(5794):136–139.

Snoke, J. A. (2003). Focmec: Focal mechanism determinations. *International Handbook of Earthquake and Engineering Seismology*, 85:1629–1630.

So, M., Mote, T., and Pappin, J. (2016). Seismic hazard assessment of south korea. *Japanese Geotechnical Society Special Publication*, 2(20):755–760.

Soh, I., Chang, C., Lee, J., Hong, T.-K., and Park, E.-S. (2018). Tectonic stress orientations and magnitudes, and friction of faults, deduced from earthquake focal mechanism inversions over the korean peninsula. *Geophysical Journal International*, 213(2):1360–1373.

Sokos, E. N. and Zahradnik, J. (2008). Isola a fortran code and a matlab gui to perform multiple-point source inversion of seismic data. *Computers & Geosciences*, 34(8):967–977.

Son, M., Cho, C. S., Shin, J. S., Rhee, H.-M., and Sheen, D.-H. (2018). Spatiotemporal distribution of events during the first three months of the 2016 gyeongju, korea, earthquake sequencespatiotemporal distribution of events during the first three months of the 2016 gyeongju earthquake sequence. *Bulletin of the Seismological Society of America*, 108(1):210–217.

Son, M., Chong, H., and Kim, I. (2002). Geology and geological structures in the vicinities of the southern part of the yonil tectonic line, se korea. *Journal of the geological society of Korea*, 38(2):175–197.

Son, M., Song, C., Kim, M.-C., Cheon, Y., Cho, H., and Sohn, Y. (2015). Miocene tectonic evolution of the basins and fault systems, se korea: dextral, simple shear during the east sea (sea of japan) opening. *Journal of the Geological society*, 172(5):664–680.

Song, C. (2015). Study on the evolution of the miocene pohang basin based on its structural characteristics. *Unpublished Ph. D. Thesis, Pusan National University, Busan*.

Song, S. G. and Lee, H. (2019). Static slip model of the 2017 m w 5.4 pohang, south korea, earthquake constrained by the insar data. *Seismological Research Letters*, 90(1):140–148.

Soto-Cordero, L., Meltzer, A., and Stachnik, J. (2018). Crustal structure, intraplate seismicity, and seismic hazard in the mid-atlantic united states. *Seismological Research Letters*, 89(1):241–252.

Sun, X. and Hartzell, S. (2014). Finite-fault slip model of the 2011 mw 5.6 prague, oklahoma earthquake from regional waveforms. *Geophysical Research Letters*, 41(12):4207–4213.

Sykes, L. R. (1978). Intraplate seismicity, reactivation of preexisting zones of weakness, alkaline magmatism, and other tectonism postdating continental fragmentation. *Reviews of Geophysics*, 16(4):621–688.

Tajima, F. and Kanamori, H. (1985). Global survey of aftershock area expansion patterns. *Physics of the Earth and planetary interiors*, 40(2):77–134.

Talwani, P. (2014). Unified model for intraplate earthquakes.

Talwani, P. and Rajendran, K. (1991). Some seismological and geometric features of intraplate earthquakes. *Tectonophysics*, 186(1-2):19–41.

Tavakoli, B., Pezeshk, S., and Cox, R. T. (2010). Seismicity of the new madrid seismic zone derived from a deep-seated strike-slip fault. *Bulletin of the Seismological Society of America*, 100(4):1646–1658.

Toda, S., Stein, R., Richards-Dinger, K., and Bozkurt, S. (2005). Forecasting the evolution of seismicity in southern california: Animations built on earthquake stress transfer. *Journal of Geophysical Research:Solid Earth*, 110(B5).

Tormann, T., Wiemer, S., and Mignan, A. (2014). Systematic survey of high-resolution

b value imaging along californian faults: Inference on asperities. *Journal of Geophysical Research: Solid Earth*, 119(3):2029–2054.

Townend, J. and Zoback, M. D. (2000). How faulting keeps the crust strong. *Geology*, 28(5):399–402.

Trnkoczy, A. (1999). Topic understanding and parameter setting of sta/lta trigger algorithm. *New manual of seismological observatory practice*, 2.

Tsuboi, S., Abe, K., Takano, K., and Yamanaka, Y. (1995). Rapid determination of mw from broadband p waveforms. *Bulletin of the Seismological Society of America*, 85(2):606–613.

Uchide, T. and Song, S. G. (2018). Fault rupture model of the 2016 gyeongju, south korea, earthquake and its implication for the underground fault system. *Geophysical Research Letters*, 45(5):2257–2264.

Utsu, T. (1992). On seismicity. *Report of the Joint Research Institute for Statistical Mathematics, Inst. for Stat. Math., Tokyo*, pages 139–157.

Utsu, T., Ogata, Y., et al. (1995). The centenary of the omori formula for a decay law of aftershock activity. *Journal of Physics of the Earth*, 43(1):1–33.

Van der Elst, N. J., Page, M. T., Weiser, D. A., Goebel, T. H., and Hosseini, S. M. (2016). Induced earthquake magnitudes are as large as (statistically) expected. *Journal of Geophysical Research: Solid Earth*, 121(6):4575–4590.

Vavryčuk, V. (2014). Iterative joint inversion for stress and fault orientations from focal mechanisms. *Geophysical Journal International*, 199(1):69–77.

Wadati, K. and Oki, S. (1933). On the travel time of earthquake waves.(part ii). *Journal of the Meteorological Society of Japan. Ser. II*, 11(1):14–28.

Waldhauser, F. and Ellsworth, W. L. (2000). A double-difference earthquake location algorithm: Method and application to the northern hayward fault, california. *Bulletin of the Seismological Society of America*, 90(6):1353–1368.

Walters, R. J., Gregory, L. C., Wedmore, L. N., Craig, T. J., McCaffrey, K., Wilkinson, M., Chen, J., Li, Z., Elliott, J. R., Goodall, H., et al. (2018). Dual control of fault intersections on stop-start rupture in the 2016 central italy seismic sequence. *Earth and Planetary Science Letters*, 500:1–14.

Wang, Z. (2007). Seismic hazard and risk assessment in the intraplate environment: The new madrid seismic zone of the central united states. *SPECIAL PAPERS-GEOLOGICAL SOCIETY OF AMERICA*, 425:363.

Westerhaus, M., Wyss, M., Yilmaz, R., and Zschau, J. (2002). Correlating variations of b values and crustal deformations during the 1990s may have pinpointed the rupture initiation of the m w= 7.4 izmit earthquake of 1999 august 17. *Geophysical Journal International*, 148(1):139–152.

Wiemer, S. and Katsumata, K. (1999). Spatial variability of seismicity parameters in aftershock zones. *Journal of Geophysical Research: Solid Earth*, 104(B6):13135–13151.

Wiemer, S. and Wyss, M. (2000). Minimum magnitude of completeness in earthquake catalogs: Examples from alaska, the western united states, and japan. *Bulletin of the Seismological Society of America*, 90(4):859–869.

Withers, M., Aster, R., Young, C., Beiriger, J., Harris, M., Moore, S., and Trujillo, J. (1998). A comparison of select trigger algorithms for automated global seismic phase and event detection. *Bulletin of the Seismological Society of America*, 88(1):95–106.

Woo, J.-U., Kim, J., Rhie, J., and Kang, T.-S. (2017). Characteristics in hypocenters

of microseismic events due to hydraulic fracturing and natural faults: a case study in the horn river basin, canada. *Geosciences Journal*, 21(5):683–694.

Woo, J.-U., Kim, M., Sheen, D.-H., Kang, T.-S., Rhie, J., Grigoli, F., Ellsworth, W., and Giardini, D. (2019a). An in-depth seismological analysis revealing a causal link between the 2017 mw 5.5 pohang earthquake and egs project. *Journal of Geophysical Research: Solid Earth*.

Woo, J.-U., Rhie, J., Kim, S., Kang, T.-S., Kim, K.-H., and Kim, Y. (2019b). The 2016 gyeongju earthquake sequence revisited: aftershock interactions within a complex fault system. *Geophysical Journal International*, 217(1):58–74.

Wu, Q., Chapman, M., and Beale, J. (2015). The aftershock sequence of the 2011 mineral, virginia, earthquake: Temporal and spatial distribution, focal mechanisms, regional stress, and the role of coulomb stress transfer. *Bulletin of the Seismological Society of America*, 105(5):2521–2537.

Wyss, M. (1973). Towards a physical understanding of the earthquake frequency distribution. *Geophysical Journal of the Royal Astronomical Society*, 31(4):341–359.

Yano, T. E. and Matsubara, M. (2017). Effect of newly refined hypocenter locations on the seismic activity recorded during the 2016 kumamoto earthquake sequence. *Earth, Planets and Space*, 69(1):74.

Yeck, W. L., Weingarten, M., Benz, H. M., McNamara, D. E., Bergman, E., Herrmann, R., Rubinstein, J. L., and Earle, P. (2016). Far-field pressurization likely caused one of the largest injection induced earthquakes by reactivating a large preexisting basement fault structure. *Geophysical Research Letters*, 43(19):10–198.

Yoon, C. E., Bergen, K. J., Rong, K., Elezabi, H., Ellsworth, W. L., Beroza, G. C., Bailis, P., and Levis, P. (2019a). Unsupervised large-scale search for similar earthquake signals. *Bulletin of the Seismological Society of America*, 109(4):1451–1468.

Yoon, C. E., Huang, Y., Ellsworth, W. L., and Beroza, G. C. (2017). Seismicity during the initial stages of the guy-greenbrier, arkansas, earthquake sequence. *Journal of Geophysical Research: Solid Earth*, 122(11):9253–9274.

Yoon, C. E., O'Reilly, O., Bergen, K. J., and Beroza, G. C. (2015). Earthquake detection through computationally efficient similarity search. *Science advances*, 1(11):e1501057.

Yoon, C. E., Yoshimitsu, N., Ellsworth, W. L., and Beroza, G. C. (2019b). Foreshocks and mainshock nucleation of the 1999 m w 7.1 hector mine, california, earthquake. *Journal of Geophysical Research: Solid Earth*, 124(2):1569–1582.

Yoon, S., Sohn, Y., and Chough, S. (2014). Tectonic, sedimentary, and volcanic evolution of a back-arc basin in the east sea (sea of japan). *Marine Geology*, 352:70–88.

Yoshida, K. and Hasegawa, A. (2018). Hypocenter migration and seismicity pattern change in the yamagata-fukushima border, ne japan, caused by fluid movement and pore pressure variation. *Journal of Geophysical Research: Solid Earth*, 123(6):5000–5017.

Yun, H. (1994). Emended stratigraphy of the miocene formations in the pohang basin, part ii: south of the hyongsan fault. *J. Paleontl. Soc. Korea*, 10:99–116.

Zang, A., Oye, V., Jousset, P., Deichmann, N., Gritto, R., McGarr, A., Majer, E., and Bruhn, D. (2014). Analysis of induced seismicity in geothermal reservoirs–an overview. *Geothermics*, 52:6–21.

Zhang, M. and Wen, L. (2015). An effective method for small event detection: match and locate (m&l). *Geophysical Journal International*, 200(3):1523–1537.

Zhao, Y. and Wu, Z. (2008). Mapping the b-values along the longmenshan fault zone before and after the 12 may 2008, wenchuan, china, ms 8.0 earthquake. *Natural Hazards & Earth System Sciences*, 8(6).

Zoback, M. L. (1992). First-and second-order patterns of stress in the lithosphere: The world stress map project. *Journal of Geophysical Research: Solid Earth*, 97(B8):11703–11728.

Appendices

A Supporting Information for An in-depth seismological analysis revealing a causal link between the 2017 M_W 5.5 Pohang earthquake and EGS project

Text S1 describes the detailed procedures for the construction of a local 1-D velocity model. The 1-D model was used to locate events, measure their magnitudes, and determine their focal mechanisms. Text S2 is a procedure for the determination of a key event, which was recorded at the PX-2 borehole chain in August 2017. Text S3 provides the information on the site correction terms in the procedure for magnitude determination. Figure S1 represents the period of operation of the seismic stations used in this study. Figures S2 to S6 show the timeline of the hydraulic stimulations and earthquake sequences near the EGS site. Figures S7 and S8 illustrate the spatial distribution of events classified by two different clustering methods and the dendrogram of the waveform clustering analysis, respectively. Figure S9 illustrates the geometry of the PX-2 borehole chain that was operated during the soft stimulation at PX-1 in August 2017. Figures S10 to S12 illustrate examples of hodograms used to measure station orientations. Figure S13 is an example of measuring the azimuth of the key event. Figure S14 depicts the procedure for locating the key event using the records at the PX-2 borehole chain. Figures S15 and S16 are examples of the seismograms of the observed tube waves and the procedure for locating the key event using the arrival times of the tube waves.

Table A.1 lists detailed information on the seismic stations used in this study. Table A.2 lists the templates that were used in the event detection procedure. Table A.3 lists the information used to determine the key event location.

A.1 Construction of a local 1-D seismic velocity model for the Pohang EGS site

A 1-D seismic velocity model developed in this study was built based on the changes in the seismic velocities. Among the various factors that cause such differences, lithological changes can be considered as the most fundamental factor because the physical characteristics of a rock unit are closely related to its stiffness, which, in turn, determines the seismic wave velocities. Therefore, we set the boundaries of our local 1-D velocity model following the lithological changes along the depth profile using geological survey data Lee et al. (2015). However, if the seismic velocities of the two adjacent layers had no differences despite lithological variations between the layers, we combined them into a single layer in the final velocity model. Our local 1-D seismic velocity model is composed of two parts: a part shallower than 4.5 km, which is supported by both the geology obtained from the drilling cores and geophysical survey data, and a deep section below 4.5 km, which only contains seismological information. The shallow part is divided into six layers that are consistent with the lithological changes in the geological model by Lee et al. (2015). Two layers and a half space below the Moho, consisting of the deep part, were adopted from the Gyeongsang basin model by Kim et al. (2011). We built the final 1-D velocity model with seven layers above the Moho discontinuity and sub-Moho half-space by combining two adjacent layers with identical velocities into one layer. Details on the procedures for determining the discontinuities and velocities in the shallow part are described below. The depth required for the interface between the first and second layers, as well as their P-wave velocities, were adopted from the refraction survey that was performed in the vicinity of the EGS project site. The P-wave velocities for the first and second layers were 1.67 and 4.01 km/s, respectively. To determine the S-wave velocity of the first layer, the S-P times for the surface (MSS7) and borehole sensors (EXP1) at a depth of 150 m in the PX-2 well were measured for an event on February 6, 2016, at 15:01:34 UTC. We were unable to use the absolute arrival times measured by these sensors due to the asynchronization between the sensors. The S-wave velocity was estimated based on

the following equation:

$$d/V_S - d/V_P = t_{PS} \tag{A.1}$$

where d, V_P, V_S, and t_{PS} are the interstation distance, P- and S-wave velocities, and the S-P-time, respectively. For the given values, the S-wave velocity of the first layer was determined as 0.48 km/s using equation (S1). The S-wave velocity of the second layer was again adopted from the V_P/V_S ratio (1.81) determined by the Poisson's ratio (0.282) from mechanics experiments on the rock cores (Lee et al., 2019a). The P- and S-wave velocities of the third layer were determined using the arrival-time differences for the key event on August 13, 2017, at 21:42:37 UTC between the two end-members of the borehole seismometers in PX-2 at depths of 1.360 and 1.520 km, respectively (Fig. 4.2a). The P- and S-wave arrival time differences measured with the two borehole sensors were 0.031 and 0.052 s, respectively. We observed incidence angles of approximately 80° from the particle motions at the PX-2 borehole chains. Then, the P- and S-wave velocities for the third layer were determined as 5.08 and 3.03 km/s, respectively. As information on the velocities of the fourth and fifth layers were not available, the key event was again used to determine the velocities via a grid search, with an increment of 0.01 km/s between the range of velocities for the third and sixth layer, not allowing any low-velocity layers. Before the start of the procedure, the velocities of the first, second, third, and sixth layers were fixed by independent methods. The P-wave velocities of the fourth and fifth layers were estimated as 5.08 and 5.45 km/s, respectively, and the S-wave velocities were determined by adopting the V_P/V_S ratio from the well-logging data. The P- and S-wave velocities of the sixth layer were determined as 5.85 and 3.31 km/s, respectively, based on sonic log data from the PX-2 well (Fig. 4.2a). We set the top of the sixth layer as 3.400 km, which corresponds to the shallowest depth for the sonic log data. Determining the bottom depth for the sixth layer, which is the boundary between the shallow and deep parts, was demanding. The bottom depth of the sixth layer was set to 7.700 km, corresponding to the mean depth between the fifth and seventh layers.

A.2 Determination of the key event's absolute location

A.2.1 Orientation of the borehole geophones

Induced seismicity monitoring operations during the August 2017 stimulations at the Pohang EGS pilot project were performed using a linear vertical array of 160 m consisting of 17 three-component geophones (group interval of 10 m) deployed in the PX-2 well at a depth of 1,360 m (Fig. A.9). Determining the orientation of the horizontal components in the linear arrays of the geophones deployed in the borehole installations was a common challenge that affected the induced-seismicity-monitoring operations based on such network geometries. For this reason, finding the correct orientations of the three component seismic sensors deployed in the borehole installations was the first step in the processing of these data types. In this study, we summarized the orientation results of the borehole sensor array deployed at the Pohang EGS site using the method proposed by Grigoli et al. (2012); Krieger and Grigoli (2015). This method relies on the hypothesis that, for two aligned seismic sensors, the misfit between the respective waveforms is minimum (i.e., when the inter-station distance is much smaller than the station–source distance) while the misfit increases if the sensors are not aligned. In this approach, the relative orientation angles were retrieved by minimizing, in a least-squares sense, the l2-norm between the complex traces (hodograms) of adjacent sensor pairs. Thus, we can find the alignment angle between a pair of sensors by solving a linear inverse problem in the complex domain. Once all sensors of an array are aligned, the absolute orientation can be found using teleseismic events with known locations. In the first step, the aligned horizontal seismic traces were stacked to improve the signal-to-noise (SNR) ratio. Then, polarization analysis techniques were used for the stacked trace to obtain a more robust azimuth estimation of the teleseismic event. As the location of the teleseismic events is known by comparing its azimuth with the azimuth obtained from the array sensors, we can retrieve the absolute orientation of the array. To find the relative orientation of each adjacent sensor pair in the array, we used the key event. Figure A.10 shows the hodogram of a pair of sensors, PX01-PX02, before

and after the alignment process. All waveforms were bandpass-filtered between 1 and 50 Hz, with a second-order Butterworth filter. In the second step, we obtained an independent estimate of the absolute orientations of the array by estimating the azimuth of the following regional earthquake in the northwest region of the Ryukyu islands (August 16, 2017, 12:51:25 UTC; M_{W} 5.7; lat. 28.6737°; lon. 127.9007°; depth 198 km) and compared the results with the "true" azimuth (which, in this case, is approximately 189°). To estimate the azimuth form of the recorded waveforms, we used a polarization analysis technique based on the multi-window PCA (Noda et al., 2012; Eisermann et al., 2015) that we applied to all 17 geophones that formed the array. Figure A.11 shows the polarization analysis results for the GFZ04 sensor using a time window of 2 s, which contains the first P-wave arrival. The azimuth estimations can be improved by aligning the horizontal components of each sensor in the array and stacking their waveforms. This process allowed us to increase the linearity of the signal, providing a more robust azimuth estimation (estimated azimuth = 191°, "true" azimuth approximately 189°), as shown in Fig. A.12.

A.2.2 Location of the key event on 13 August 2017

As previously mentioned, estimating the azimuth and incidence angles for an event can be further improved by applying PCA on the stacked waveforms. Figure A.13 shows the hodogram and estimated azimuth distribution for the stacked waveforms of the key event. Before stacking, all waveforms were filtered in the frequency range of 1–100 Hz. We note that the use of stacked waveforms strongly increased the rectilinearity of the signal within the first P-wave arrival window, providing more robust results. The incidence angle and azimuth of the event were determined as 322 ± 6° and 11 ± 3°, respectively. Finally, we used the PS time to obtain an estimation of the source–receiver distance to determine the absolute location of the seismic event from the estimated azimuth and incidence angles. To calculate the source–receiver distance, we used a P-wave velocity range between 5.4 and 5.8 km/s and a V_P/V_S ratio of 1.77.

Table S3 summarizes the location results based on the measured PS-time, azimuth, and incidence angle.

A.2.3 Key event focal depth validation using PS times from wellbore sensors and tube waves

We used the source–receiver distances (R1 and R2) estimated at the shallowest and deepest geophones of the array, respectively, to obtain an independent estimation of the depth of the key event as proposed in Grigoli et al. (2018). Figure A.14 shows a simple geometrical approach that allowed us to calculate the depth by solving a circle intersection problem. The source–receiver distance at the shallowest and deepest sensors of the array was calculated using the PS times for a range of seismic velocities. The range of P-wave velocities was 5.4–5.8 km/s while the range of S-wave velocities was calculated using a V_P/V_S velocity ratio of 1.77. Based on this, we were able to calculate the minimum and maximum source–receiver distances (r, R with r < R) for each event. The measured PS times for the shallowest and deepest sensors were 0.403 ± 0.007 and 0.381 ± 0.007 s, respectively, which yielded a depth range of 3.80–4.37 km (Fig. A.14).

Tube waves are interfacial waves that occur in encased wellbores when seismic waves impinge on the casing of the well and perturb the fluid in the wellbore. Tube waves travel in the wellbore along the fluid–wall interface of the wellbore at the same speed as the borehole fluid. In this application, we assumed that the direct P and S phases were converted into tube waves at the end of the encased well, such that during propagation as tube waves, there was no change in the initial PS time at the time of the conversion. The tube waves allowed us to measure the PS time at the end of the encased well (i.e., similar to measuring the PS time at a station located at the end of the encased well), which increased the depth resolution estimation. Figure A.15 illustrates the tube waveforms of the key event recorded by the PX07 sensor. To determine the depth ranges for both events, we used a previously described approach. We used the PS

time measured by the PX01 sensor and PS time extracted from the tube waves, which we considered to have originated from the end of the encased well. The intersection of circles (obtained using the same velocity range as before) provided a range of suitable depths for these events. In this case, the event range was smaller, such that there was a reduction in the related uncertainty. Figure A.16 illustrates that we determined a focal depth range of the key event at between 3.98 and 4.37 km.

A.3 Station corrections for accurate M_{L} measurements

Station corrections were estimated with 194 aftershocks that occurred from November 16, 2017, to December 31, 2017. We only used aftershocks that had more than or equal to five observations at permanent stations. After a careful visual inspection, we measured the zero-to-peak amplitudes from the synthesized Wood–Anderson displacements of the vertical component. Individual station magnitudes of the permanent stations were averaged to yield the initial event magnitude. The differences between the initial event magnitude and each station magnitude were averaged for individual permanent and temporary stations, which corresponded to the station correction, ranging from –0.657 to 0.768. We assumed that the large negative and positive values were due to de-amplification of the borehole instrument and amplification of soil, respectively. We also note that the station corrections of the broadband borehole instrument at YOCB and YODB reported in Sheen et al. (2018) were 0.050 and –0.134, whereas those from this study were 0.018 and –0.195, respectively, which are similar to each other. Several temporary stations were only operated during the stimulation period. Corrections for these stations were made based on the records of 17 events that occurred during the stimulation period, ranging from –0.424 to 1.177.

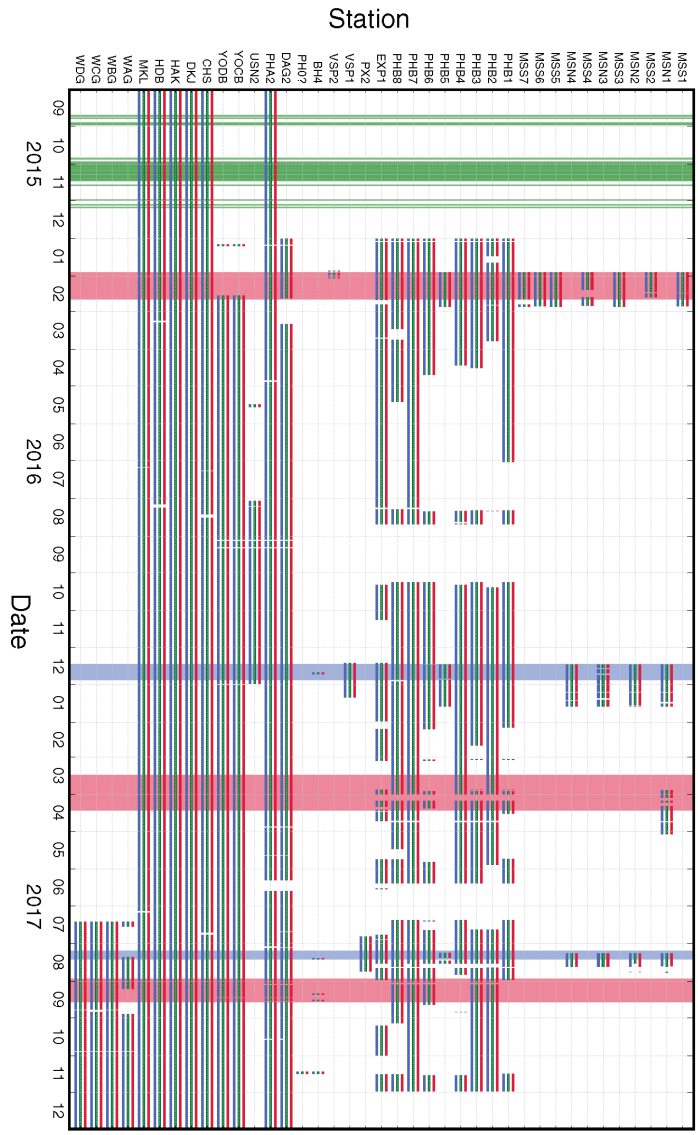

Figure A.1: The period of operation for the seismic stations used in this study. The period of drilling mud loss at PX-2 is shaded in green. The periods of hydraulic stimulations at PX-1 and PX-2 are shaded in blue and red, respectively. The red, green, and blue lines indicate the operation of the E-, N-, and Z- components at each seismic station.

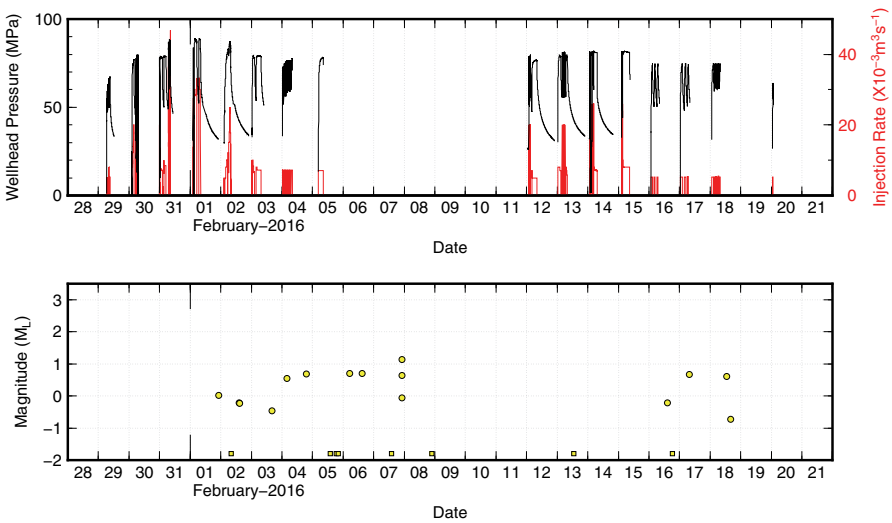

Figure A.2: History of the injection rate, wellhead pressure, and seismicity of the first stimulation at PX-2. The earthquakes for which the local magnitudes were not determined are denoted by square symbols.

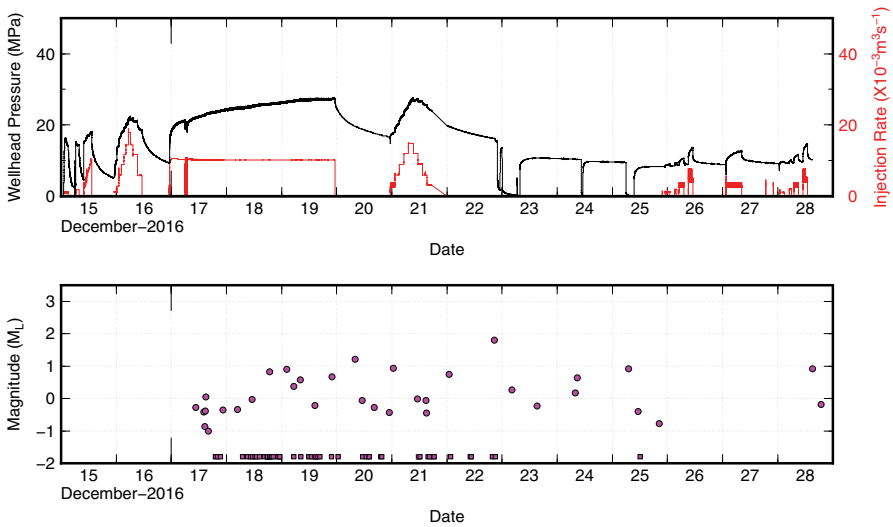

Figure A.3: History of the injection rate, wellhead pressure, and seismicity of the second stimulation at PX-1. The earthquakes for which the local magnitudes were not determined are denoted by square symbols.

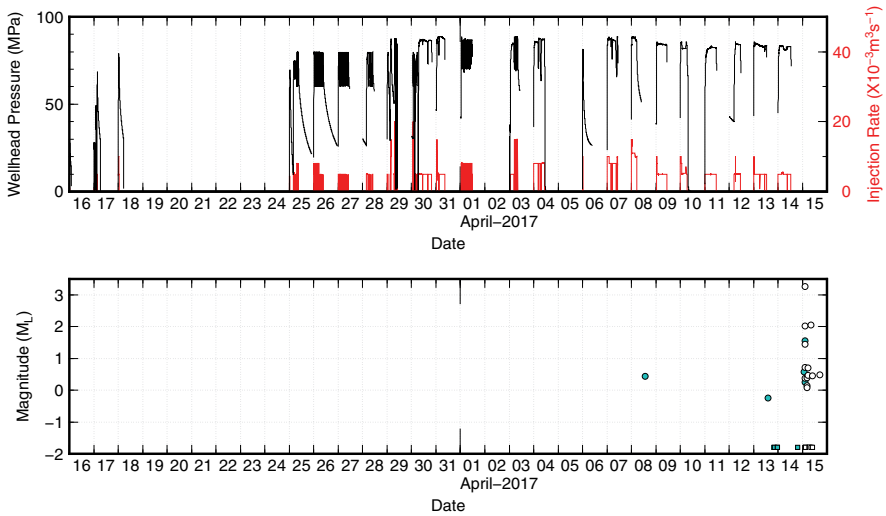

Figure A.4: History of the injection rate, wellhead pressure, and seismicity of the third stimulation at PX-2. The earthquakes for which the local magnitudes were not determined are denoted by square symbols. The M_{W} 3.2 earthquake and its aftershocks are shown in white.

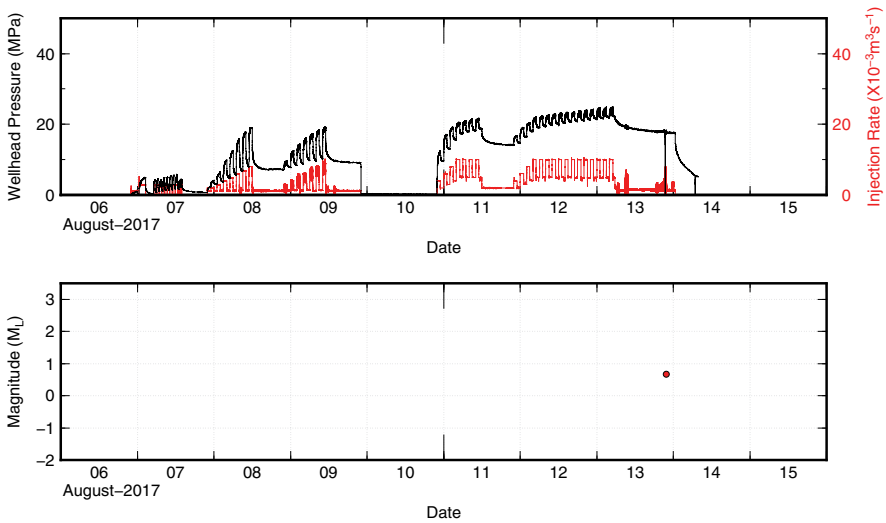

Figure A.5: History of the injection rate, wellhead pressure, and seismicity of the fourth stimulation at PX-1. Note that only one earthquake was observed during this period.

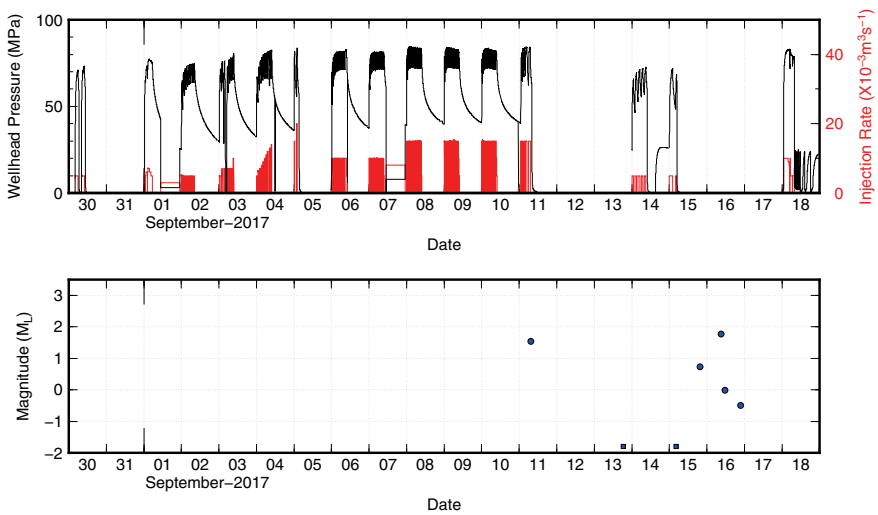

Figure A.6: History of the injection rate, wellhead pressure, and seismicity of the fifth stimulation at PX-2. The earthquakes for which the local magnitudes were not determined are denoted by square symbols.

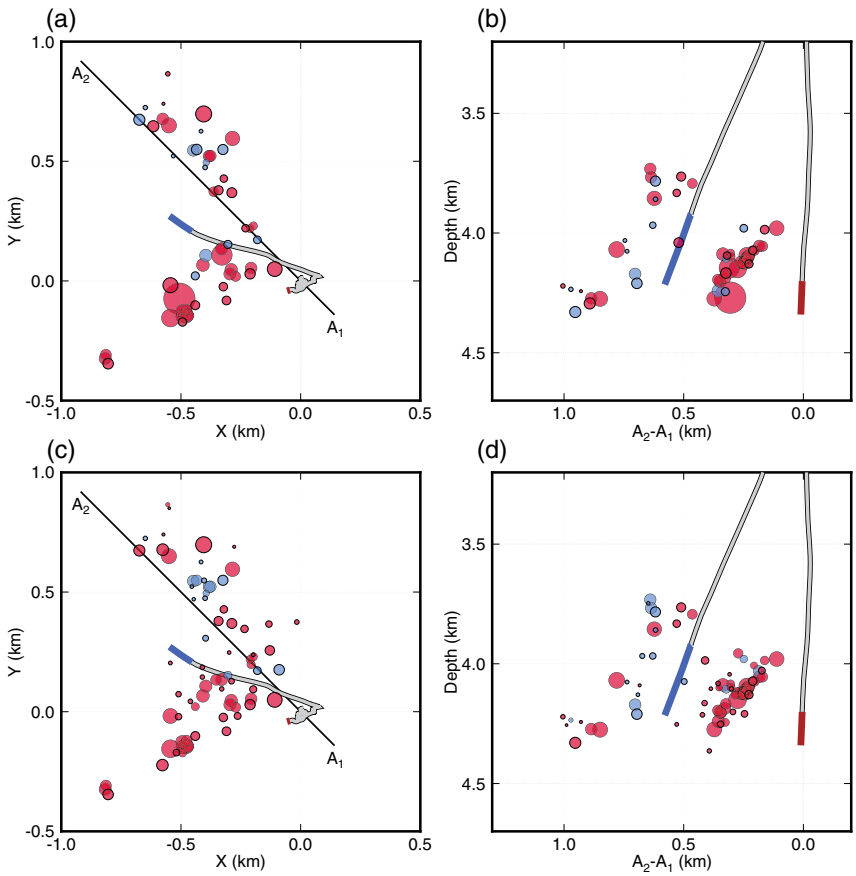

Figure A.7: Epicenter distribution of clusters classified by (a) Kagan angles among focal mechanisms and (c) the waveform similarity based on cross-correlation and their cross-sectional views along A1 and A2 (i.e., (b) and (d), respectively). The colored symbols correspond to the symbols shown in 4.7: red for the A and CW-1 groups and blue for the B to E and CW-2 groups.

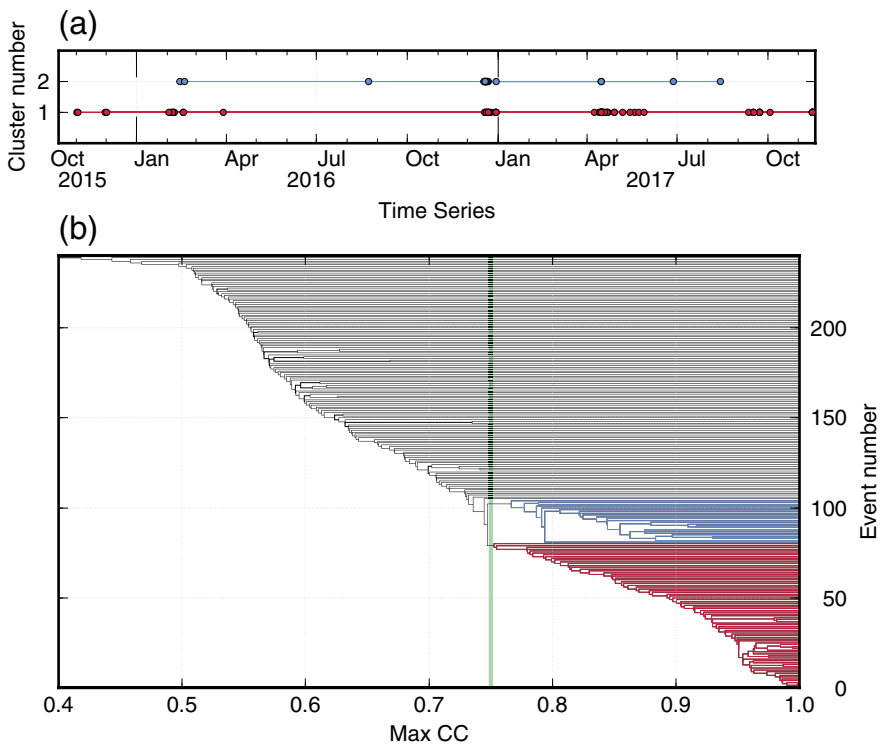

Figure A.8: Results of the hierarchical clustering analysis for waveform similarity. Two groups (CW-1 and CW-2) with a threshold of 0.75 were identified from the 240 events with a clear phase identification at PHA2. (a) Time history of earthquakes in each group and (b) dendrogram for the hierarchical clustering analysis.

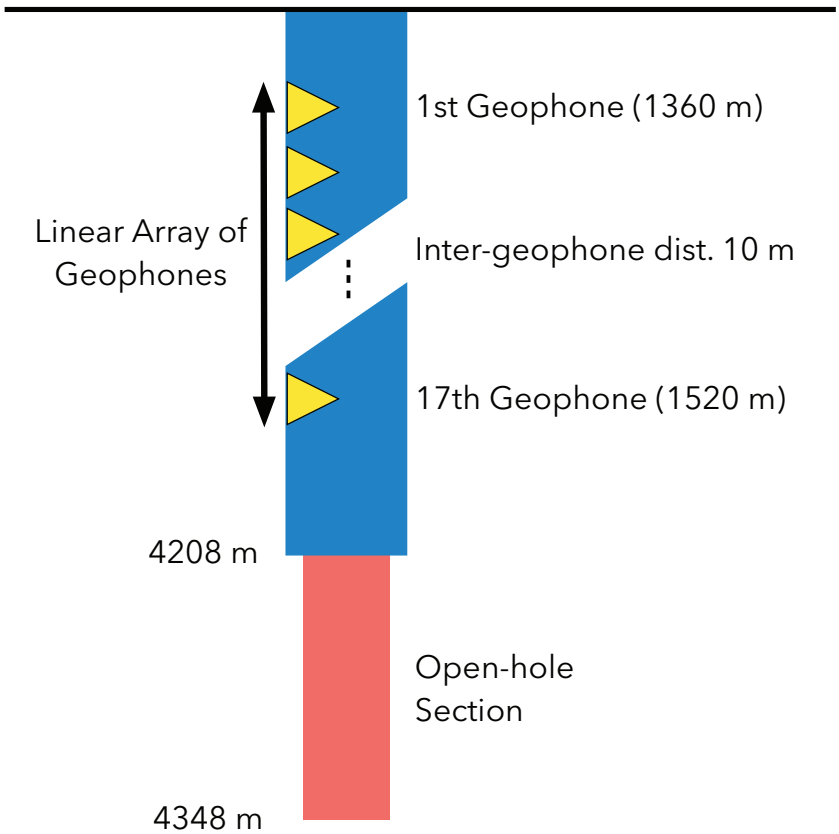

Figure A.9: A sketch of the PX-2 well. Blue and red sections represent, respectively, the cased and open-hole part of the well.

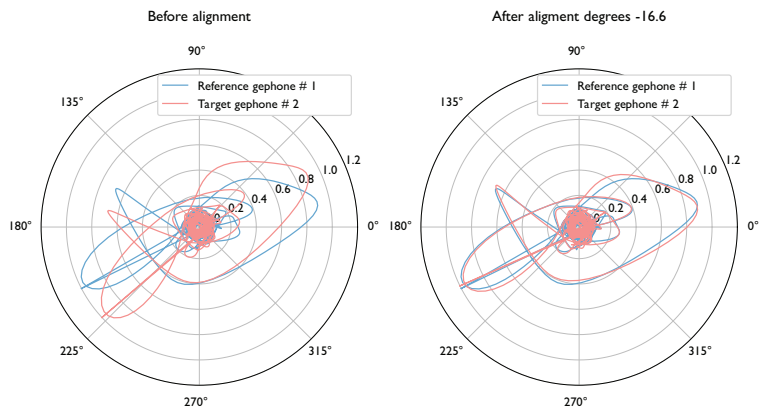

Figure A.10: Hodograms of the horizontal component waveforms recorded by the geophones at PX01, which were taken as the reference (blue line), and PX02 (red line). (Left panel) Before and (right panel) after the alignment process.

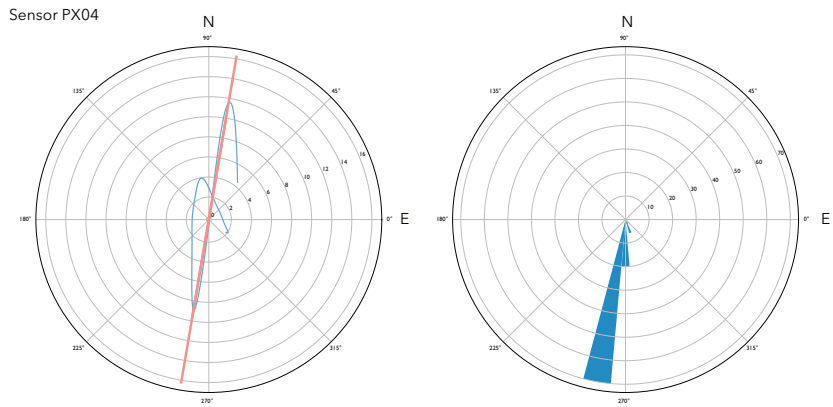

Figure A.11: (left panel) Hodogram of the horizontal component waveforms recorded by the geophone at PX04 (blue line) and the direction of maximum polarization (red line). (right panel) The distribution of the azimuths computed using a multi-window PCA.

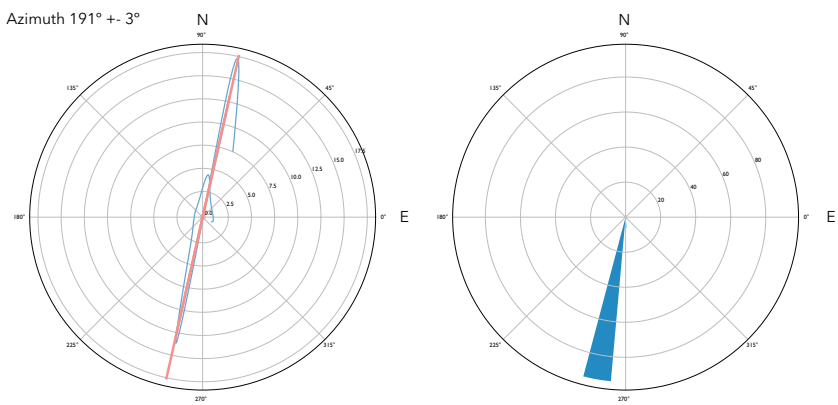

Figure A.12: (left panel) Hodogram obtained by stacking the aligned horizontal component waveforms of each sensor in the array and direction of maximum polarization (red line). (right panel) The distribution of the azimuths computed using a multi-window PCA.

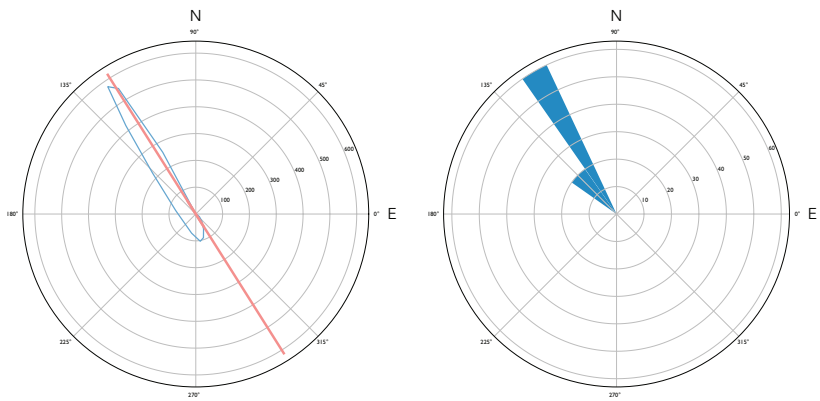

Figure A.13: (left panel) Hodogram of the stacked waveforms for the key event (blue line) and the direction of maximum polarization (red line). (right panel) The distribution of the azimuths computed using a multi-window PCA. Note that the angles are not converted to azimuth with respect to the North but taken anticlockwise from the East.

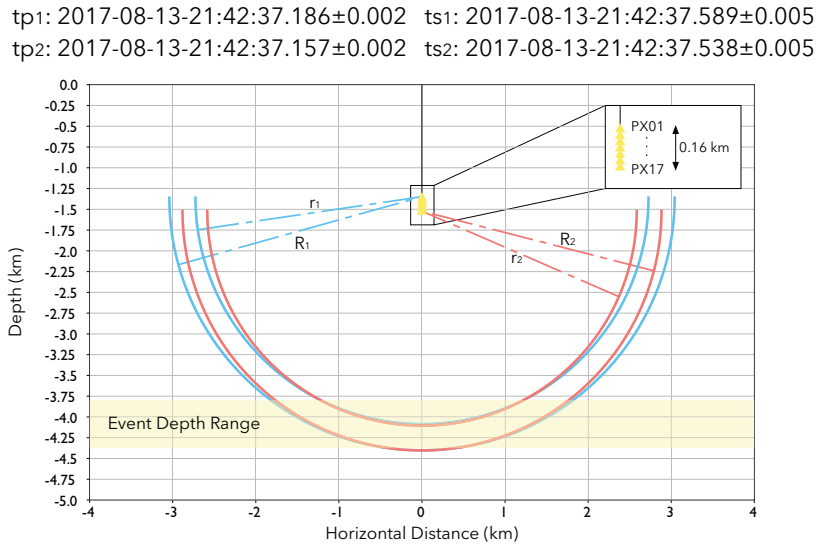

Figure A.14: Illustration of the depth event range obtained for the key event. The minimum and maximum source–receiver distances are denoted by ri and Ri, respectively. The indices 1 and 2 refer to the PX01 and PX17 sensors, respectively, while the yellow area denotes the potential depth range of the event.

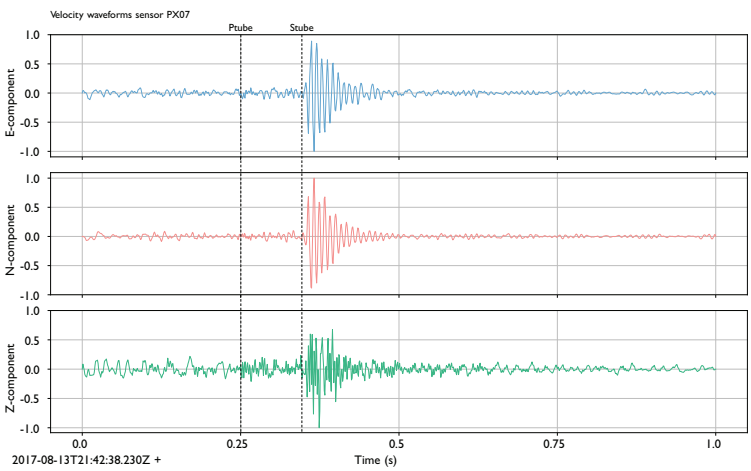

Figure A.15: Tube waveforms (normalized) recorded by the PX07 sensor. Ptube and Stube are the P and S waves converted into tube waves at the end of the encased well.

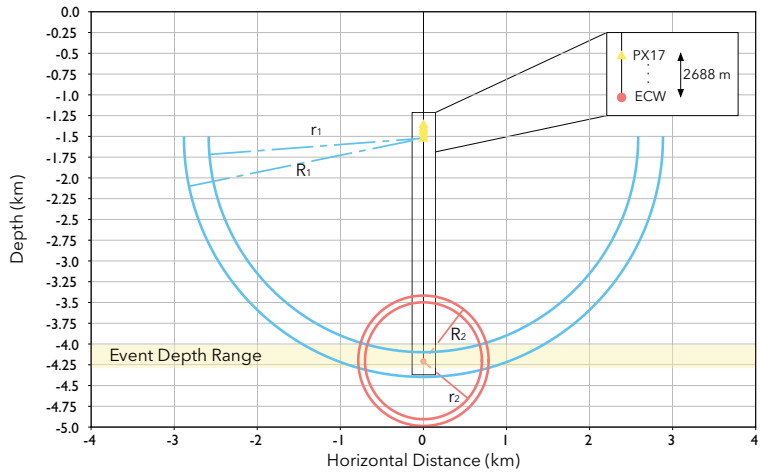

Figure A.16: Illustration of the depth event range obtained for the key event. The minimum and maximum source–receiver distances are denoted by ri and Ri, respectively. The indices 1 and 2 refer to the PX17 sensor and end of the encased well, respectively, while the yellow area denotes the potential depth range of the event.

Table A.1: Detailed information for the seismic stations mainly used in this study.

Network	Station	Latitude (°)	Longitude (°)	Elevation (m)	ETC
EG	MSS1	36.1182	129.3792	–9	Surface seismometers from KIGAM
	MSN1	36.1182	129.3792	–9	
	MSS2	36.1107	129.4272	–4	
	MSN2	36.0913	129.4156	14	
	MSS3	36.0973	129.4277	–12	
	MSN3	36.0649	129.3966	31	
	MSS4	36.0593	129.3671	14	
	MSN4	36.0645	129.3500	44	
	MSS5	36.0886	129.3510	–14	
	MSS6	36.1162	129.3152	3	
	MSS7	36.1059	129.3784	4	
	PHB1	36.1463	129.3923	–148	Borehole seismometers from KIGAM
	PHB2	36.1140	129.4219	–114	
	PHB3	36.0973	129.4278	–134	
	PHB4	36.0867	129.3970	–145	
	PHB5	36.0535	129.3610	–144	
	PHB6	36.0886	129.3510	–108	
	PHB7	36.1162	129.3152	–114	
	PHB8	36.1271	129.3611	–145	
	EXP1	36.1059	129.3784	–150	
PX	PX01-PX17	36.1068	129.3782	from –1,350 to –1,520	Borehole seismometers from KIGAM

VSP	V135, V155	36.1068	129.3782	–1,350, –1,550	Borehole seismometers from KIGAM
	V136, V137, V138	36.1068	129.3782	–1,360, –1,370, –1,380	
ETH	BH4, POH01	36.1068	129.3782	0, –2,300	Surface and borehole seismometers from KIGAM
PH	PH01	36.1075	129.3520	25	Temporary seismic stations from K.-H. Kim
	PH03	36.1142	129.3770	22	
	PH04	36.1013	129.3789	54	
	PH05	36.0969	129.3462	14	
	PH06	36.1115	129.3856	34	
	PH07	36.1083	129.3644	7	
	PH08	36.1209	129.3661	10	
	PH09	36.1186	129.3514	12	
KS	DAG2	35.7685	128.8970	294	Permanent KMA seismic network
	PHA2	36.1930	129.3708	73	
	USN2	35.7024	129.1232	250	
	YOCB	35.9771	128.9511	143	
	YODB	36.5333	129.4095	92	
KG	CHS	36.1811	129.0881	240	KIGAM permanent seismic network
	DKJ	35.9468	129.1089	173	
	HAK	35.9296	129.5004	16	
	HDB	35.7337	129.3991	146	
	MKL	35.7322	129.2420	187	

KN	WAG	35.7070	129.4706	N/A	KHNP permanent seismic network
	WBG	35.6749	129.4051	N/A	
	WCG	35.8498	129.2375	N/A	
	WDG	35.8834	129.4020	N/A	

Table A.2: Detailed information for the seismic stations mainly used in this study.

Origin time (yyyy/mm/dd HH:MM:SS.SS)	Latitude (°)	Longitude (°)	Depth (km)	Magnitude
2015/11/30 03:52:20.72	36.104	129.358	4.3	0.80
2016/02/06 05:11:31.42	36.104	129.354	4.8	0.70
2016/02/07 22:04:12.61	36.103	129.354	4.8	1.14
2016/02/07 22:04:15.78	36.102	129.356	4.5	0.64
2016/02/17 07:43:44.36	36.102	129.356	4.8	0.67
2016/03/12 07:25:47.11	36.105	129.358	4.9	0.76
2016/03/31 03:58:14.00	36.110	129.360	4.3	1.18
2016/12/17 22:28:23.82	36.108	129.353	3.2	–0.36
2016/12/18 18:43:44.71	36.107	129.355	4.0	0.82
2016/12/19 05:18:48.97	36.108	129.359	4.8	0.37
2016/12/19 22:02:34.66	36.105	129.356	5.0	0.67
2016/12/20 07:56:08.37	36.106	129.355	4.4	1.21
2016/12/22 20:31:33.00	36.120	129.310	4.3	1.80
2016/12/25 06:59:50.33	36.106	129.356	4.4	0.92
2016/12/28 15:12:14.79	36.106	129.353	3.9	0.91
2016/12/29 12:32:25.80	36.107	129.355	4.0	2.15
2017/04/15 02:31:07.59	36.104	129.358	4.9	1.55
2017/04/15 02:31:13.35	36.102	129.356	4.5	3.27
2017/04/15 08:16:47.38	36.103	129.354	4.8	2.06
2017/04/15 09:47:59.98	36.101	129.360	4.8	0.45
2017/04/15 17:02:30.49	36.101	129.357	4.8	0.48
2017/04/16 01:44:47.16	36.099	129.350	3.6	0.97
2017/04/16 01:50:18.13	36.097	129.353	3.0	0.74
2017/04/20 13:01:36.61	36.099	129.350	4.0	0.67

2017/04/20 22:14:20.84	36.102	129.357	4.8	0.66
2017/04/21 18:51:04.45	36.100	129.357	4.8	0.45
2017/04/21 23:58:10.66	36.102	129.356	4.9	0.96
2017/05/18 19:04:32.94	36.101	129.355	4.9	0.89
2017/08/13 21:42:37.24	36.107	129.355	4.4	0.67
2017/09/11 07:19:24.73	36.107	129.358	4.4	1.54
2017/09/15 19:33:49.91	36.102	129.358	4.8	0.73
2017/09/16 08:55:56.12	36.103	129.355	4.8	1.78
2017/09/22 14:27:21.40	36.103	129.360	5.3	1.17
2017/09/26 20:46:43.59	36.105	129.358	4.9	0.15
2017/11/14 19:55:15.35	36.101	129.355	4.8	1.60
2017/11/14 20:04:17.36	36.101	129.355	4.8	1.70
2017/11/14 20:59:38.01	36.099	129.355	3.8	1.25
2017/11/15 05:22:32.56	36.101	129.354	4.8	2.12
2017/11/15 05:22:43.89	36.101	129.357	4.9	2.86

Table A.3: Location information for the key event.

	Parameters of the key event
P-wave arrival time at PX01	2017-08-13 21:42:37.186 ± 0.002
S-wave arrival time at PX01	2017-08-13 21:42:37.589 ± 0.005
R (min–max)	2,727–3,041 m
Easting (m) for UTM wgs 84 zone 52N	533,603 ± 69
Northing (m) for UTM wgs 84 zone 52N	3,996,409 ± 66
Depth (km)	4.21 ± 0.10
Latitude (°)	36.1117
Longitude (°)	129.3734

B Supporting Information for Aftershock sequences and statistics of the 2017 M_W 5.5 Pohang earthquake, South Korea: fault heterogeneity and possible post-seismic relaxation

Table B.1 describes the detailed parameters used in FAST earthquake detection (Yoon et al., 2015; Bergen and Beroza, 2018)

Table B.1: Input parameters for the FAST algorithm (Yoon et al., 2015; Bergen and Beroza, 2018; Rong et al., 2018) to detect earthquakes with waveform similarity.

Fingerprint Extraction parameter	Value
Time-series window length of generated spectrogram	6.0 s
Time-series window lag of generated spectrogram	0.1 s
Spectral image window length	64
Spectral image window lag	10
Fingerprint sparsity	400
Final spectral image width	32
Number of hash functions per hash table	4
Number of hash tables	100
Number of votes	2
Near-repeat exclusion parameters	5
Event-pair extraction, pruning, and network detection parameters	**Value**
Time gap along diagonal	3 s
Time gap adjacent diagonal	3 s
Adjacent diagonal merge iteration	2
Number of votes	10
Minimum fingerprint pairs	3
Maximum bounding-box width	5 s
Minimum number of stations for detection	1
Arrival time constraint: maximum time gap	5

초 록

판 내부지진 (Intraplate earthquakes, IEs)은 판 경계로부터 전달된 응력이 판 내부에 존재하는 단층 구조에 작용하는 과정에서 발생한다. 판 경계에 비해서 판 내부 지역은 시간당 응력 변화량이 매우 적고 발생되는 지진의 크기 및 개수가 작은 편으로 중 규모 이상 (규모 4 이상)의 지진 관측이 쉽지 않다. 또한 지표면 하부에 존재하는 단층 구조를 확인하는 것은 어려우며, 수백 킬로미터 이상의 먼 지역으로 전달된 응력과 판 내부의 단층 구조가 어떤 식으로 상호작용하는지를 확인하는 것은 더욱 어렵다. 한반도는 류큐 및 난카이 해구로부터 800km 떨어진 판 내부에 위치하며 중규모의 지진 관측이 매우 적은 지역에 해당한다. 실제 한반도에서 계기 지진의 관측이 시작된 1978년 이후 한반도 및 한반도 근처 해역상에서 기상청에 의해 발표된 지역 규모 (M_{L}) 5 이상의 지진은 총 10개뿐이다. 이 지진들 중 2016년과 2017년에 경주와 포항에서 각각 발생한 지역 규모 5.8과 5.4의 지진은 가장 큰 규모에 해당하는 두 지진일 뿐만 아니라 비교적 최근에 발생하여 지진학적 관측이 잘 이루어졌기 때문에 이 지진들을 연구하는 것은 한반도 내에 발생하는 중규모 지진의 특성을 연구하는 데에 도움이 될 수 있다. 본 연구의 목적은 한반도에서 발생된 중 규모 지진의 다양한 지진원적 특성을 밝히고 판내부에서 발생하는 지진이 어떤 지질학적 구조에서 발생할 수 있는 지에 대한 사례 연구를 제공함에 있다.

2016년 M_{L} 5.8 경주 지진 및 여진에 대한 지진원 분석 결과, 본진은 양산 단층의 하부에서 발생했으나, 관측된 지표 변위가 없음과 여진 분포를 통해서 확인된 단층면이 양산단층과 다른 주향을 가지고 있음을 고려할 때, 양산 단층 하부에 발달된 부수적인 단층면이 현재 응력 방향과 맞게 재활성화된 것으로 판단된다. 여진에 대

한 단층면 역산 결과 확인된 역단층 및 주향이동 단층은 현재 한반도에 작용하는 주응력이 동서 방향인 것과 대응된다. 발견된 여진의 분포는 경주 지진이 하나의 단일 지진면에서 발생한 것이 아니라 적어도 3개 이상의 분절된 단층대에서 복합적으로 발생했음을 확인하였다. 특히 본진 보다 50분 이전에 발생한 M_L 5.1 지진에 의해서 발생된 정적 응력 계산 결과는 본진의 위치의 쿨롱 응력을 증가시켜 지진의 촉발 시켰을 가능성이 있음을 보여준다.

여진 분포에 따른 응력장의 변화는 경주 지진이 발생한 공간상의 응력장에 지역적 이질성이 있음을 시사한다. 특히 15km 보다 깊은 지역에서 주향이동 단층이 우세하게 보이는 현상은 이 깊이에서 발견된 시공간 상으로 이동하는 밀집된 지진군과 관련이 있을 것으로 해석된다.

2017년 M_L 5.4 포항 지진은 인근 지열 발전소 부근에서 발생하여, 지열 발전소에서 실시한 수리 자극 실험이 지진의 발생에 영향을 주었을 것이라는 의혹이 제기되었다. 이들 사이의 인과 관계를 상세하게 검증하기 위해 해당 지열 발전소에서 실시한 다섯 차례에 걸친 수리 자극 실험 기간 및 시추공에서 이수가 누출된 기간 동안 발생한 지진과 포항 본진 및 전진의 시공간적 분포를 지열정에 유체를 주입한 시기와 비교하였다. 그 결과 포항지진과 이 지진의 전진들은 하나의 지열정에 대해 실시한 수리자극 실험 기간 동안 발생한 지진 분포와 같은 면 상에서 분포하였으며, 시간적으로 이주하는 양상도 확인하였다. 진원 분포가 가지는 평면은 본진 이후 발생한 여진의 분포로부터 확인된 단층면과도 잘 대응되며, 영상 검출 장비를 통해서 확인된 지열정의 파쇄 구간과도 일치하였다.

포항 지진의 여진의 위치 분석 결과, 경주 지진의 여진 분포와 마찬가지로 단일 단층면이 아닌 적어도 4개 이상의 단층 구조가 포항 지진으로 인해 재활성된 것으로 판단된다. 특히 3달 경과 후 발생한 M_L 4.6 여진은 본진에 해당하는 단층면의 공액 단층면 상에서 발생한 것으로 추정된다. 포항 본진에 관여한 단층면은 크게 3개의 분절로 나뉘며, 이 중 2개의 분절의 교차점에서 본진이 발생한 것으로 추정된다. 본진의 슬립 분포를 유한 단층 역산법을 통해 확인한 결과, 약 4초 가량의 시간 동안 크게 단층대 중 슬립이 시간 순서 상으로 각각 남서쪽과 북동쪽에서 2초의 시간간격을 두고 발생한 것으로 확인이 되며, 이 시간 차이는 북동쪽에 위치한 단층대가 본진이

위치한 곳의 단층대와 공간적으로 분절되어 있음에 기인할 것으로 추정된다.

두 지진의 사례 연구를 통해 확인된 경상 분지 내에서 발생한 중규모 지진의 공통적 특성으로는 (1) 단일 단층의 활성이 아닌 단층 파쇄대를 통한 단층의 움직임, (2) 한반도에 대해서 공통적으로 작용하고 있는 동서 방향의 주응력에 대응하는 주향이동단층 및 역단층의 발견 (3) 과거 신생대에 분지 구조를 형성할 당시에 생긴 것으로 추정된 표면 단층선과 현재 응력 방향에 대해서 재활성된 단층과의 관계, (4) 여진 발생 시 수 일의 시간 동안 증가하는 ***b***-value, (5) 단층의 분절대 또는 단층면의 가장자리에서 규모 4 이상의 중규모 지진들이 발생한다는 점이 있다. 이 특성들은 고대 문헌 상으로 한반도에서 발생한 것으로 추정되는 지진들과 미래에 발생할 수 있는 지진들의 특성을 조사하기 위해 활용될 가치가 있으며, 전지구적으로 발생되는 판 내부 지진들의 일반적인 특성을 규명하는 데에 도움을 줄 것으로 기대된다.

주요어: 지진 위치 결정, 단층면 해 분석, 유한 단층 역산, 유발 지진과 촉발 지진, 여진 모니터링 시스템

학번: 2015-20467